12-9-2016

Synthesis and Characterization of Transition Metal Oxide Catalysts for Environmental and Energy Storage Applications

Wenqiao Song
University of Connecticut - Storrs, wenqiao.song@gmail.com

Synthesis and Characterization of Transition Metal Oxide Catalysts for Environmental and Energy Storage Applications

Wenqiao Song, PhD

University of Connecticut, 2016

Nowadays, environmental concerns and the global energy crisis have become two of our greatest challenges. The main purpose of this dissertation research is to design highly active mesoporous materials that can efficiently catalyze environmental and energy related reactions. Surface properties can be easily tuned by thermal treatment and cation doping, resulting in improved catalytic activities. Synthesis and characterization of the materials, catalytic activities for carbon monoxide oxidation, oxygen reduction and oxygen evolution reactions, and mechanistic studies are covered in this thesis.

The first part describes the synthesis of mesoporous cobalt oxides through an inverse micelle route for low temperature carbon monoxide oxidation applications. The prepared material showed much better activity and stability compared with commercial cobalt oxide due to its nanoparticle nature and porous structure. The catalytic performance under both dry and moisture rich conditions were tested. Detailed characterization of the materials suggested that high surface areas and the presence of surface oxygen vacancies were critical for enhanced activities.

In real systems, structured catalysts such as monolithic substrates coated with a layer of active material are used instead of powder form catalysts. To evaluate the potential of our catalysts to be used in practical catalytic devices, mesoporous metal oxides (MnO_x, Co_3O_4, CeO_2) were coated on cordierite substrate by dip coating and in-situ growth and were used as low temperature diesel oxidation catalysts. The resulting materials showed promising catalytic performance. The

effect of particle size, loading amount and Cu doping on the catalytic performance are discussed in detail.

In the last part, mesoporous cobalt oxides were used as bifunctional catalysts for oxygen reduction and oxygen evolution reactions. If a catalyst can catalyze both reactions, it will have great potential in the application of rechargeable metal air batteries. Ni and Mn doping were introduced into the cobalt oxide material to increase the conductivity and active site population. The Ni incorporated cobalt oxide exhibited the best activity, which can be considered as a potential substituent for precious metal catalysts (Pt, Ir, Ru). Furthermore, the intrinsic structure-property relationships of the materials were established.

Synthesis and Characterization of Transition Metal Oxide Catalysts for Environmental and Energy Storage Applications

Wenqiao Song

B.S., Dalian University of Technology, 2010

A Dissertation

Submitted in Partial Fulfillment of the

Requirements for the Degree of

Doctor of Philosophy

at the

University of Connecticut

2016

APPROVAL PAGE

Doctor of Philosophy Dissertation

Synthesis and Characterization of Transition Metal Oxide Catalysts for Environmental and Energy Storage Applications

Presented by

Wenqiao Song, B.S.

Major Advisor_____

Steven L. Suib

Associate Advisor_____

Alfredo Angeles-Boza

Associate Advisor_____

Jie He

Associate Advisor_____

Pu-Xian Gao

Associate Advisor_____

Fatma Selampinar

University of Connecticut

2016

Dedicated to My Family

ACKNOWLEDGEMENTS

First, I would like to acknowledge my major advisor Dr. Steven L. Suib for his generous support, encouragement and guidance throughout my graduate studies. His enthusiastic, energetic and positive attitude towards research and teaching have greatly inspired me and will have deep impact on my future career. I am also sincerely grateful to Dr. Francis S. Galasso for his kindness, patience and all his help on my research and life. Many thanks to my associate advisors as well: Drs. Alfredo Angeles-Boza, Jie He, Pu-Xian Gao, and Fatma Selampinar for their suggestions and help in completing this dissertation.

I also express my gratitude to my colleagues for their training, contributions, suggestions and discussion on my research and their friendships. Working and living in the Suib group have been a memorable experience in my life. Special thanks to Dr. Altug Poyraz, Dr. Yongtao Meng, Dr. Chung-Hao Kuo, Sheng-Yu Chen, Yang Wu, Dr. Sourav Biswas, Ting Jiang, Wei Zhong, Dr. Zhu Luo, Ran Miao, Jing Jin, Dr. Yashan Zhang, Dr. Boxun Hu, Dr. Lakshitha Pahalagedara, Saiful Islam, Junkai He, Tahereh Jafari, and everyone in Suib's group.

Lastly, my deepest gratitude goes to my Dad and Mom, my husband and my family. Their eternal love and support means more to me than they will ever know. Thanks for always being there for me. I could not have done it without them. I love them so much.

TABLE OF CONTENTS

LIST OF FIGURES

LIST OF TABLES

CHAPTER 1. INTRODUCTION

1.1 Overview

In the past few decades, designing efficient catalyst systems which can solve environmental pollution and energy shortage problems has attracted a great deal of attention. Catalysts can be classified into two groups: homogeneous and heterogeneous catalysts. Compared with homogeneous catalysts, heterogeneous catalysts are more stable and degrade slower, and can be readily separated from reaction mixtures. However, the state of the art heterogeneous catalysts are still based on precious metals, thus placing a high demand for cost efficient noble metal free catalysts which can exhibit comparable catalytic performance. The aim of this dissertation is to develop high performance catalysts using cheap, abundant materials and can be prepared by simple synthesis steps.

In heterogeneous catalysis, reactions occur through a series of steps including adsorption, reaction and desorption. All those steps take place on the interfacial surface of the materials, which makes surface area a critical parameter in determining the catalytic activities. Mesoporous catalysts possess high surface areas and large pore volumes. As a result of these merits, this type of material can provide more accessible active sites, facilitate diffusion of reactants and products, and finally enhance the catalytic performance.[1, 2] Two general methodologies were used in the synthesis of mesoporous materials: soft-template and hard-template methods. In the hard-template approach, an ordered mesoporous material, usually mesoporous carbon or silica, was used as the template. After impregnation of inorganic precursors into the pores of the template, the sample was calcined to form the desired crystal phase. Finally, the template was removed by chemical etching or calcination, and the formed product is the negative replica of the template. This

approach was widely applied to synthesize different types of crystalline mesoporous materials. The pore size, wall thickness and surface area of the materials completely depend on the structure of the template. So tuning the surface structures and optimizing the catalytic properties are not easy to achieve using this method.

On the other hand, mesoporous materials can also be obtained by direct synthesis based on surfactant inorganic precursor self-assembly, which is called the soft template method. This synthetic protocol allowed us to prepare mesoporous catalysts with tunable morphology, pore size, surface area and pore volume, resulting in improved activities. Furthermore, this makes structure-property relationship investigations possible. Among all the mesoporous materials, mesoporous transition metal oxides have been studied most intensively due to their excellent catalytic properties. Especially late transition metal oxides such as Fe, Co and Mn oxides have been given particular attention due to their stable multiple oxidation states, yielding numerous oxides of the same material. However, these materials have weak inorganic-surfactant interactions, which make the synthesis of mesoporous structures of these materials difficult by conventional approaches.[3] Therefore, a novel approach which can be used to synthesize tunable mesoporous transition metal oxide materials is highly desirable. This thesis describes the synthesis of mesoporous late transition metal oxides by a newly developed soft template method and their catalytic applications.

1.2 Synthesis of Mesoporous Cobalt Oxides for Low Temperature Carbon Monoxide Oxidation Applications

The oxidation of carbon monoxide (CO) to carbon dioxide (CO_2) has been extensively studied for the past decades due to its many potential applications in air purification, automobile exhaust gas treatment, purifying H_2 in polymer electrolyte fuel cells, closed-cycle CO_2 lasers, and CO gas sensors.[4-6] CO oxidation has also been used as a model reaction for mechanistic studies

due to the simplicity of reactants involved. Moreover, in practical applications, especially automotive emission control, large amounts of CO are usually generated during the cold start period, which causes serious environmental problems. Therefore, it is of great necessity to regulate the CO emission by developing efficient catalysts that convert CO into CO_2 at relatively low temperatures. In the past two decades, noble metals have been discovered to function as high performance oxidation catalysts for various industrial relevant reactions including CO oxidation and the reaction temperature for complete oxidation has been significantly reduced. Haruta et al. was the first to report total conversion of CO oxidation at temperatures as low as -70ºC by using supported gold nanoparticles.[7] However, their high cost and scarcity make noble metal catalysts less desirable. A great deal of research has thus been devoted to search for and develop cost effective catalysts which are noble metal free but are able to deliver comparable catalytic performances. Transition metal or composite transition metal oxides represent promising candidates since they are cheap, earth abundant, and capable of low temperature catalytic conversion.[5, 8-10] Among these, Co_3O_4 stands out due to its high activity for CO oxidation at temperatures far below room temperature.

In this study, crystalline mesoporous cobalt oxides were synthesized using a recently discovered approach. This approach involves the use of inverse surfactant micelles. The sol-gel process of cobalt sols was controlled by NO_x chemistry. The materials are monodispersed nanoparticle aggregates and the mesopores are formed by connected intraparticle voids. The effect of heat treatment (150 - 450 ºC) on structural parameters (pore size, pore volume, surface area) and catalytic activity towards CO oxidation is discussed in detail. Powder X-ray diffraction (PXRD), N_2 sorption, field emission scanning electron microscope (FE-SEM) and high-resolution transmission electron microscopy (HR-TEM) revealed that both pore and nanoparticle sizes are

enlarged with increasing thermal treatment temperatures (150 to 450ºC). Mesoporous cobalt oxide calcined at 350ºC exhibited the best oxidation activity and can achieve complete oxidization (100% conversion) of CO to CO_2 at -60ºC under normal conditions (~ 3-10 ppm H_2O) and at 80ºC under moisture rich conditions (~ 3% H_2O). The commercial Co_3O_4 reached 100% conversion at 220ºC under normal conditions. X-ray photoelectron spectroscopy (XPS), O_2-temperature programmed desorption (O_2-TPD), H_2-temperature programmed reduction (H_2-TPR), CO-TPD and N_2 sorption analyses indicated that the surface oxygen vacancy and large surface area promoted the lattice oxygen mobility of the catalysts and further enhanced their catalytic performance. Lattice oxygen participation confirmed by CO-TPD suggests the reaction proceeds via the Mars-van Krevelen mechanism through a redox cycle. TPD tests after catalyst deactivation under normal conditions were investigated. Water accumulation and carbonate species formation during the reaction that block the surface active sites are proposed to be responsible for catalyst deactivation, but their activities can be easily restored by expelling water and carbonates at moderate temperature (200ºC).

1.3 Mesoporous Metal Oxides on Cordierite Monolithic Substrate for Exhaust After-Treatment

Nowadays environmental and air pollution problems have become one of the major concerns of human beings. Consequently air purification devices are highly demanded. Among all the harmful substances emitted into air, large amounts of pollutants are coming from automobile exhaust gas emissions. To minimize the toxic gas emission from vehicles, internal combustion engines are equipped with catalytic converters. With a proper catalyst inside, catalytic converters are able to convert carbon monoxide, hydrocarbons, and nitrogen oxides to less toxic gases such as carbon dioxide and nitrogen. However several issues remain with the development of emission control devices. First, the use of precious metal catalysts make it challenging for large scale

commercialization. The search for low cost alternatives has become a top priority in the past decade.[10, 11] Additionally, in practical use, structured catalysts are preferable over powder based catalysts. In automobile catalytic converters, ceramic cordierite ($2MgO{\cdot}2Al_2O_3{\cdot}5SiO_2$) monoliths are the most widely used substrates. The honeycomb like structure with parallel channels inside is the general structure. Cordierite has several outstanding merits including low pressure drop, excellent thermal and mechanical shock resistance, efficient mass transfer, good porosity, enough refractoriness and low catalyst usage.[12, 13] Therefore, an efficient method to deposit active catalysts onto the substrate without losing its original physicochemical properties and activities is highly necessary. Lastly, the detailed investigation of intrinsic determining parameters which can have a great impact on the catalytic activities is lacking in the literature.

In this study, a newly developed soft template approach for synthesizing mesoporous materials (named as UCT method) is used to in-situ coat the efficient metal oxide catalysts on cordierite honeycomb substrates. This method involves the use of inverse micelles. Metal oxo-clusters were confined in the micelle nano reactor to eliminate the effect of water and prevent particle aggregation. The formed materials have ordered mesopores and high thermal stability. More importantly, this method is generic and can be used to synthesize a large group of mesoporous materials from different parts of the periodic table. Herein, three metal oxides, manganese oxide, cobalt oxide and cerium oxide are chosen. They all have different stable forms of oxidation states, which equipped them with excellent redox properties originating from their multivalent nature. The low redox potentials also lead to outstanding catalytic activities for oxidation reactions. By using the UCT synthesis method, mesoporous manganese oxide, cobalt oxide and cerium oxide were in-situ coated on cordierite substrate. The as-prepared monolithic catalysts showed promising activities for the CO oxidation reaction. Moreover, in-situ coated

samples have better activities compared to that of dip coated samples. The advantage of an in-situ coating process is also demonstrated in the aspect of coating layer robustness. All the in-situ prepared materials have more than 90% weight maintained after 20 min sonication in ethanol, while more than 65% weight loss was observed for the dip coated sample.

1.4 Ni and Mn-Substituted Mesoporous Co_3O_4 as Bifunctional Catalysts for Oxygen Reduction Reaction and Oxygen Evolution Reaction

The development of highly efficient alternative energy conversion and storage systems has been greatly inspired by the exponentially increasing energy consumption.[14-16] Extensive research has been focused on the electrochemical oxygen reduction reaction (ORR) and the oxygen evolution reaction (OER), the two key reactions in metal-air batteries, fuel cells, electrochemical water splitting and solar fuel production.[17-19] Dai et al. recently reported a direct relationship between high ORR activity and favorable discharge performance of the Li-O_2 batteries in both aqueous and non-aqueous medium.[20] The best catalyst known so far for ORR is based on platinum (Pt) while iridium (Ir) and ruthenium (Ru) oxides are considered as the most active for OER. However they only have moderate activities for the reverse reactions.[21-23] Therefore, the design of efficient bifunctional catalysts for both OER and ORR remains challenging and is highly demanding due to their potential applications in unitized regenerative fuel cells (URFCs) and rechargeable metal-air batteries.[24-26] In addition to the high cost, noble metal based catalysts also suffer from limited stability. Especially in alkaline solutions, particle degradation, dissolution and aggregation make them less desirable for practical applications.[27] Consequently, much effort has been put to search for cost effective, earth abundant and environmentally benign noble metal free catalysts with high electrochemical activities and superior stabilities. In this context, ORR and OER under alkaline conditions has been extensively studied since this opens up possibilities for a

large spectrum of materials including transition metal oxides and sulfides,[28, 29] perovskites,[30, 31] and metal oxides/graphene or carbon nanotube hybrid materials.[27, 32] Among these materials, spinel cobalt (II, III) oxide has become one of the most extensively studied electrocatalysts for both ORR and OER reactions due to the excellent redox properties originating from its multivalent nature.[33-37]

Herein, we report a one-step wet-chemical synthesis of Ni and Mn-substituted mesoporous cobalt oxides through an inverse micelle method. Various characterization techniques including PXRD, N_2 sorption, TEM and SEM confirmed the successful incorporation of Ni and Mn leading to the formation of Co-Ni(Mn)-O solid solutions with retained mesoporosity. Among these catalysts, cobalt oxide with 5% Ni doping demonstrated the best activity for both ORR and OER, with an overpotential of 399 mV for ORR (at 3 mA/cm^2) and 381 mV (at 10 mA/cm^2) for OER, which is on a par with the benchmark Pt/C and Ir/C catalysts. Furthermore, 5% Ni-doped Co_3O_4 demonstrated better durability than the precious metals featuring little activity decay observed throughout 24 hours continuous operation for both ORR and OER. Analyses of Cyclic Voltammetry, XPS, Raman and O_2-TPD reveal that the redox activity of Co^{3+} to Co^{4+} is crucial for OER performance, while the population of surface oxygen vacancies and surface area determine their ORR activity. The comprehensive investigation of the intrinsic active sites for ORR and OER by correlating different physicochemical properties such as surface area, surface oxidation states, and structural defects with the electrochemical activities is believed to provide important scientific insight toward the rational design of high performance electrocatalysts for ORR and OER reactions.

CHATPER 2. MESOPOROUS Co_3O_4 WITH CONTROLLED POROSITY AS EFFICIENT LOW TEMPERATURE CARBON MONOXIDE OXIDATION CATALYST

2.1 Introduction

Considerable work has been done towards low temperature CO oxidation over Co_3O_4 based materials. Thormahlen et al.[5] prepared an aluminum supported Co_3O_4 catalyst, which exhibited a light off temperature T_{50} of -63ºC after a preoxidation step. Xie et al.[8] synthesized Co_3O_4 nanorods with predominantly exposed {110} planes, which can completely oxidize CO to CO_2 at -77ºC under a normal feed gas. Jia et al.[27] reported low temperature CO oxidation under normal conditions with 100% conversion at -76ºC achieved by using Co_3O_4-SiO_2 nanocomposites. However, these catalysts need to be activated in oxidizing atmospheres prior to catalytic tests. They also need relatively high pretreatment temperatures (>350 ºC) in order to fully oxidize CO at low temperatures. Pretreatment in an oxidizing atmosphere has a chance of partially oxidizing the catalyst[38] and the preadsorbed labile O_2 on the catalyst surface can enhance the oxidation of CO at low temperatures. Therefore the catalytic performance of the catalysts cannot be truly revealed. One drawback of Co_3O_4 based catalysts for CO oxidation is their low water tolerance. They are quickly deactivated by the presence of moisture in the gas stream, thus placing a new demand for highly active moisture tolerant catalysts. Several attempts were made to solve this problem, including polydimethylsiloxane (PDMS) coating of the oxide surface[39] and incorporation of CeO_2.[40] Nevertheless, the activity under moisture rich conditions is still far lower than those under normal or dry conditions. Therefore, the design for noble metal free hydrophobic catalysts still remains as a challenge.

Since the pioneering work of Mobil Oil researchers[41], mesoporous materials have attracted tremendous attention in many different catalytic systems such as catalysis, sorption, gas sensors, and optics. Their catalytic activities have been reported to exceed their nonporous counterparts due to their high surface area, nanocrystallinity, mesoporosity, and pore volume.[42-44] So far to our knowledge, most studies of mesoporous transition metal oxides are focused on groups I-IV metals, including Ti, V, Nb, Cr, W.[45-47] These metals have strong interactions with polyethylene oxide groups on surfactants by accepting electrons into their empty d orbitals.[3] Late transition metals with filled or half-filled d orbitals do not have such interactions. Poor control of the solvent involved interactions is another reason why the synthesis of mesoporous late transition metal oxides remains challenging. Recently, our group has successfully synthesized a series of mesoporous materials, which are named UCT materials (University of Connecticut mesoporous materials).[48] Instead of conventional approaches, an inverse surfactant (Pluronic, P123) micelle was used as a soft template to create the mesopores. The sol-gel process was controlled by unique NOx chemistry. Subsequently treating the materials with different heating cycles yielded monomodal, thermally-controlled mesoporous materials with crystalline walls. The approach enables one to prepare mesoporous materials for a wide variety of elements from the periodic table including transition metal oxides (Fe, Co, Ni, Mn, Ti, Zr), metalloids (SiO_2), nonmetals (C), lanthanides (CeO_2) and TM sulfides (CdS and ZnS). Specifically, herein we report the preparation of mesoporous Co_3O_4 (UCT-8), which is difficult to produce using conventional methods[49], and use as a highly active catalyst for low temperature CO oxidation. The synthesized mesoporous Co_3O_4 showed promising activity in CO oxidation under both normal conditions (~3-10 ppm H_2O) and moisture rich conditions (~3% H_2O). Mild pretreatment conditions under an inert atmosphere at 200^{o}C and low oxygen content (1%) were used. The materials were characterized by PXRD, N_2

sorption, XPS, HR-TEM, H_2-TPR, and TPD to examine the effect of heating cycles on the material properties. Surface lattice defects and surface areas were found to greatly influence the catalytic activity.

2.2 Experimental Section

2.2.1 Catalyst Synthesis

All chemicals used were reagent-grade. Cobalt (II) nitrate hexhydrate ($Co(NO_3)_2 \cdot 6H_2O$, ≥98.0), 1-butanol (anhydrous, 99.8%) and Poly(ethylene glycol)-block-Poly(propylene glycol)-block-Poly(ethylene glycol) PEO_{20}–PPO_{70}–PEO_{20} (Pluronic P123) were purchased from Sigma-Aldrich. Concentrated nitric acid (68%-70% HNO_3) was purchased from J. T. Baker. To synthesize the mesoporous Co_3O_4, 5 g (0.017 mol) of $Co(NO_3)_2 \cdot 6H_2O$ was dissolved in a solution containing 17 g (0.33 mol) of 1-butanol, 2.4 g (0.038 mol) of HNO_3 and 2.5 g (4.31×10^{-4} mol) of P123 in a 400 mL beaker. After magnetic stirring at room temperature, a clear gel was formed. The clear gel was then placed in an oven at 120ºC for 3.5 h. The obtained powder was washed with ethanol several times, centrifuged and dried in a vacuum oven. The powders were calcined at 150ºC for 12 h (designated UCT-7), and further heated to 250ºC, 350ºC, and 450ºC respectively for 1 h with a heating rate of 1ºC/min (designated UCT-8). All the heating cycles were done under air. Samples were nominated as Meso-Co-X (X=150, 250, 350 and 450), representing samples heat treated at 150ºC, 250ºC, 350ºC, and 450ºC respectively. Commercial Co_3O_4 (C-Co_3O_4) from Strem Chemical Inc. was 99.5% in purity and used as received.

2.2.2 Materials Characterizations

Powder X-ray diffraction (PXRD) analyses were performed on a Rigaku Ultima IV diffractometer with Cu Kα radiation (λ = 1.5406 Å) at room temperature. The operating voltage

was 40 kV and the current was 40 mA. Both low angle (2θ = 0.5° - 8°) and wide angle (2θ = 5° - 75°) diffraction patterns were measured. N_2 sorption measurements were performed on a Quantachrome Autosorb-1-1C automated sorption system. The samples were degassed at 200ºC for 4 h (120ºC, 4 h for UCT 7) prior to the experiments. The surface areas were calculated by the Brunauer-Emmett-Teller (BET) method and the pore size distributions were obtained by the Barrett-Joyner-Halenda (BJH) method from the desorption branch of the isotherms. The morphologies of the samples were investigated with a Zeiss DSM 982 Gemini field emission scanning electron microscope (FE-SEM) with a Schottky emitter at an accelerating voltage of 2.0 kV and a beam current of 1.0 mA. Samples were dispersed in methanol and mounted on silicon wafers. High-resolution transmission electron microscopy (HR-TEM) images were collected with a JEOL 2010 FasTEM microscope operating at 200 kV. The samples were prepared by using a focused-ion-beam (FIB) technique to make them thin enough to be observed by HRTEM. The X-ray Photoelectron Spectroscopy (XPS) analyses were conducted on a PHI model 590 spectrometer with multiprobes (ΦPhysical Electronics Industries Inc.). Al-Kα radiation (λ= 1486.6 eV) was used as the radiation source. Fourier Transform Infrared Spectroscopy (FT-IR) were collected using a Nicolet Magna 560 spectrometer equipped with TGS detector. Sixty four scans were collected at 4 cm^{-1} spectral resolution. Pellets were made by diluting samples in KBr.

Temperature-programmed mass spectrometry analyses were conducted in a programmable tube furnace equipped with a gas analyzer MKS coupled with a quadruple mass selective detector. About 100 mg (200 mg for O_2-TPD) of materials were packed in a quartz tube reactor mounted into the tube furnace. The loaded samples were pretreated in an inert gas flow (Ar) at 200ºC for 1 h to clean the catalyst surface before each test. Temperature programmed measurements were performed from room temperature to 800ºC with a heating ramp rate of 10ºC/min. In H_2-TPR

measurements, 10% H_2/N_2 flow was passed through the catalyst bed at a flow rate of 50 sccm, while the temperature was ramped from room temperature (RT) to 600ºC. In CO-TPD measurements, samples were first exposed to 10% CO/He at room temperature for 1 h. Then the samples were purged with Ar for 30 min to remove any surface physisorbed gases and residual feed gas from the streams. After purging, the samples were heated under argon flow from RT to 600ºC. By replacing the 10% CO/He with pure O_2, O_2-TPD was conducted from RT to 800ºC. The flow rate was 200 sccm. TPD measurements under inert atmosphere after deactivation were also measured. The reaction gas mixture (1% CO, 1% O_2/N_2) was passed through the catalyst bed with 200 sccm flow rate for 15 h to ensure complete deactivation. Subsequently, the catalyst was purged with argon for 30 min to remove any residual gases. After that, the sample was heated from room temperature to 600ºC under an Ar flow (200 sccm).

2.2.3 Catalytic Tests

CO oxidation was carried out in a continuous flow fixed bed quartz tubular reactor under atmospheric pressure. About 100 mg of as-prepared catalyst was used for each test. Before the measurement, the catalysts were pretreated under helium flow (15 sccm) for 1 h at 200ºC (120ºC for UCT-7) to clean the catalyst surface. After cooling down, a gas mixture of 1% CO, 1% O_2 balanced in N_2 was passed through the catalyst bed with a flow rate of 20 sccm. The outlet gas streams were analyzed by an online gas chromatograph (SRI 8610C Multiple Gas Analyzer #1 GC) equipped with a thermal conductivity detector (TCD), a 6 foot long molecular sieve 13X packed column, and a 6 foot long silica gel packed column. The reaction temperature was measured using a K-type thermocouple inserted directly into the catalyst bed. Temperatures below 0ºC were achieved by mixing dry ice and ethanol in a Dewar flask. GC samples were injected after 10 min stabilization at any given temperature. The reaction conversion was calculated based on the CO

concentration, N_2 was used as an internal standard. Normal condition (~ 3-10 ppm H_2O) was obtained by using the as-mixed normal feed gas. Moisture rich condition was obtained by passing the feed gas through a water bubbler at room temperature (~ 3% water vapor).

2.3 Results

2.3.1 Physicochemical Properties

2.3.1.1 PXRD and TEM

Figure 2.1 shows both high (a) and low angle (b) PXRD patterns of mesoporous cobalt oxide materials calcined at different temperatures. All the materials, except Meso-Co-150°C, had a typical spinel Co_3O_4 crystalline pattern according to JCPDS (# 090418). Increasing heat treatment temperature (250 to 450°C) resulted in patterns with sharper diffraction lines, which indicated that the particle grain sizes were increased. Compared to commercial Co_3O_4 sample (C-Co_3O_4), however, Meso-Co-X materials have much smaller grain sizes. Using {311} planes of Co_3O_4 for grain size calculation by the Scherrer equation, the particle grain sizes of Meso-Co-X samples are in the range of 8.25 to 19.57 nm, while commercial Co_3O_4 has a particle size of 89.25 nm. The PXRD pattern of Meso-Co-150 showed a mixed phase consisting of $C_4H_6CoO_4{\cdot}4H_2O$ and Co_3O_4. The crystal structure was totally transformed to Co_3O_4 after a heat treatment at 250°C.

Figure 2.1b gives the low angle diffraction lines of cobalt oxide samples. Meso-Co-250 and Meso-Co-350 diffracted in the low angle region, indicating the existence of a mesostructure, like other UCT materials[48, 50]. While Meso-Co-150 and Meso-Co-450 as well as the commercial Co_3O_4 failed to show a diffraction line in low angle PXRD. The low angle PXRD diffraction line position for Meso-Co-350 shifted to a smaller 2θ value compared to Meso-Co-250, which further confirms the fact that the particle size of UCT materials expands with increasing heat treatment

temperature. According to the model of UCT materials, low angle diffraction line positions correspond to the average particle size. Therefore, Meso-Co-450 could still have a mesostructure, but the diffraction line position might shift to lower angle that is beyond the detection limit.

The change of the nanoparticle sizes upon heat treatment was also observed in TEM analyses (Figure 2.1c-e). The nature of the particles is a nanoparticle aggregate, the same as other UCT materials. All TEM images were collected with the same magnification for better evaluation of the change of the particle sizes with different heat treatment. With calcination temperature increasing from 250 to 450°C, the particle size changed from 11.4 to 21.7 nm, which corresponds well with the tendency revealed by low angle PXRD characterization.

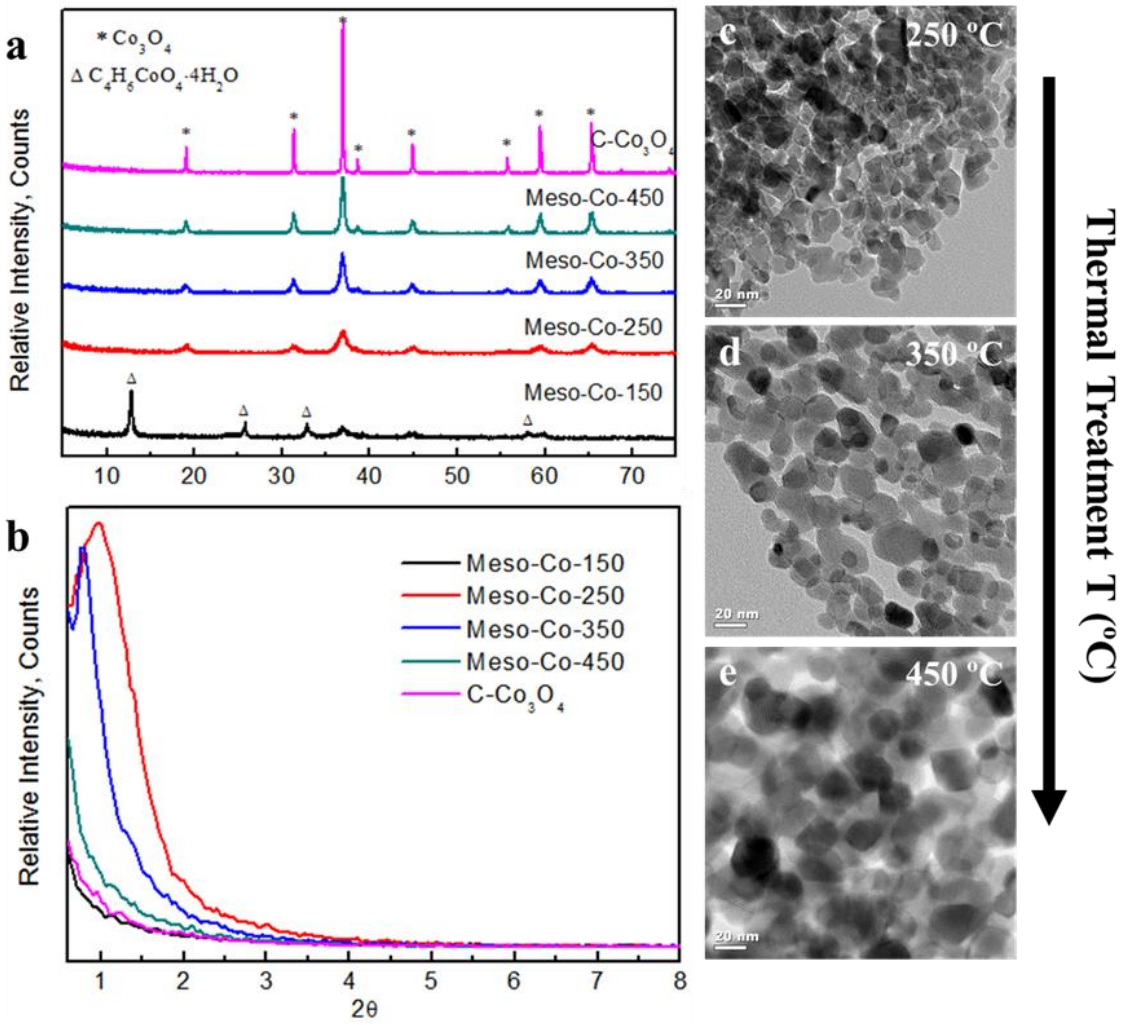

Figure 2.1 Characterizations of as-prepared materials. (a) Low angle and (b) Wide angle PXRD patterns of Meso-Co-X (X=150, 250, 350 and 450) and commercial Co_3O_4 (C-Co_3O_4) samples. TEM images of (c) Meso-Co-250, (d) Meso-Co-350 and (e) Meso-Co-450 showing particle growth (scale bar, 20 nm).

2.3.1.2 N_2 Sorption

Similar to the trend found in PXRD, Barrett-Joyner-Halenda (BJH) desorption pore diameters built up from 1.9 to 17.5 nm with the final heat treatment temperature increasing from 150°C to 450°C, as shown in Figure 2.2b. The Meso-Co-150 sample demonstrated its nonporous nature (Type III isotherm) while Meso-Co-250 and Meso-Co-350 showed a characteristic Type IV adsorption isotherm, followed by a Type I hysteresis loop (Figure 2.2a), suggesting the existence of a regular ordered mesoporous structure[48]. These two materials also have very high surface areas (> 100 m^2g^{-1}) and large pore volumes (> 0.349 $cc \cdot g^{-1}$). Meso-Co-450 showed a further expansion in pore size and the BJH desorption pore size distribution still suggests a uniform porous structure (17.5 nm). However the surface area decreased significantly compared with Meso-Co-250 and Meso-Co-350. Such phenomenon proves the successful synthesis of UCT-8 materials whose particle sizes, pore diameters and pore volumes can be tuned by heat treatment at different temperatures. The BET surface area, BJH pore volume and other structural parameters are summarized in Table 2.1.

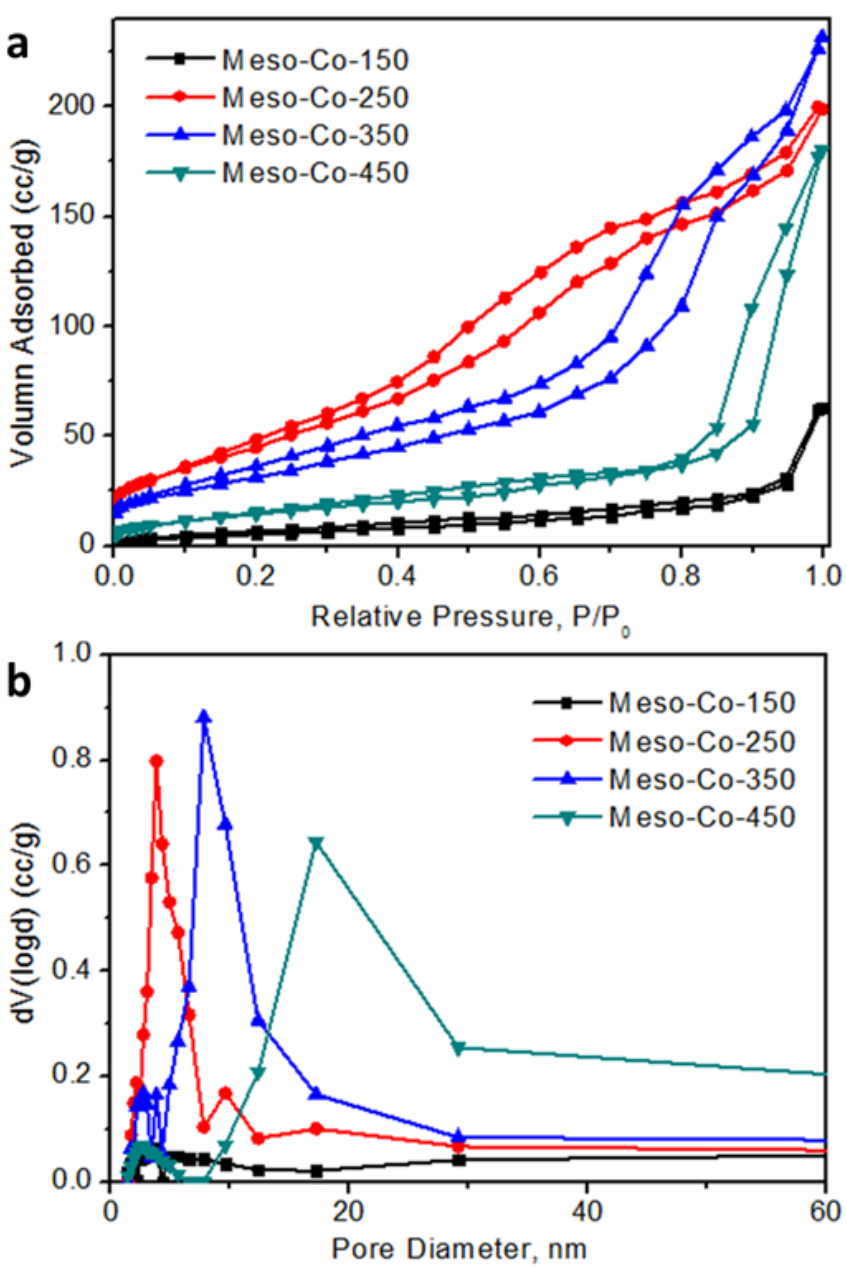

Figure 2.2 BET measurements. (a) N_2 sorption isotherms and (b) BJH desorption pore size distributions of Meso-Co-X (X=150, 250, 350 and 450).

Table 2.1 Structural parameters and catalytic performance of different catalysts discussed in this chapter.

Heat Treatment T (ºC)	BET Surface Area (m^2/g)	BJH Des. Pore Volume (cm^3/g)	BJH Des. Pore Diameter (nm)	Low Angle Diffraction Position (nm)	Crystal Structure	T_{100}*
150ºC	22.9	0.10	1.9	--	Co_3O_4 & $C_4H_6CoO_4 \cdot 4H_2O$	180ºC
250ºC	181.4	0.35	3.8	9.29	Co_3O_4	35ºC
350ºC	120.8	0.38	7.7	11.03	Co_3O_4	60ºC
450ºC	57.9	0.29	17.5	--	Co_3O_4	0ºC

* T_{100}: The temperature where full conversion of CO to CO_2 takes place.

-- Signifies not applicable

2.3.1.3 Electron Microscopy

Morphological properties of mesoporous cobalt oxides were investigated by field emission scanning electron microscope (FE-SEM) and high-resolution transmission electron microscopy (HR-TEM). Figure 2.3a-d shows SEM images of Meso-Co-X (X=250, 350, 450) samples. The samples are flower-like round particles consisting of nanosize plates. Meso-Co-150 also consists of flower like round particles but fails to show a uniform morphology due to incomplete transformation to the Co_3O_4 phase (see Figure 2.3a). The pore openings also expanded with heat treatment. In Meso-Co-450, uniform pores can be clearly seen in the images. High-resolution transmission electron microscopy (HR-TEM) images are shown in Figure 2.3e-g. The obtained mesoporous cobalt oxides with crystalline walls exhibited well-defined lattice fringes. The d-spacing values are measured to be 0.28 nm, 0.24 nm, and 0.47 nm, corresponding to {220}, {311} and {111} planes of the Co_3O_4 spinel structure, respectively. In spinel cobalt oxide, Co^{3+} occupies octahedral sites coordinating with six oxygen atoms while Co^{2+} possesses tetrahedral sites with four neighboring oxygen atoms. Crystallography studies of the spinel cobalt oxide lattice suggest that Co^{3+} is highly populated within {110} planes while {111} planes contain Co^{2+} only.

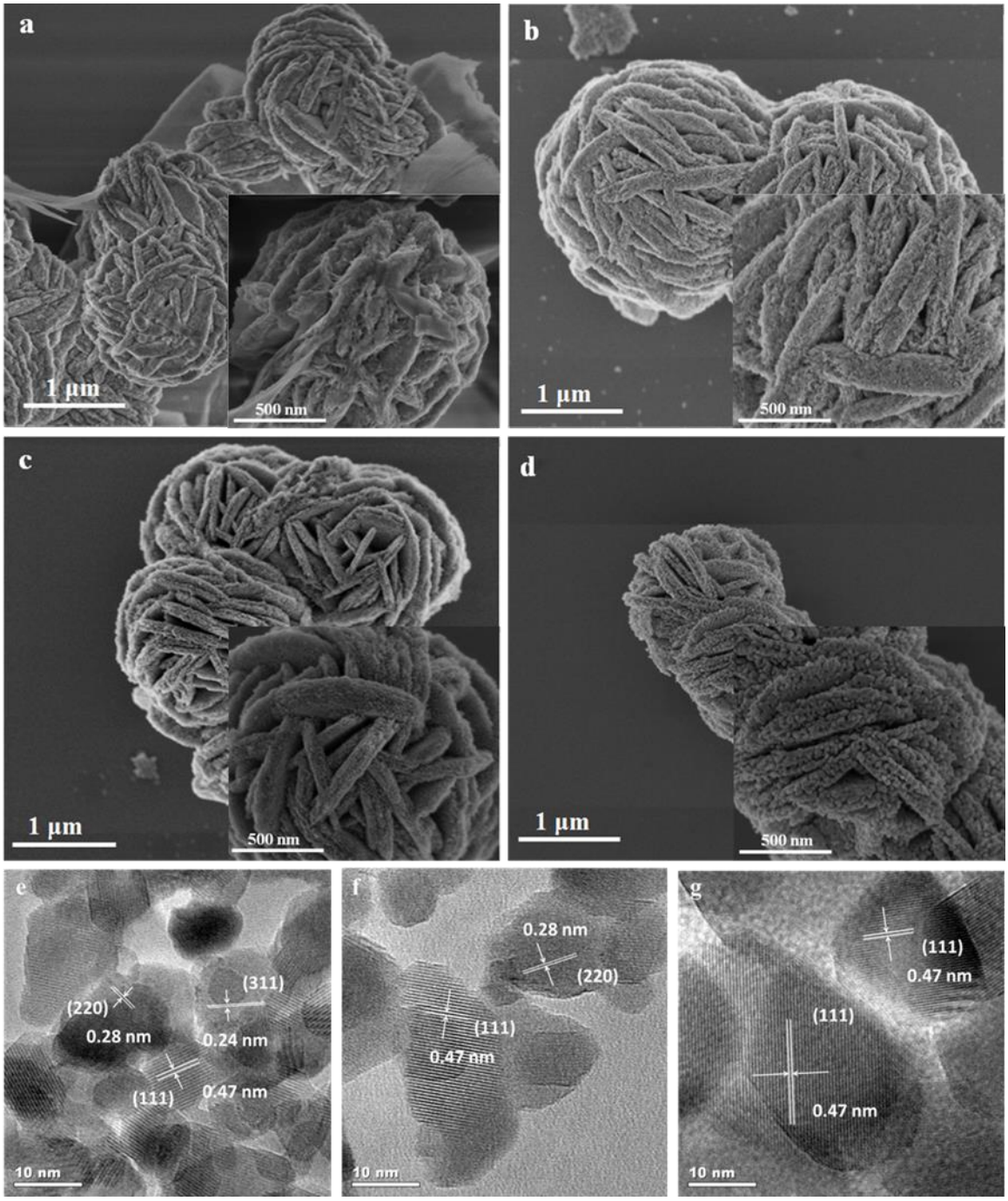

Figure 2.3 Electron microscopy images. FESEM micrographs of catalysts heat treated at (a) 150°C, (b) 250°C, (c) 350°C and (d) 450°C. HRTEM images of meso-Co at (e) 250°C, (f) 350°C and (g) 450°C.

2.3.2 CO Oxidation Reaction Activities

Figure 2.4 shows the catalytic performance towards carbon monoxide oxidation under various conditions of Meso-Co-X samples. Performance of commercial Co_3O_4 (C-Co_3O_4) is also included for comparison. Figure 2.4a gives the activity behavior under normal conditions (~ 3-10 ppm H_2O). Among these materials, Meso-Co-350 was the best catalyst and completely oxidized carbon monoxide at temperatures as low as -60ºC. Meso-Co-250 showed slightly lower activity with the temperature of 100% conversion (T_{100}) at -35ºC. Compared to Meso-Co-250 and Meso-Co-350, Meso-Co-450 could only oxidize CO completely at 0ºC. However, its catalytic activity was still much higher than that of the commercial Co_3O_4, which exhibited no conversion at temperatures below 120ºC and did not fully convert CO to CO_2 until the temperature reached 220ºC. On the other hand, Meso-Co-150 did not start to convert CO until 120ºC, and then the conversion increased rapidly and reached 100% at 180ºC. The behavior suggested that the catalyst may undergo phase transformation in the temperature range of 120-180ºC. Since Meso-Co-350 exhibited the best catalytic performance, this material was selected for long term durability tests. The results are demonstrated in Figure 2.4b. The catalyst maintains 100% conversion for 11 consecutive hours at room temperature. After 14 hours the sample was totally deactivated and was regenerated under helium flow at 200ºC for 1 h. Upon regeneration the activity was fully recovered and became even better compared with the fresh-prepared sample. No activity loss was observed for 13 h.

CO oxidation under moisture rich conditions (~ 3% H_2O) was also performed. After sending about 3% moisture into the feed gas stream, T_{100} of the catalysts shifted to higher temperatures (Figure 2.4c). Meso-Co-350 still exhibited the best performance with 100% conversion at 80ºC. T_{100} of Meso-Co-250 and Meso-Co-450 were 120ºC and 140ºC, respectively.

Stability tests under moisture rich condition are shown in Figure 2.4d. At 150ºC, both Meso-Co-250 and Meso-Co-350 maintained 100% CO conversion for 24 hours. However at 100ºC, Meso-Co-350 gave 100% conversion initially, then the CO conversion tended to decrease, but still remained > 50% conversion after 24 h. CO oxidation in moisture rich conditions over metal oxides was previously studied by several other research groups[8, 39, 40, 51, 52]. Xie et al. obtained ~92% conversion at 150ºC with 8.20 vol% H_2O in the gas stream[8]. Kuo et al. synthesized Co_3O_4 nanoparticles on carbon nanotube with polymer coating and reached 100% conversion at 150ºC with ~3% moisture[52]. Chen et al. prepared several metal oxides and coated them with hydrophobic polymer PDMS. The best performance in the gas stream containing ~3% moisture was achieved by PDMS coated amorphous manganese oxide, which showed CO conversion of 63% at 100ºC and reached a total conversion at 130ºC[39]. Compared to literature findings, the results presented here are promising.

Figure 2.5 shows the PXRD pattern of Meso-Co-150 before and after reaction. The sample was transformed from $C_4H_6CoO_4{\cdot}4H_2O$ to a Co_3O_4 spinel phase during the reaction. Also the color of the catalyst changed from pink to black. The decreased O_2 concentration but increased CO_2 concentration detected in the outlet gas at 160ºC indicated the remaining carboxyl groups in the catalyst have been transformed into CO_2. Similar behavior of carboxyl and nitrate groups removal of UCT materials monitored by TPD was reported[48]. When the temperature was elevated above 160ºC, the residues in the sample started to be removed gradually and thus more active sites were exposed leading to the rapidly developing catalytic activity of Meso-Co-150 in the range of 140-180ºC. Thermogravimetric analysis of the sample confirmed a significant weight loss at around 210ºC in air. Therefore the complete oxidation of CO can be achieved upon the removal of the residues at around 200ºC.

Morphologies of Meso-Co-350 after stability test under normal conditions are shown in Figure 2.4e-g. No obvious morphological change from either FE-SEM or HR-TEM images was observed as compared to the fresh catalyst. The HR-TEM image still displayed clear lattice fringes of Co_3O_4 which confirmed there is no phase transformation or segregation. This result indicated the catalyst was able to maintain its structural integrity and experienced no physical damage throughout the long-term reaction.

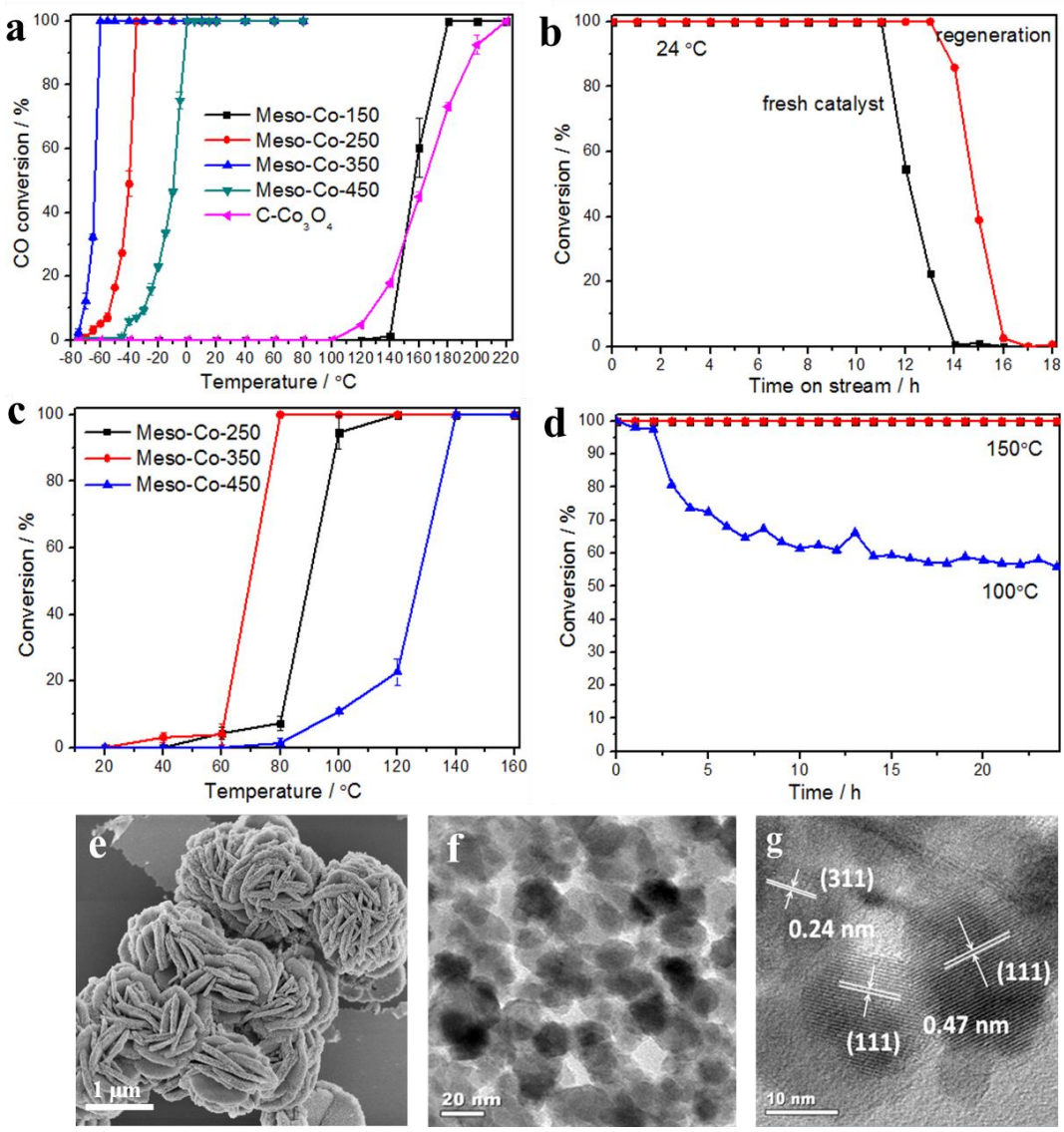

Figure 2.4 Catalytic performance towards CO oxidation. (a) CO light off of Meso-Co-X (X=150, 250, 350 and 450) as well as C-Co_3O_4 and (b) Long-term durability test of Meso-Co-350 at room temperature under normal conditions (~3-10 ppm H_2O). (c) and (d): CO light off plot of Meso-Co-X (X=250, 350 and 450) and stability test of Meso-Co-350 and Meso-Co-250 under moisture rich conditions (~3% H_2O). (e-g) FE-SEM, TEM and HR-TEM images of Meso-Co-350 after stability test under normal conditions.

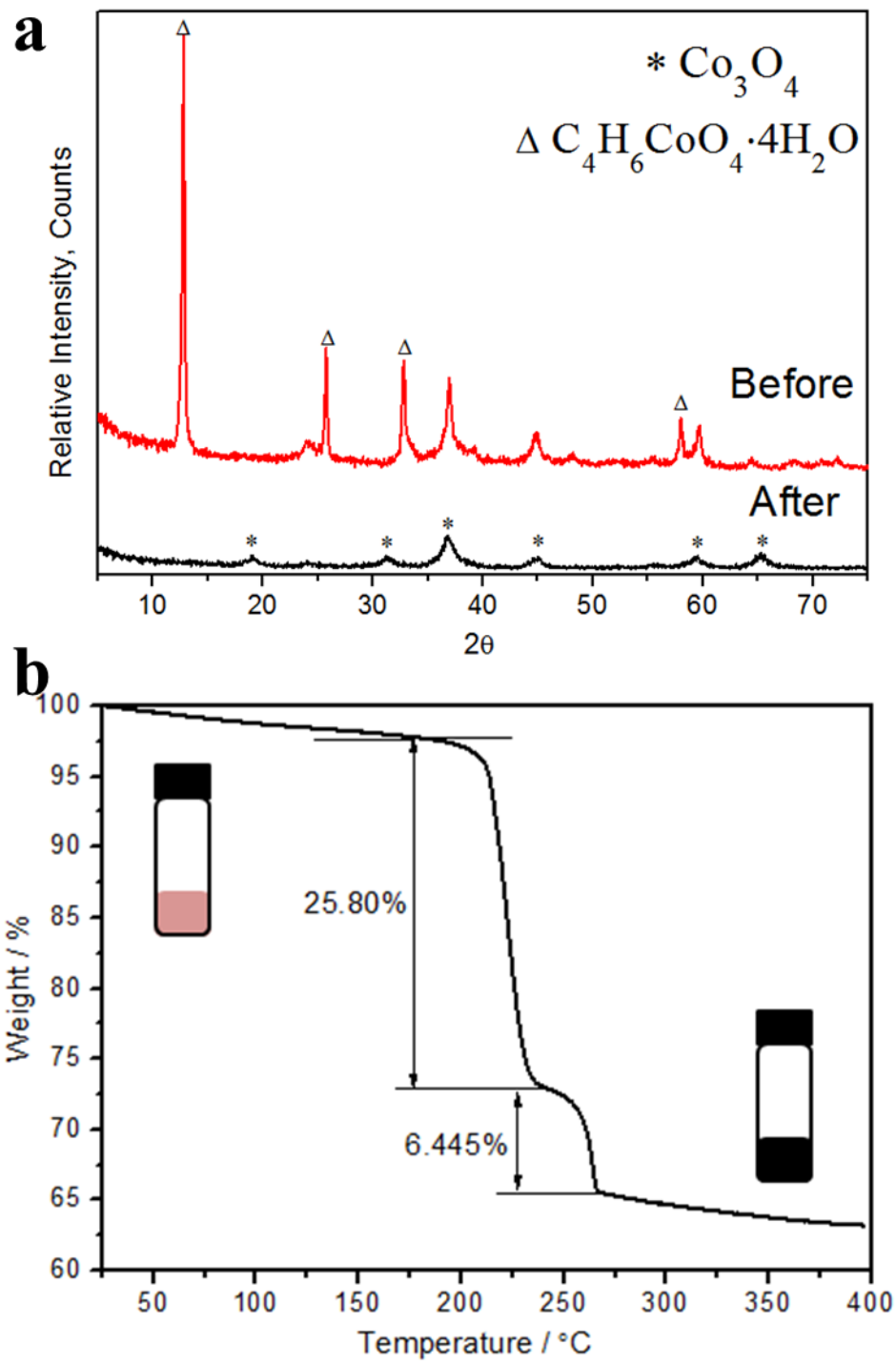

Figure 2.5 (a) PXRD patterns of Meso-Co-150 before and after reaction. (b) Thermogravimetric analysis (TGA) of Meso-Co-150.

2.3.3 X-ray Photoelectron Spectroscopy (XPS)

For Co_3O_4 catalysts, higher surface area can contribute to higher catalytic activity due to more exposed active sites and weakened Co-O bond strength[53, 54]. Since Meso-Co-250 has the highest surface area but is not the most active catalyst (Table 2.1), the differences of catalytic performances of these materials cannot be solely contributed to effects of surface area. Other factors such as surface properties and metal valence states need to be considered. A useful technology to study the surface chemistry of the catalysts is X-ray Photoelectron Spectroscopy (XPS). The XPS spectra of Meso-Co-X (X=250, 350 and 450) as well as Meso-Co-350* (Meso-Co-350 after stability tests under normal conditions) are shown in Figure 2.6. The Co $2p_{3/2}$ and Co $2p_{1/2}$ peak positions located at around 780 eV and 795 eV (Figure 2.6a) are in good agreement with the presence of Co_3O_4[27, 55, 56]. The Co 2p spectra were further deconvoluted into Co^{2+} and Co^{3+} signals, respectively as shown in Figure 2.6a. Co 2p peaks at binding energies of ~779 eV and 795 eV are characteristic of Co^{3+}, while the peaks at ~781 eV and 797 eV correspond to Co^{2+} [33, 57, 58]. Different surface oxygen species have been identified by the deconvoluted O 1s spectrum. The asymmetry of the O 1s peak on higher binding energy side suggested the existence of surface adsorbed oxygen containing species. Specifically, the fitted O 1s spectra displayed four major oxygen contributions with the corresponding peaks centered at ~529 eV, 530 eV, 532 eV, and 533 eV. These bands can be attributed to Co-O bonds (O_L), hydroxyl (O_{OH}), oxygen vacancies (vO_2), and chemisorbed water (O_{mw}), respectively. Peak area percentages of these four different oxygen components are listed in Table 2.2. The Co^{2+}/Co^{3+} ratios of cobalt oxides heated from 250 to 450ºC were calculated to be 0.42, 0.53 and 0.39 respectively, among which Meso-Co-350 had the highest amount of Co^{2+} (23.1%) and exhibited the most abundant oxygen vacancies (25.1%) on the surface.

After stability tests, the surface composition of Meso-Co-350 did not change a lot compared to the fresh catalyst, with 22.6% Co^{2+} and 23.0% oxygen vacancies remaining on the surface.

Table 2.2 Summary of area percentages of different elemental components obtained from the deconvoluted spectra.

%Area / Sample	Co $2p_{3/2}$		O 1s			
	Co^{2+}	Co^{3+}	O_{mw}	vO_2	O_{OH}	O_L
Meso-Co-250	19.7	46.9	4.7	15.4	30.2	49.7
Meso-Co-350	23.1	43.6	9.5	25.1	29.7	35.8
Meso-Co-450	18.8	47.8	5.6	14.9	28.0	51.5
Meso-Co-350*	22.6	44.0	6.5	23.0	33.9	36.6

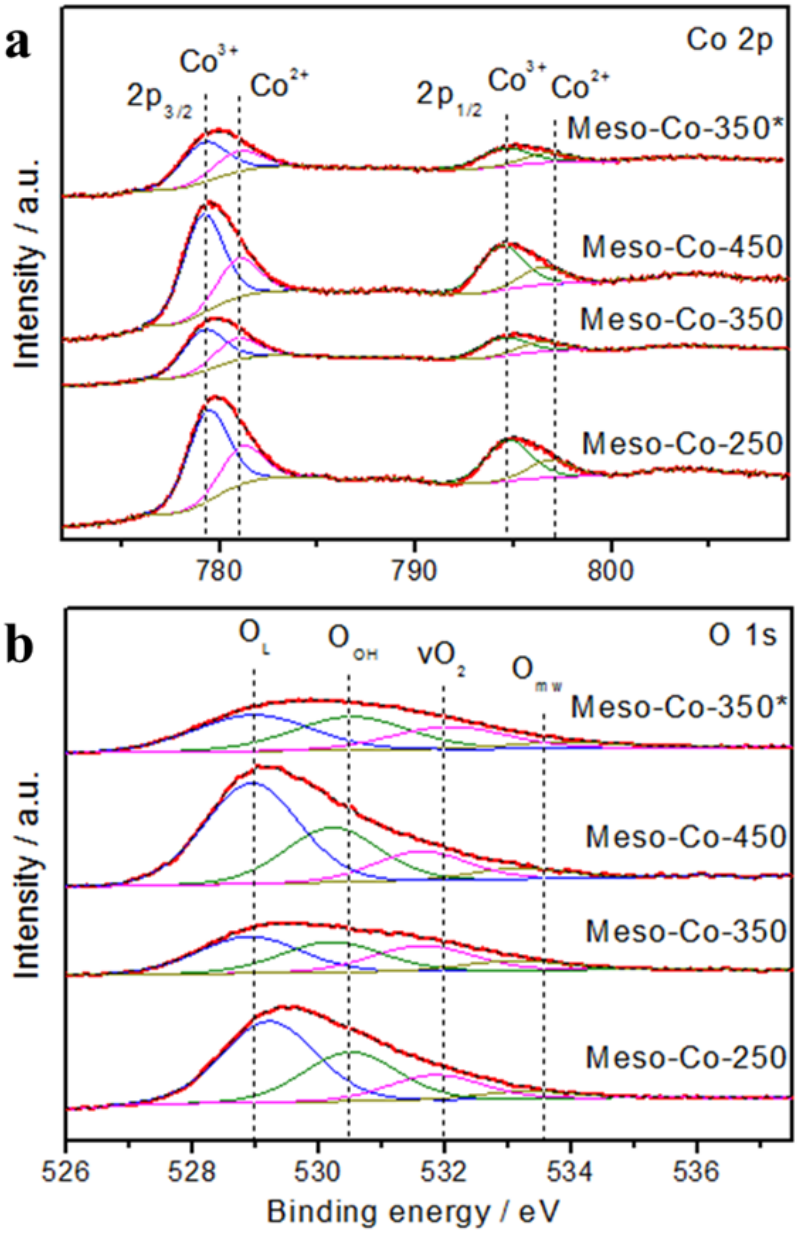

Figure 2.6 X-ray Photoelectron Spectroscopy (XPS) analysis. (a) Co 2p and (b) O 1s deconvoluted XPS spectra of mesoporous cobalt oxides (Meso-Co-X; X=250, 350, 450 and 350*).

Meso-Co-350* is the deactivated Meso-Co-350 sample after long-term stability tests under normal conditions for 15 hours.

2.3.4 Redox Properties

Catalysts exhibiting higher activity towards oxidation reaction generally have higher reducibility[59, 60]. H_2-TPR measurements were performed to investigate the difference in redox properties of Meso-Co-X (X=250, 350 and 450) and C-Co_3O_4 (Figure 2.7). This is controversial in the literature with respect to the TPR spectrum of Co_3O_4. For example, Arnoldy and Moulijin[61] reported one broad peak for the reduction of Co_3O_4. However more commonly, the reduction steps for Co_3O_4 was believed to be a step-wise process via $Co_3O_4 \rightarrow CoO \rightarrow Co^0$ [62-65]. Luo et al.[53] and Spadaro et al.[66] found that the reduction behavior of Co_3O_4 is highly dependent on the dispersion state of cobalt. Large particles of Co_3O_4 were usually reduced to metallic cobalt in a single step while nanoparticles often went through a two-step process. The reduction steps for Co_3O_4 samples presented here were consistent with literature findings. Mesoporous Co_3O_4 with nanoparticle sizes got reduced in a two-step fashion while C-Co_3O_4 was reduced directly to metallic Co due to its relatively large particle size, as discussed in section 3.1. The reduction profiles of mesoporous cobalt oxides started with a sharp peak in the range of 220 to 300ºC, which can be ascribed to the reduction from Co^{3+} to Co^{2+} ($Co_3O_4 \rightarrow CoO$). The subsequent broader reduction peak in the temperature range of 300 to 480ºC corresponded to the reduction of CoO to metallic Co. When the final heat treatment temperature was increased from 250 to 350ºC, both reduction peaks shifted to lower temperatures, indicating an enhanced reducibility of Meso-Co-350. Hydrogen spillover, structural change and promoted oxygen mobility are the major possibilities responsible for the enhanced reduction behaviors of base metal oxides[53]. Hydrogen spillover is usually achieved by promoted metal oxides, especially noble metals. The samples presented in this study are pure spinel cobalt oxides without any promoting ions. Therefore, the enhanced oxygen mobility seems to be the only possible reason for the increased reducibility of Meso-Co-350. Further increasing

the final temperature to 450ºC (Meso-Co-450) has led to a decrease of reducibility. PXRD and N_2 sorption measurements showed Meso-Co-450 had a larger particle size and smaller surface area as compared with Meso-Co-250 and Meso-Co-350. These factors can account for the decreased reducibility of Meso-Co-450. From H_2-TPR characterization, mesoporous cobalt oxides were found to demonstrate much higher reducibility than C-Co_3O_4. The order of catalyst reducibility correlates well with their catalytic activities (see section 3.4). Besides the two major peaks in the temperature range of 200 to 450ºC, there are small peaks below 200ºC. These peaks can be attributed to the reduction of surface oxygen species (O_2^- or O^-) adsorbed on oxygen vacancies[53, 65]. Meso-Co-350 had a small broad peak at 128ºC, as compared to Meso-Co-250 which had a smaller peak at around 185ºC. This indicated the heat treatment of UCT-8 from 250 to 350ºC helped generate more oxygen vacancies and increased the reactivity of surface adsorbed oxygen species. The presence of oxygen vacancies was also suggested by XPS (Figure 2.6) data. Meso-Co-350 had the most abundant surface lattice defects. These defects might enhance lattice oxygen mobility of Meso-Co-350 and further promote its reducibility.

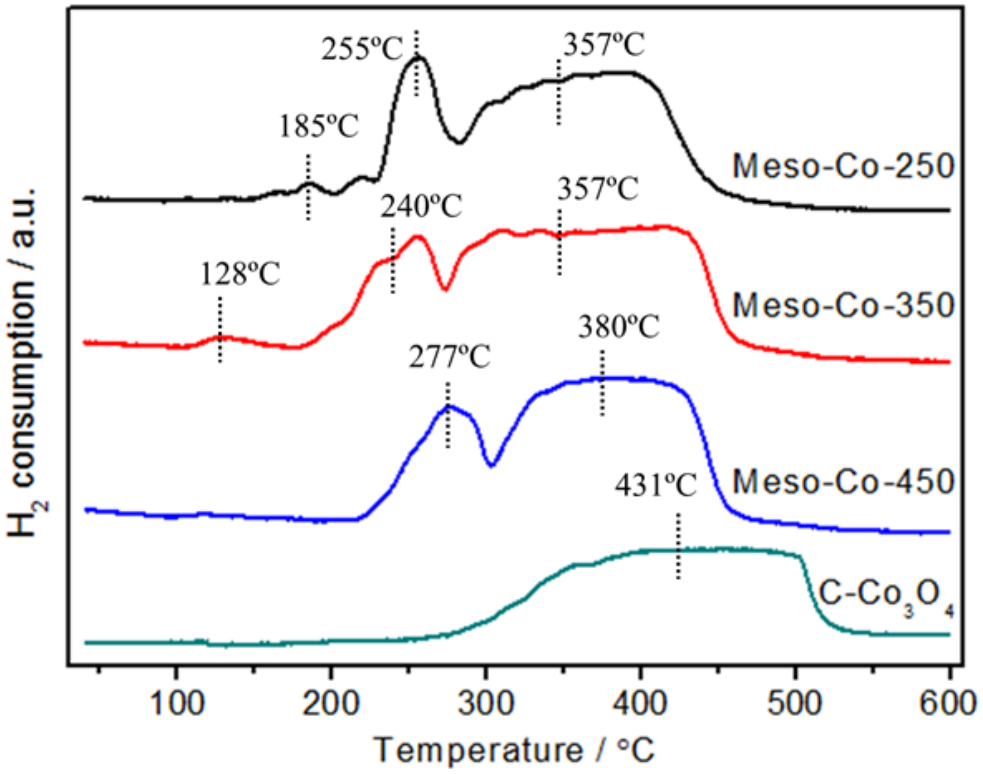

Figure 2.7 H_2-TPR profiles of mesoporous cobalt oxides (Meso-Co-X; X=250, 350 and 450) and commercial cobalt oxide (C-Co_3O_4). The measurements were conducted from room temperature to 600 ºC (10 ºC/min) under a stream of 10% H_2/N_2 with a flow rate of 50 sccm.

2.3.5 Reaction Mechanism

2.3.5.1 O_2-TPD

XPS and H_2-TPR analyses suggested that oxygen vacancies on catalyst surfaces may have a promotion effect on the redox properties and thus catalytic activity. To further investigate the surface defects and lattice oxygen mobility of the catalysts, temperature programmed desorption (TPD) analyses were performed. Figure 2.8a presents the O_2-TPD spectra of Meso-Co-X (X=250, 350 and 450) samples. Generally, the surface adsorbed oxygen species undergo the following transformation procedures with electron gain: $O_2(ad) \rightarrow O_2^-(ad) \rightarrow O^-(ad) \rightarrow O^{2-}(ad/lattice)$. $O_2(ad)$ refers to physically adsorbed oxygen, which usually can be removed by purging argon before the analysis. The oxygen adsorbed species of $O_2^-(ad)$ and $O^-(ad)$ are weakly bonded to catalyst surfaces and are easier to desorb. $O^{2-}(ad/lattice)$ is surface lattice oxygen and is difficult to be extracted. Based on results from the literature[67-69], the desorption peaks below 350ºC are usually attributed to surface adsorbed $O_2^-(ad)$ and $O^-(ad)$ species. These superficial oxygen species are associated with surface defects. The peaks located at temperatures higher than 350ºC come from the extraction of surface lattice oxygen and bulk lattice oxygen. Therefore, the oxygen desorption peaks with respect to temperature ranges can be classified as follows:

(1) 150-250ºC: desorption of surface adsorbed peroxy species $O_2^-(ad)$,

(2) 280-340ºC: desorption of surface adsorbed monatomic species $O^-(ad)$,

(3) 350-670ºC: desorption of surface lattice oxygen $O^{2-}(ad/lattice)$, and

(4) Beyond 700ºC: desorption of bulk lattice oxygen.

As shown in Figure 2.8a, all samples exhibited a large intense peak above 700ºC due to thermal decomposition of Co_3O_4. Among these catalysts, Meso-Co-250 exhibited a shoulder peak at 310ºC and Meso-Co-350 had a small broad peak centered at around 208°C, referring to the surface adsorbed monatomic species O^-(ad) and peroxy species O_2^-(ad), respectively. The results were consistent with H_2-TPR analysis in which Meso-Co-350 had more reactive surface adsorbed oxygen species than Meso-Co-250. Surface lattice oxygen desorbed in the temperature range of 350 to 670ºC. With increasing heat treatment temperature of the material from 250 to 450ºC, surface lattice oxygen desorbing temperature shifted to higher temperatures (390 $\rightarrow$ 557ºC) and the relative amount of oxygen evolved decreased significantly. Tang et al. prepared CeO_2/Co_3O_4 samples and found their surface areas decreased under high annealing temperatures. They claimed increasing the surface areas of the samples can weaken the Co-O bond and promote lattice oxygen desorption from Co_3O_4[54]. The larger surface areas can also enable more lattice oxygen exposed on the surface. Therefore the decreased surface lattice oxygen mobility of Meso-Co-X calcined from 250 to 450ºC can be attributed to a surface area effect. Correlating the findings from O_2-TPD with the catalytic performance, surface defect generation as well as high surface areas improved the catalytic activity of the catalysts for CO oxidation.

2.3.5.2 CO-TPD

In order to look into the surface oxygen activity of mesoporous cobalt oxides towards CO oxidation, CO-TPD measurements were also conducted. CO_2 desorption spectra in the absence of O_2 after CO adsorption are shown in Figure 2.8b. All the carbon monoxide adsorbed on the catalyst surface desorbed as carbon dioxide during the heating cycle with no CO signal detected. This indicates that lattice oxygen is involved in CO oxidation and the amount of desorbed CO_2 reveals the quantity of active surface lattice oxygen of the catalyst. CO_2 desorption amount follows the

same tendency as CO oxidation catalytic activity: Meso-Co-350 > Meso-Co-250 > Meso-Co-450. Similar as discussed previously, the higher surface area and more lattice defects result in higher lattice oxygen mobility. The presence of oxygen vacancies on Meso-Co-350 acts as a driving force for lattice oxygen migration[70]. This explains the highest activity of Meso-Co-350, even though its surface area is smaller than that of Meso-Co-250. The CO_2 desorption temperatures of various materials are more or less the same (~170ºC), which suggests similar CO_2 desorption rates from catalyst surfaces.

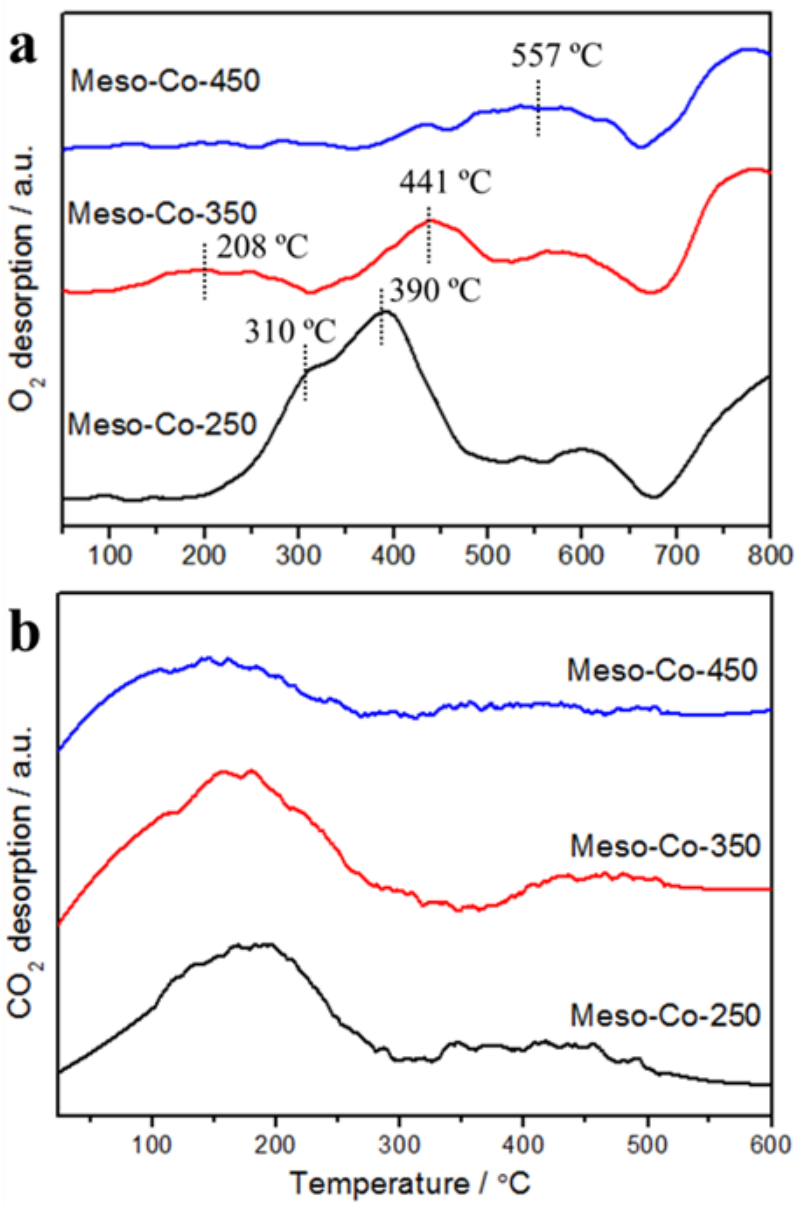

Figure 2.8 (a) O_2-TPD and (b) CO-TPD profiles of Meso-Co-X (X=250, 350 and 450) samples. The signals were recorded when the samples were heated under Ar (200 sccm) from room temperature to 800ºC with a heating rate of 10ºC/min.

2.3.6 Deactivation Mechanism

2.3.6.1 Fourier Transform Infrared Spectroscopy (FT-IR)

To understand the reason for deactivation, FT-IR tests were conducted on Meso-Co-350 to investigate the difference of the sample before and after deactivation. The spectrum of Meso-Co-350 before the reaction was obtained after the fresh sample was pretreated under He flow at 200ºC for one hour. After pretreatment, the reaction gas mixture was passed through the catalyst bed for 15 hours under normal conditions to ensure complete deactivation, then the IR spectrum was recorded. The sample was tested immediately after each treatment stage. Results are displayed in Figure 2.9a. Meso-Co-350 before and after deactivation both show two distinctive bands at 565 and 663 cm^{-1}, which originate from the characteristic stretching vibrations of Co_3O_4 metal-oxygen bond[71]. This indicates the Co_3O_4 spinel structure remained after long-term reaction. A broad band at around 3400 cm^{-1} corresponds to the stretching vibration of adsorbed molecular water[27]. As shown in Figure 2.9a, the deactivated sample exhibits a much more intense water band. Even if the reaction was conducted under normal conditions without sending additional water vapor, trace amounts of water (~ 3-10 ppm) present in the feed gas can accumulate on the catalyst. The detailed intensity change of IR bands in the range 1200–1800 cm^{-1} was enlarged and is shown in the inset graph. The band at 1628 cm^{-1} is due to the vibration of adsorbed molecular H_2O[27]. Additionally, the bands at 1336 and 1506 cm^{-1} can be assigned to the bending modes of carbonates, similar to the frequencies reported in the literature[48, 72, 73]. After deactivation, amount of molecular water was increased significantly and carbonates were formed on the catalyst, which might be responsible for the activity decay.

2.3.6.2 TPD after Deactivation

A TPD test was run on the used Meso-Co-350 after the stability test under normal conditions to identify gases adsorbed on the catalyst surface during the reaction and may explain the possible reasons for the deactivation. Meso-Co-350 was first purged under the reaction gas mixture for 15 hours, and then heated under argon flow. Desorbed gases were monitored continuously. The results are displayed in Figure 2.9b. Strong water signals as well as carbon dioxide peaks were detected. A carbon dioxide desorption peak at around 200ºC can be assigned to decomposition of carbonate species formed during the reaction[8, 74-76]. Another major CO_2 peak at around 460ºC may correspond to the interaction between surface carbon and lattice oxygen[74, 75, 77]. Surface carbon might be formed by CO disproportionation ($2CO \rightarrow C + CO_2$). In the meantime, a significant amount of water was generated during the reaction. Figure 2.9b shows a sharp peak of water at 150ºC indicating moisture accumulation during the reaction. Besides the water desorption peak at 150ºC, another broad peak in the 310-520ºC range corresponds to some strongly adsorbed water molecules on the surface[8]. The TPD results matches perfectly with FT-IR data. They both suggest that the formation of carbonates and increasing water amount might be possible deactivation paths for low temperature CO oxidation.

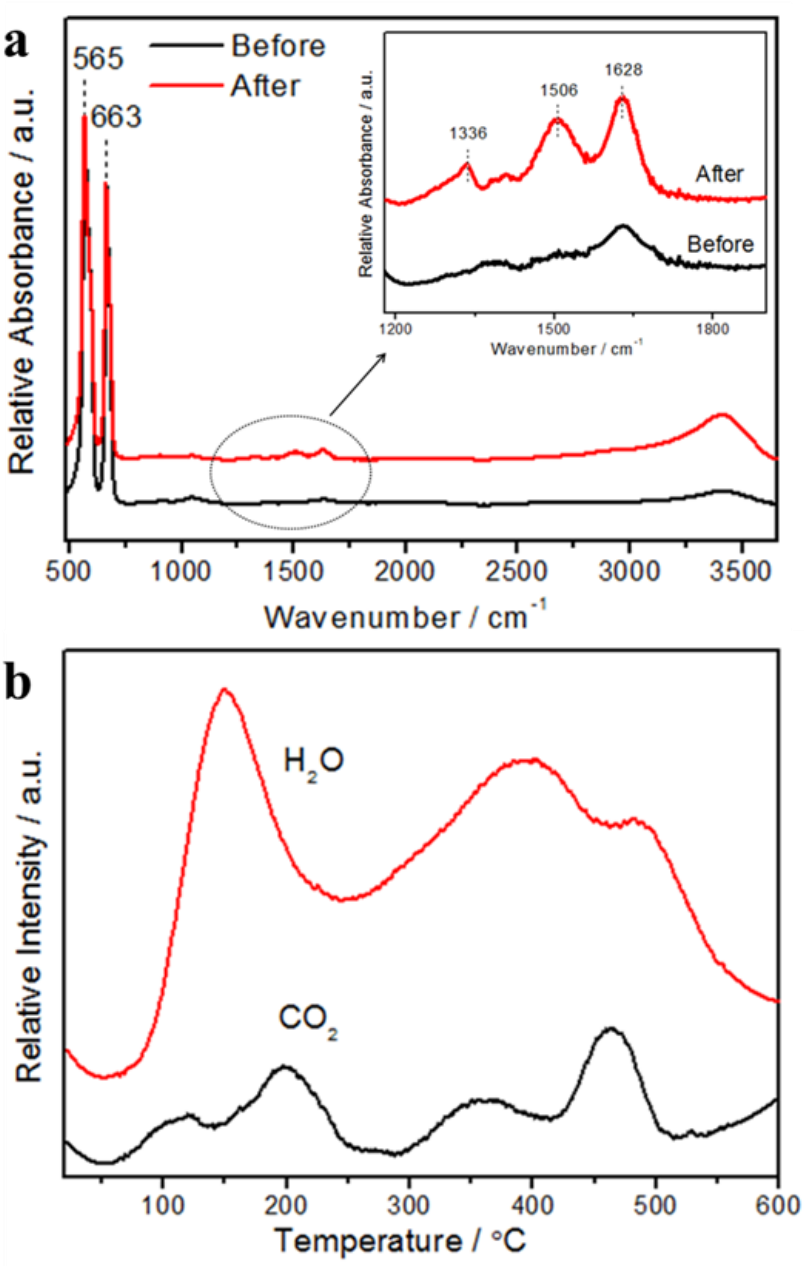

Figure 2.9 Characterizations of deactivated material. (a) FT-IR spectra of Meso-Co-350 before and after long-term stability tests under normal conditions for 15 h. (b) TPD profiles of Meso-Co-350 after complete deactivation under normal conditions. The desorption profiles were detected under Ar flow (200 sccm) with a heating rate of 10ºC/min.

2.4 Discussion

In this study, mesoporous cobalt oxides (UCT-8) were successfully synthesized by a recently developed approach[48]. This method involves the use of inverse surfactant (Pluronic P123) micelles. Sol-gel reactions of the metal oxo-clusters were controlled in acidic medium by unique NO_x chemistry. NO_x refers to a wide range of nitric oxides formed by thermal decomposition of the nitrate ion. The formed NO_x are adsorbed on the surface oxo-clusters to prevent uncontrolled condensation and their further decomposition increased the pH of the solution, which yielded oxidation of the oxo-clusters. Finally, the formed metal oxide mesostructure was a result of monodispersed nanoparticle aggregation and the mesopores were formed by connected intraparticle voids. Characterization studies of the as-prepared mesoporous cobalt oxides demonstrated the typical features of UCT materials. One low angle diffraction line and a Type IV adsorption isotherm, indicating a regular mesopore structure with a monomodal pore size distribution. Moreover, during heat treatment, unit cell expansion and pore size enlargement were observed. This unique properties of UCT materials can be readily seen by low angle PXRD (Figure 2.1b), TEM images (Figure 2.1c-e) and pore size distribution graphs (Figure 2.2b). As summarized in Table 2.1, the pore size increased from 3.8 to 7.7 nm and particle size grown up from 9.29 to 11.03 nm with increasing thermal treatment temperature from 250 to 350ºC. Such control of particle growth and pore size distribution by thermal treatment is unexpected for conventional mesoporous transition metal oxides[78]. A thermal treatment stage at 250ºC is required to completely transform the materials to the Co_3O_4 spinel phase.

The CO oxidation catalytic activity over metal oxide catalysts is believed to be closely associated with surface area, lattice defects, lattice oxygen mobility, crystallinity and the valence state of cations[70, 79-82]. Here we use several characterization techniques to examine the structural

properties of the materials and correlate with their catalytic behavior. Deconvoluted O 1s and Co 2p peaks from XPS analysis indicated that Meso-Co-350 have the most abundant oxygen vacancies as well as the highest Co^{2+}/Co^{3+} ratio (Figure 2.6). This is reasonable considering the overall surface charge neutrality. Co_3O_4 spinel structure contains both Co^{2+} and Co^{3+} cations. With higher surface concentration of Co^{2+}, oxygen deficiency is required to compensate for the positive charge loss on the surface and thus the formation of surface oxygen vacancies is favored. H_2-TPR measurements give the information about the reducibility of the catalysts. Figure 2.7 indicates Meso-Co-350 is the most reducible catalyst. Reduction peaks below 200ºC are assigned to the reduction of surface adsorbed oxygen on oxygen vacancies. Again, Meso-Co-350 exhibited the largest quantity of surface defects. According to the literature[67, 83], the more susceptible a metal oxide is to be reduced, the easier it is to generate oxygen vacancies. This agrees with our findings in which Meso-Co-350 not only shows the greatest reducibility but also generates the largest amount of oxygen vacancies. This has been further evidenced by O_2-TPD measurements (Figure 2.8a). Meso-Co-350 had a broad O_2 desorption peak at 208ºC, which was ascribed to desorption of surface adsorbed peroxy species O_2^-(ad). Correlating these findings with the catalytic activity tests, surface lattice defects enhance the activity of catalysts towards CO oxidation. Figure 2.8b shows CO-TPD spectra of different catalysts. All the carbon monoxide adsorbed on catalyst surfaces was desorbed as CO_2. Since lattice oxygen was the only oxygen source, the participation of lattice oxygen in the reaction was confirmed. Based on these findings, the reaction here is believed to proceed via the Mars-van Krevelen mechanism, in which the gas phase oxygen is exchanged with lattice oxygen[84-86]. Similar to the mechanisms reported in the literature[53, 74, 75, 87], the oxidation of carbon monoxide involves a redox cycle between Co^{2+} and Co^{3+}. Carbon monoxide is first adsorbed on the catalyst. The adsorbed CO extracts the neighboring lattice

oxygen and desorbs as CO_2, leaving the catalyst surface with an oxygen vacancy. The partially reduced site can be replenished by gas phase oxygen, and acts as active site for O_2 dissociation. Since O_2 dissociation is an endothermic process[87], it is not a dominant step in a low temperature reaction. The rate-determining step for CO oxidation is the reaction between CO and lattice oxygen, which generates an oxygen vacancy[70, 87, 88]. The presence of surface oxygen vacancies can promote the lattice oxygen diffusion from the bulk to the surface and facilitates the adsorption-desorption process of the gas phase species[89]. That leads to an enhanced catalytic performance. Typically, the generation of surface oxygen vacancies involves lattice distortion caused by incorporation of other metals[53, 63, 89, 90]. In the present study, lattice defects can simply be tuned by thermal treatment, which provides an alternative way to design redox active catalysts. Besides the promotion role of oxygen vacancies, surface area is another important factor in CO oxidation reactions. XPS results suggest that the amount of oxygen vacancies on Meso-Co-250 and Meso-Co-450 is on the same level, thus the activity difference can be mainly attributed to surface area differences. Increasing the calcination temperature from 250 to 450ºC significantly decreased the surface area from 181.4 to 57.9 m^2/g (see Table 2.1). As more oxygen is exposed on the surface, Meso-Co-250 exhibited much higher lattice oxygen mobility, as indicated in O_2-TPD and CO-TPD measurements. This accounts for the higher activity of Meso-Co-250 than Meso-Co-450. The presence of monatomic species O^-(ad) on Meso-Co-250 is also suggested by the small peak at 185ºC (H_2-TPR spectrum) and the shoulder peak at 310ºC (O_2-TPD spectrum). This kind of adsorbed oxygen species might also improve the catalytic activity.

Several possible deactivation mechanisms for CO oxidation reactions were proposed in the literature. In the previous studies, the adsorbed CO on the surface extracts the adjacent lattice oxygen while the generated oxygen vacancy can be reoxidized by gas phase oxygen or further

reduced by gas phase CO. If the reduction process proceeds faster than reoxidation, the catalyst surface will be irreversibly reduced causing deactivation[75]. However, this deactivation mechanism is not supported by the XPS measurements. In Figure 2.6, Meso-Co-350 after the stability test demonstrates almost the same surface composition as that of the fresh catalyst (0.51 Co^{2+}/Co^{3+} ratio versus 0.53 for fresh sample). In addition, this deactivation mechanism has not been reported for CO oxidation activity decay over Co_3O_4 at room temperature. Another possible mechanism of deactivation could be the surface reconstruction of the cobalt oxide, in which the coordination of the surface cobalt ions is changed without changing the oxidation state, making initially active cobalt ions unavailable for CO adsorption[76]. Given that the catalytic activity can be fully restored by heating the catalyst at 200ºC under helium flow (see section 3.2), surface reconstruction may not be responsible for the activity decay. Such kind of reconstruction should not be recovered under an inert atmosphere at a mild temperature. Furthermore, this deactivation mechanism cannot explain why deactivation occurs slowly at higher temperatures. In long term stability tests, Meso-Co-350 was deactivated after 11 hours on line reaction under normal conditions (~3-10 ppm H_2O). The conversion efficiency dropped quickly after the start of deactivation. However, when the reaction temperature was raised to 100ºC, the deactivation rate decreased dramatically. The catalyst still showed more than 50% conversion after 24 hours even under moisture saturated conditions (~3% H_2O). At 150ºC, no activity loss was observed throughout 24 hours of each run. More commonly, the deactivation was believed to occur when the active sites are blocked by carbonates, molecular adsorbed water or hydroxyl groups[51, 91]. This blocking effect is consistent with the experimental results. Figure 2.9b shows a TPD study for deactivated Meso-Co-350, H_2O and CO_2 desorption peaks at various temperature ranges were detected. Since the catalyst activity can be fully restored by heating under He at 200ºC, the desorption peaks beyond 300ºC due to

surface carbon and strongly adsorbed water cannot account for the activity decay. Water accumulation desorbed at 150ºC should be the main reason for deactivation. The small amounts of CO_2 desorbed at 200ºC suggest that carbonate species formation also contributes to the loss of activity. FT-IR data (Figure 2.9a) also indicate formation of carbonates and accumulation of moisture on the deactivated catalyst. Deconvoluted O 1s spectra (Figure 2.6b) show that the deactivated Meso-Co-350 contains less molecular adsorbed water than the fresh sample (6.5% compared to 9.5%). This is because the fresh sample was tested without any pretreatment. Pretreatment under inert gas can yield a clean catalyst surface, which should have much less moisture content than the deactivated sample, as evidenced by FT-IR measurement. To summarize, the accumulated moisture as well as carbonates can block the active sites on the catalyst surface and lead to the activity loss. At higher temperatures (> 100ºC) water poisoning is largely suppressed and the catalyst can maintain 100% conversion for 24 hours at 150ºC even under moisture rich conditions (~ 3% H_2O). Therefore, the deactivation of mesoporous cobalt oxide results from the blocking effects by water and carbonate species.

2.5 Conclusions

Mesoporous cobalt oxides (UCT-8) were successfully synthesized by a one step sol-gel process using a recently developed approach. The approach was based on an inverse surfactant micelle. Characterization of the materials demonstrated typical features of UCT materials. The presence of one low angle diffraction line and a Type IV sorption isotherm indicated a regular mesoporous structure with a uniform pore size distribution. Unit cell expansion and pore size enhancement with increasing heat treatment temperature from 150 to 450ºC was observed by PXRD, BET, FE-SEM and HR-TEM.

The catalytic performance of the catalysts followed the order: Meso-Co-350 > Meso-Co-250 > Meso-Co-450 > Meso-Co-150 > C-Co_3O_4. Meso-Co-350 exhibited the best catalytic behavior with T_{100} of -60ºC under normal conditions (~3-10 ppm H_2O) and T_{100} of 80ºC under moisture rich conditions (~3% H_2O). The activity order correlated well with the reducibility and lattice oxygen mobility of the catalysts as indicated by TPR and CO-TPD. XPS and O_2-TPD indicated Meso-Co-350 had the most abundant surface oxygen vacancies, which accounts for its promoted catalytic activity. Furthermore, high surface area also contributed to enhanced catalytic activity of Meso-Co-X compared with C-Co_3O_4. Accumulated water and carbonates are proposed to be responsible for the deactivation of the catalysts based on FT-IR and TPD results. The understanding of the effect of lattice defects and surface area on CO oxidation activity and the deactivation mechanism are crucial for continuous improvement of nonprecious metal oxide catalysts towards CO oxidation.

CHAPTER 3. MESOPOROUS METAL OXIDES ON CORDIERITE MONOLITHIC SUBSTRATE AS EFFICIENT LOW TEMPERATURE DIESEL OXIDATION CATALYSTS

3.1 Introduction

To coat a layer of active material on cordierite honeycomb substrate, several techniques have been used including dip coating, wash coating, spray coating and sol-gel coating. The most widely used technique in industry is dip coating. In a typical process, powder materials were dispersed in a proper solution. After homogeneous distribution, a binder was added to help stick the powder active material on the substrate. Several powder form materials have been reported to coat on the substrate by dip coating and used for exhaust after treatment applications.[13, 92, 93] However the dip coated samples usually suffer from lower catalytic activities. The addition of extra binder may block some active surface of the material and hinder the homogeneous distribution of the material throughout the substrate. Also this kind of coating process requires multi-step preparation. To increase the material utilization and eliminate the use of binder, catalysts with nanoarray configurations have been developed recently.[10, 11] Compared to powder based catalysts, nanoarray structured materials significantly decrease the material usage, largely expose active surfaces and improve gas solid interaction, resulting in better activities. One limitation of nanoarray material preparation is that the catalyst should have nanowire, nanorod or urchin like morphology. To extend the coating procedure to all kinds of materials with efficient catalytic properties maintained, a novel coating process is highly desirable.

The UCT synthesis method recently developed by our group might be a good candidate to realize this coating purpose. This approach uses Pluronic surfactant as the soft template. The

addition of this polymer in the precursor solution can increase the viscosity of the solution and make it sticky. Therefore, the polymer helps to stick the active materials on the cordierite substrate. Moreover, the UCT approach is ideal for synthesizing nanoparticle sized materials by the use of inverse micelles. The small particle sizes not only help the homogeneous distribution of the materials, but also let the material go into the macroporous structure of the substrate, leading to a strong adhesion force between the active layer and the substrate. In this chapter, in-situ coatings of mesoporous manganese oxide, cobalt oxide, and cerium oxide have been discussed. Those materials exhibited better CO oxidation activities than dip coated samples. To further promote the activity for mesoporous manganese oxide based monolithic catalysts, multiple coating process, nanoarray coatings and copper doping were introduced. The activity improvement was found to be related to increased loading amount and enhanced lattice oxygen mobility.

3.2 Experimental Section

3.2.1 Materials Synthesis

All chemicals were purchased from Sigma-Aldrich and used as received. Metal nitrates ($Co(NO_3)_2 \cdot 6H_2O$, $Mn(NO_3)_2 \cdot 4H_2O$, $Ce(NO_3)_3 \cdot 6H_2O$) were used as the metal sources. 0.02 mol of metal nitrates were dissolved in a solution containing 14 g 1-butanol, 2 g nitric acid and 2 g P123. After completely dissolving, the honeycomb substrate was put in the clear gel before further heating. The obtained substrate containing clear gel was heated in oven at 120 °C for 3-4 h, followed by rinsing with ethanol and drying in vacuum oven. Then the obtained powder together with the monolithic materials were subjected to a heating cycle of 150 °C 10h, 250 °C 3h and 350 °C 2h.

3.2.2 Material Characterizations

Powder X-ray diffraction (PXRD) analyses were conducted on a Rigaku Ultima IV diffractometer with Cu Kα radiation (λ = 1.5406 Å) at room temperature. The operating voltage was 40 kV and the current was 40 mA. Both low angle (2θ = 0.5° - 8°) and wide angle (2θ = 5° - 75°) diffraction patterns were measured. The morphologies of the samples were investigated with a Zeiss DSM 982 Gemini field emission scanning electron microscope (FE-SEM) with a Schottky emitter at an accelerating voltage of 2.0 kV and a beam current of 1.0 mA. Elemental mapping of the materials were carried out on an Oxford Aztec Energy microanalysis system equipped with an X-Max 80 silicon drift detector.

Temperature-programmed reduction analyses were conducted in a programmable tube furnace equipped with a gas analyzer MKS coupled with a quadruple mass selective detector. Monolithic materials were packed in a quartz tube reactor mounted into the tube furnace. The loaded samples were pretreated in an inert gas flow (Ar) at 200ºC for 1 h to clean the catalyst surface before each test. 5% H_2/Ar flow was passed through the catalyst bed at a flow rate of 200 sccm, while the temperature was ramped from room temperature (RT) to 600ºC. H_2 consumption signal was recorded.

3.2.3 CO Oxidation Tests

CO oxidation was carried out in a continuous flow fixed bed quartz tubular reactor under atmospheric pressure. For catalytic test, four pieces of 2mm × 2mm × 1cm monolithic catalyst were aligned in a row in a glass tube. Before the measurement, the catalysts were pretreated under helium flow (20 sccm) for 1 h at 200ºC to clean the catalyst surface. After cooling down, a gas mixture of 1% CO, 10% O_2 balanced in N_2 was passed through the catalyst bed with a flow rate of 20 sccm. The outlet gas streams were analyzed by an online gas chromatograph (SRI 8610C Multiple Gas Analyzer #1 GC) equipped with a thermal conductivity detector (TCD), a 6 foot long

molecular sieve 13X packed column, and a 6 foot long silica gel packed column. GC samples were injected after 10 min stabilization at any given temperature. The reaction conversion was calculated based on the CO concentration, N_2 was used as an internal standard.

3.3 Results

3.3.1 In-Situ Synthesis of Mesoporous Metal Oxides Coated Cordierite Substrate.

3.3.1.1 Mesoporous Manganese Oxides

Figure 3.1c shows the picture of as-prepared mesoporous manganese oxide monolith catalyst. The bare cordierite honeycomb substrate has a white color, after the coating procedure it turned black. We could easily tell there is a decent coating on the substrate simply by the color of the sample. To confirm the successful synthesis of mesoporous manganese oxide, the remaining powder was collected and subjected to PXRD tests. Both high angle and low angle PXRD were measured. The results are shown in Figure 2.1a, b. Mesoporous manganese oxide calcined at 350°C exhibited amorphous nature, which is consistent with recently published work from our group.[94, 95] The material will start to crystallize at 450°C. Low angle PXRD pattern displayed one diffraction line, confirming the existence of an ordered mesostructure. This is typical for UCT materials. Besides the photo of the synthesized material, the coating layer of manganese oxide was also evidenced by SEM images, as shown in Figure 3.1d, e. The presence of the small round particles on the substrate can be clearly observed. The material not only adhere on the surface of the substrate, but also penetrate into the macroporous structure of the cordierite. The zoomed in image shown in Figure 3.1e allowed us to calculate the thickness of the coating layer to be around 0.5 micron. Moreover, by weighing the substrate before and after coating, the active material loading ratio was calculated to be ~8%. Furthermore, to increase the loading amount, the as-

prepared sample was subjected to a second and third coating procedure. After the second coating, the loading ratio was increased to ~17.4%, doubled the loading amount of one layer coating. The third layer coating did not give that much increase in terms of loading amount. The loading ratio finally reached ~22.7%, only ~5% higher than the two layer coating, suggesting the material started to reach the maximum loading amount on the cordierite substrate.

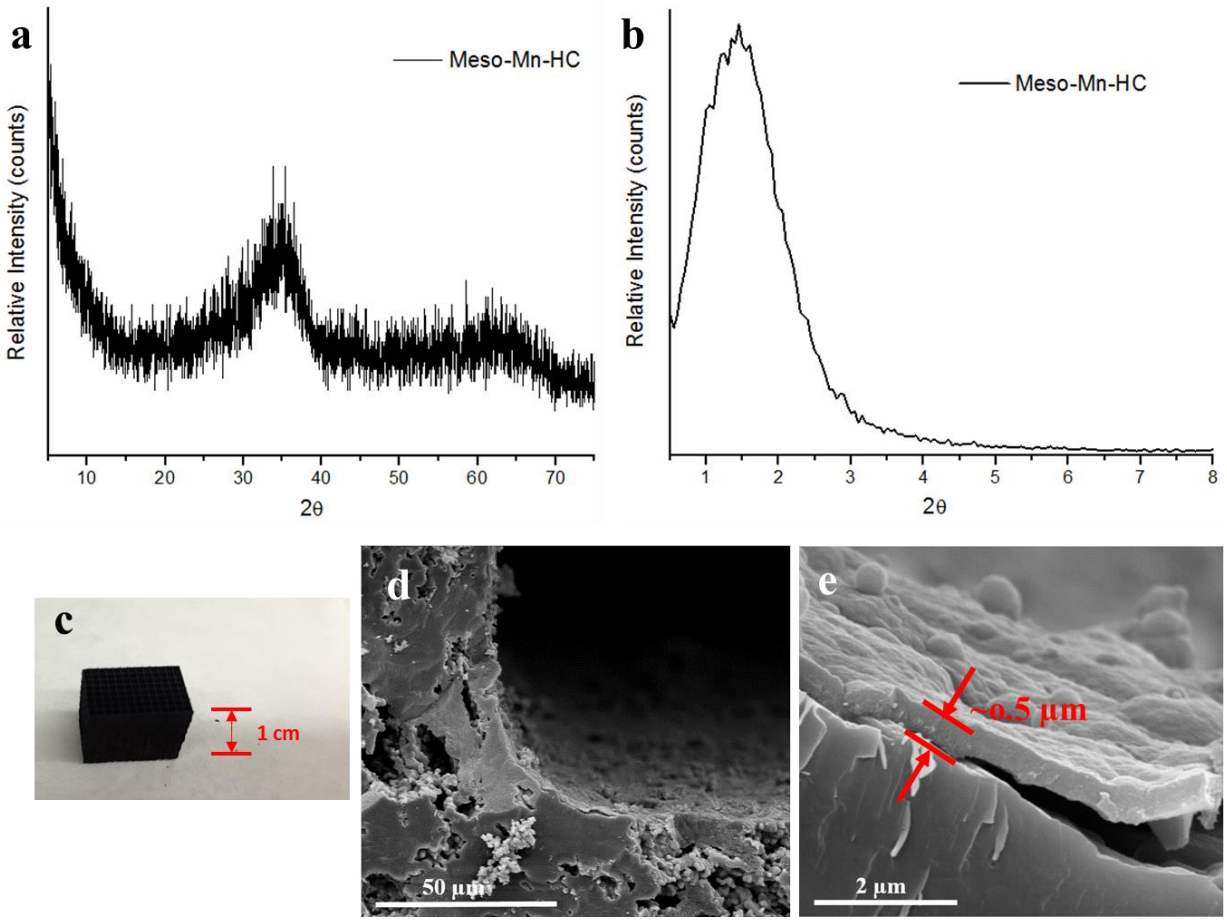

Figure 3.1 (a) Wide angle and (b) Low angle PXRD patterns of mesoporous manganese oxide. (c) Picture of as-prepared mesoporous manganese oxide monolith catalyst. (d) and (e) SEM images of mesoporous manganese oxide on cordierite.

Compared to powder based monolith catalysts, nanoarray catalysts have several advantages including better exposed active sites, high surface area and short diffusion length. The open-access feature of nanoarray materials can enable more efficient gas-solid interaction and largely increase the material utilization. Therefore, nanoarrays have been widely used in the application of exhaust after treatment as highly active materials and as ideal supports for precious metal loading. Herein, we coated our mesoporous manganese oxide catalyst onto the α-MnO_2 nanoarray structure. PXRD and SEM results were given in Figure 3.2. Wide angle PXRD patterns still indicate the amorphous nature of the material. However compared to PXRD results of Meso-Mn-HC (Figure 3.1a), Meso-Mn-AR showed more weak diffraction lines. Two additional diffraction lines between 30 and 40 degree might be ascribed to the α-MnO_2 structure, which fell off the substrate during the synthesis. The mesoporous structure was confirmed by the diffraction line in low angle PXRD region (Figure 3.2b), similar to other UCT materials. Figure 3c and d displayed the SEM images of α-MnO_2 nanoarrays before and after manganese oxide coating. Before coating, the nanoarray has a short nanowire morphology aligned on the substrate. After coating, the presence of nanoparticles randomly distributed on the nanoarray can be observed in Figure 3d. However this failed to show a uniform coating layer throughout the material. The sample loading ratio was calculated to be around 17%.

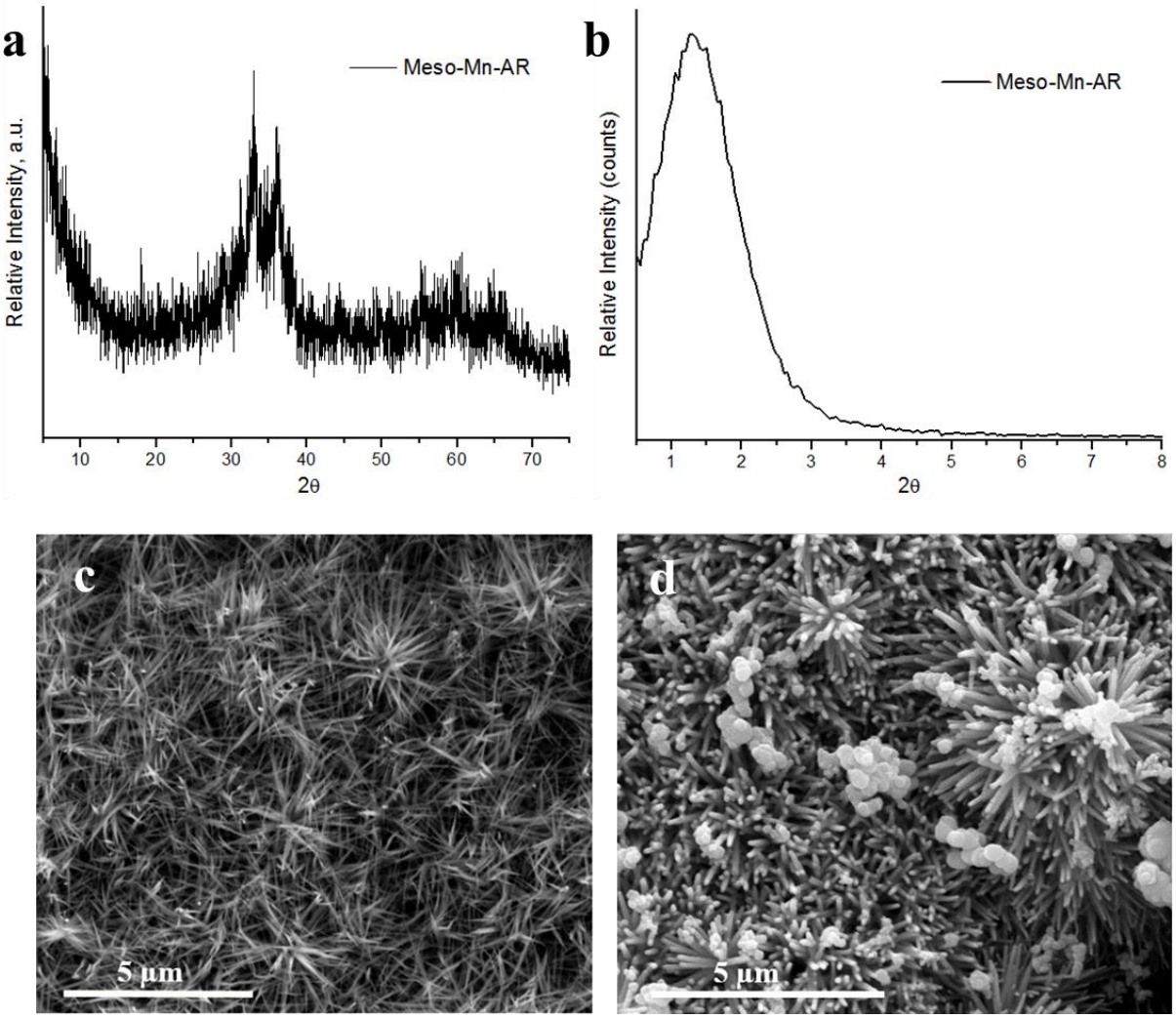

Figure 3.2 (a) Wide angle and (b) Low angle PXRD patterns of Meso-Mn-AR. SEM images of α-MnO_2 nanoarray structure (c) before and (d) after mesoporous manganese oxide coating.

3.3.1.2 Ion-Promoted Mesoporous Manganese Oxides

To extend this coating procedure to other materials in UCT family, we first tried to coat Cs-promoted mesoporous manganese oxide, which is also called UCT-18-Cs. Similarly, the cordierite substrate was immersed in the precursor solution at the beginning step, and the obtained material was heated to 350°C. The sample was characterized by PXRD and SEM, and results are presented in Figure 3.3. The wide angle PXRD pattern displayed in Figure 3.3a still shows an amorphous nature, which is typical for all UCT manganese oxide based materials. The form of the mesostructure was indicated by the diffraction line in the low angle PXRD region (Figure 3.3b). Figure 3.3c is the picture of the material after the coating process. No white color from the bare substrate can be observed, suggesting UCT-18-Cs was homogeneously coated on the cordierite. SEM images presented in Figure 3.3d, e showed the cross section images of the material. A thin uniform layer of material was present on the substrate. Similar to Meso-Mn-HC, the material not only formed on the surface of the cordierite, but also went into the porous structure of the substrate. The active material loading ratio is roughly 7.3%, slightly lower than the loading ratio of Meso-Mn-HC (~8%).

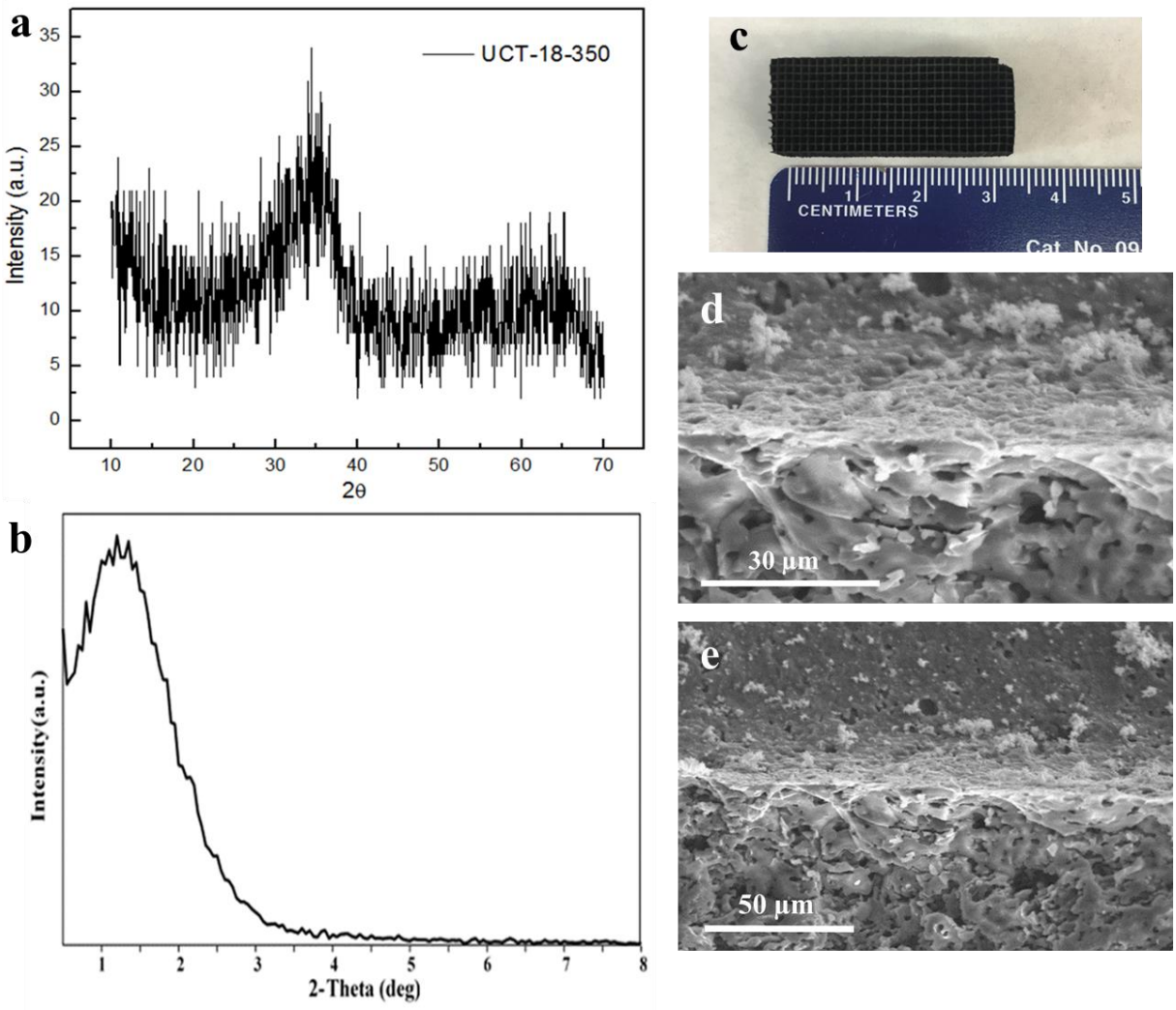

Figure 3.3 (a) Wide angle and (b) Low angle PXRD patterns of Cs-promoted mesoporous manganese oxide material. (c) Photo of UCT-18-Cs coated on cordierite monolith substrate. (d) and (e) SEM images of UCT-18-Cs on cordierite substrate.

On the other hand, copper manganese oxide, also known as hopcalite, is a commercial catalyst used in air purification devices for respiratory protection. This material is inexpensive compared to precious metals. Copper manganese oxide has been reported to have better activity for carbon monoxide oxidation and volatile organic compounds oxidation.[51, 96] Therefore, here we try to dope copper into mesoporous manganese oxide in the hope of improving its CO oxidation activity. Three copper nominal concentrations were used: 10%, 20%, and Cu:Mn 1:2 ratio (33.3%Cu). Figure 3.4a displays wide angle PXRD patterns of 10%Cu-Mn and Cu:Mn 1:2 materials. Both samples show two additional diffraction lines at 36 and 39 degrees, which corresponded to the CuO crystal phase. With more Cu in the material, those two diffraction lines become sharper, and several additional diffraction lines in the region of 50-70 degree start to evolve. Those diffraction lines all belong to the CuO phase. No manganese oxide related diffraction lines were observed due to its amorphous nature. The wide angle PXRD results suggested that phase segregation occurred during the synthesis. EDX mapping under SEM as illustrated in Figure 3.4c showed a homogeneous distribution of Cu, Mn, and O atoms throughout the material. Therefore, we can conclude from PXRD and EDX results that the prepared sample consists of CuO nanoparticles homogeneously distributed over the amorphous mesoporous manganese oxide surface. SEM images given in Figure 3.4b showed that the morphology of the sample is randomly packed small round nanoparticles. The smaller nanoparticles with diameters less than 100 nm are CuO. The mesopores can also be clearly seen from the image. The active material loading ratios of 10%Cu-Mn-HC, 20%Cu-Mn-HC, and Cu/Mn 1:2-HC are ~5.5%, ~7.3%, and ~2.3%, respectively.

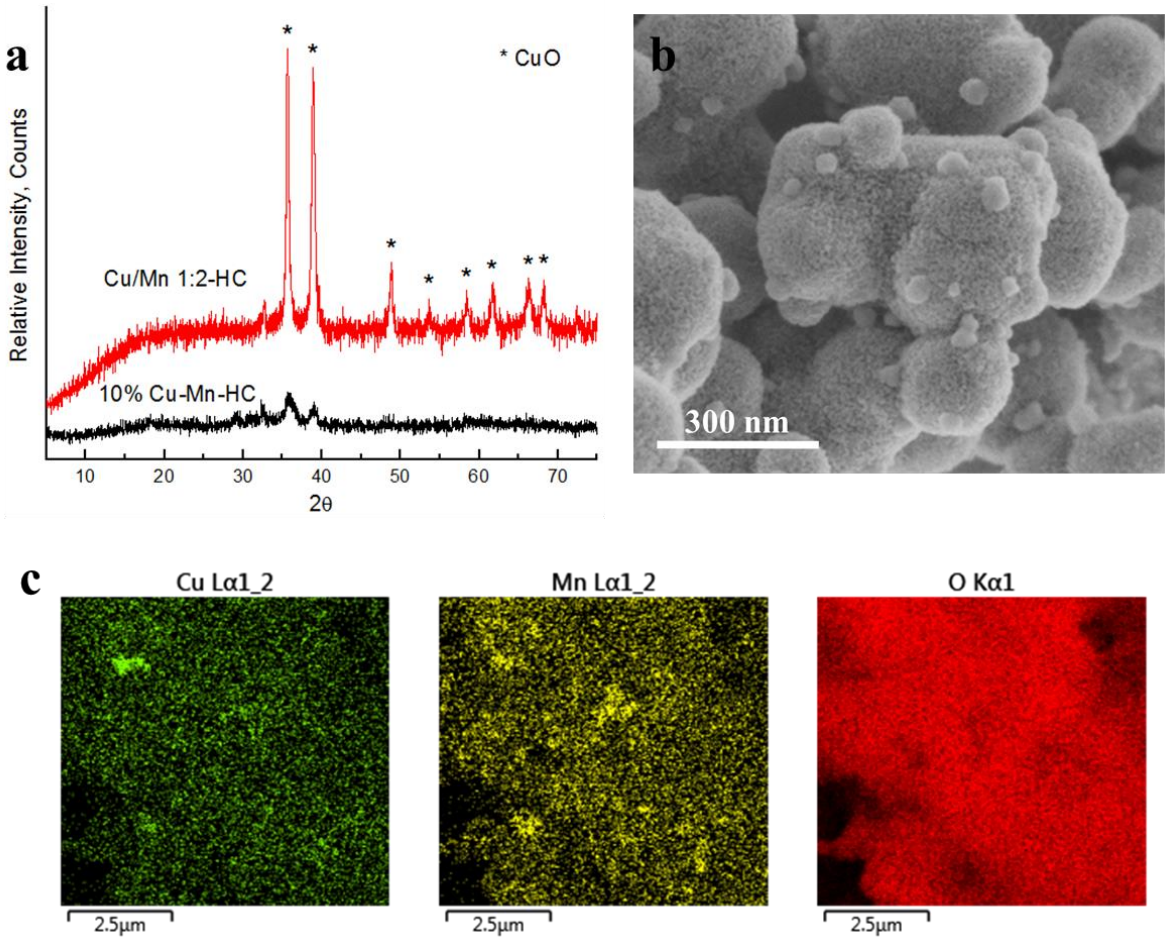

Figure 3.4 (a) Wide angle PXRD patterns of 10%Cu-Mn-HC and Cu/Mn 1:2-HC. (b) SEM image and (c) EDX mapping of Cu/Mn 1:2-HC.

3.3.1.3 Mesoporous Cobalt Oxide

Besides manganese oxide based materials, there are more than 50 materials in the UCT family. Among those materials, cobalt oxide would be a good candidate for exhaust after treatment applications. Similar to manganese oxide, cobalt oxide has multivalent nature which is a suitable catalyst for redox reactions. Over the past decade, cobalt oxide has become the most intensively studied material for carbon monoxide oxidation and hydrocarbon combustion. Co_3O_4 nanorods can completely convert CO to CO_2 at a temperature as low as -77°C.[8] In this thesis, mesoporous cobalt oxide synthesized by UCT approach was coated on cordierite substrate. Figure 3.5a presents wide angle PXRD patterns of 20%Mn-Co-HC and Meso-Co-HC. They almost exhibited the same PXRD patterns, no manganese oxide related phases were observed. Furthermore, the diffraction lines of 20%Mn-Co-HC shifted to the left compared to Meso-Co-HC, as indicated by the drop line in Figure 3.5a, again confirming no phase segregation occurred. The added Mn was successfully incorporated into the Co_3O_4 lattice and formed a Mn-Co-O solid solution. Figure 3.5b showed that 20%Mn-Co-HC diffracted in the low angle PXRD region, indicating the mesostructure was maintained, even though lattice distortion was caused by the foreign cation Mn. So far, mesoporous 20% Mn doped cobalt oxide was successfully synthesized. Figure 3.5c is a photo of 20%Mn-Co on a cordierite substrate. The black color of the monolith catalyst suggests a uniform layer of active material on the substrate. The presence of the material on cordierite was further evidenced by the SEM image in Figure 3.5d. A layer of mesoporous material can be clearly seen from the image. There is a cracking in the layer, which is likely due to the calcination step at 350°C. However there is no obvious weight increase after the coating process, probably due to etching of the substrate by nitric acid in the precursor solution. As a result, no loading ratio was calculated.

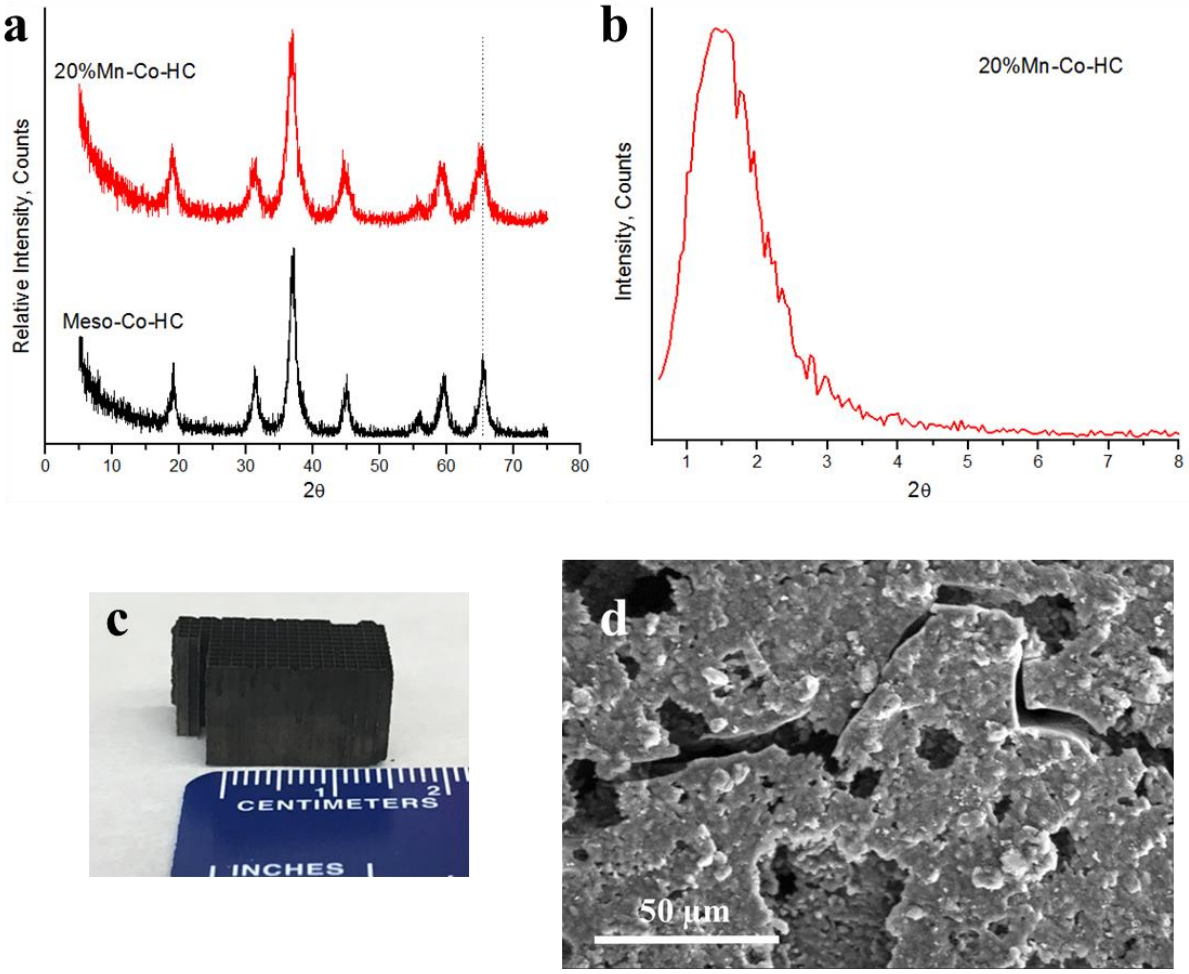

Figure 3.5 (a) Wide angle and (b) Low angle PXRD patterns of 20%Mn-Co-HC and Meso-Co-HC. (c) Photo and (d) SEM image of 20%Mn-Co on cordierite substrate.

3.3.1.4 Mesoporous Cerium Oxide

Lastly, we have extended this method to cerium oxide. Ceria has two stable forms of oxidation states: Ce^{3+} and Ce^{4+}. The redox potential between Ce^{3+} and Ce^{4+} is relatively low (1.7 V), which makes ceria have excellent redox properties. Additionally, cerium oxide is well known for its high oxygen storage capacity. As a result, ceria can easily release oxygen under a reducing atmosphere and replenish oxygen by interaction with oxidizing gases.[97] Cerium oxide is expected to have very promising catalytic activity for emission control applications. Figure 3.6a presents the wide angle PXRD data for mesoporous cerium oxide synthesized by the UCT approach. All the diffraction lines can be correlated to the CeO_2 crystal phase, indicating the material has good crystallinity, as expected. Similarly, photos were taken for mesoporous cerium oxide coated cordierite substrates. As shown in Figure 3.6b, cerium oxide and cordierite have very similar color, we could not tell from the picture whether we have a decent coating on the substrate or not. However, by measuring the weight of the sample before and after coating, we were able to calculate the coating ratio of cerium oxide to be ~5%. The existence of the layer on the substrate was further confirmed by SEM images as displayed in Figure 3.6c, d. A single layer of cerium oxide nanoparticles was uniformly bound on the surface of the substrate. The active material has a spherical morphology. The UCT synthesis method can be used to in-situ coat mesoporous manganese oxide, cobalt oxide and cerium oxide on the cordierite substrate. The loading ratios of different materials are summarized in Table 3.1.

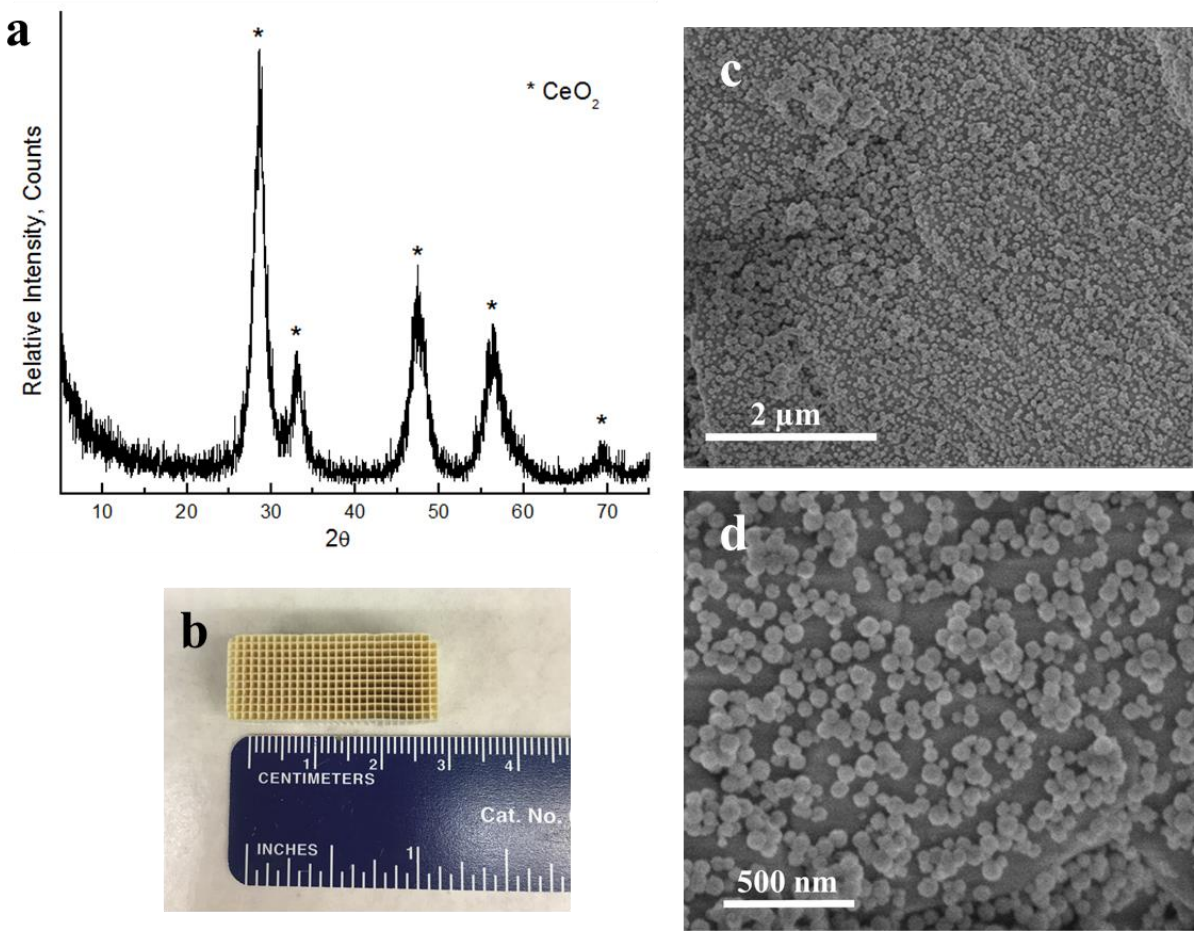

Figure 3.6 (a) Wide angle PXRD pattern for mesoporous cerium oxide. (b) Photo, (c) and (d) SEM images of mesoporous cerium oxide on cordierite substrate.

Table 3.1 Structural parameters and catalytic activities of different materials mentioned in this chapter.

Material	Loading ratio	Mass of active material	T_{50}
Meso-Mn-HC-1st	~8%	~9 mg	126°C
Meso-Mn-HC-2nd	~17.4%	~21 mg	100°C
Meso-Mn-HC-3rd	~22.7%	~29 mg	103°C
Meso-Mn-AR	~17%	~18 mg	110°C
10%Cu-Mn-HC	~5.5%	~6.1 mg	108°C
20%Cu-Mn-HC	~7.3%	~8.0 mg	108°C
Cu/Mn 1:2-HC	~2.3%	~2.5 mg	124°C
Cs-Mn-HC	~7.3%	~5.9 mg	156°C
Meso-Ce-HC	~5%	~5 mg	190°C
20%Mn-Co-HC	--	--	87°C
Meso-Mn-DC	~10.7%	~16 mg	146°C
Meso-Co-DC	~12.0%	~21 mg	83°C

-- Signifies not applicable

3.3.2 Dip Coated Mesoporous Metal Oxides on Cordierite Substrate

Instead of the novel in-situ coating method discussed in 3.3.1, in industry, wash coating or dip coating procedure is usually used. In a typical dip coating process, the prepared powder form material is dispersed in a proper solvent. To this dispersion solution, a binder such as colloidal silica, PTFE, PVP or PVDF is added to increase the viscosity of the solution. Thus the active material can stick onto the substrate. However, the addition of polymer binder may block some active sites on the material and lead to lower catalytic activity. To minimize the blocking effect of the binder, herein, Al_2O_3 was used instead of polymer binder. The high porosity and large surface area of Al_2O_3 make this material an ideal candidate for the coating process. Also alumina has been widely used as a secondary support for noble metals to help maximize the utilization of the expensive active component. More importantly, Al_2O_3 is sticky in acidic medium, thus no extra binder is needed.[92] Figure 3.7 shows the SEM images and photos of mesoporous manganese oxide and mesoporous cobalt oxide dip coated monolith catalysts. From the pictures (Figure 3.7c, d) of the coated samples, a grey thick layer coating of the mesoporous material was deposited on the surface of the substrate. SEM images shown in Figure 3.7a and b again indicate the existence of layers of nanoparticles on cordierite, no morphology due to bare substrate was observed. With the addition of Al_2O_3, the mesoporous materials were well dispersed and particle aggregation was controlled. The particle size of the active material is on the nanometer scale. Moreover, the loading amount of the catalyst can be built up by a repeated dip coating process until a desired amount is obtained. In this study, to compare the CO oxidation performance of dip coated samples with that of in-situ synthesized catalysts, the loading ratios of Meso-Mn-DC and Meso-Co-DC were finally adjusted to be ~10.7% and ~12.0%, respectively.

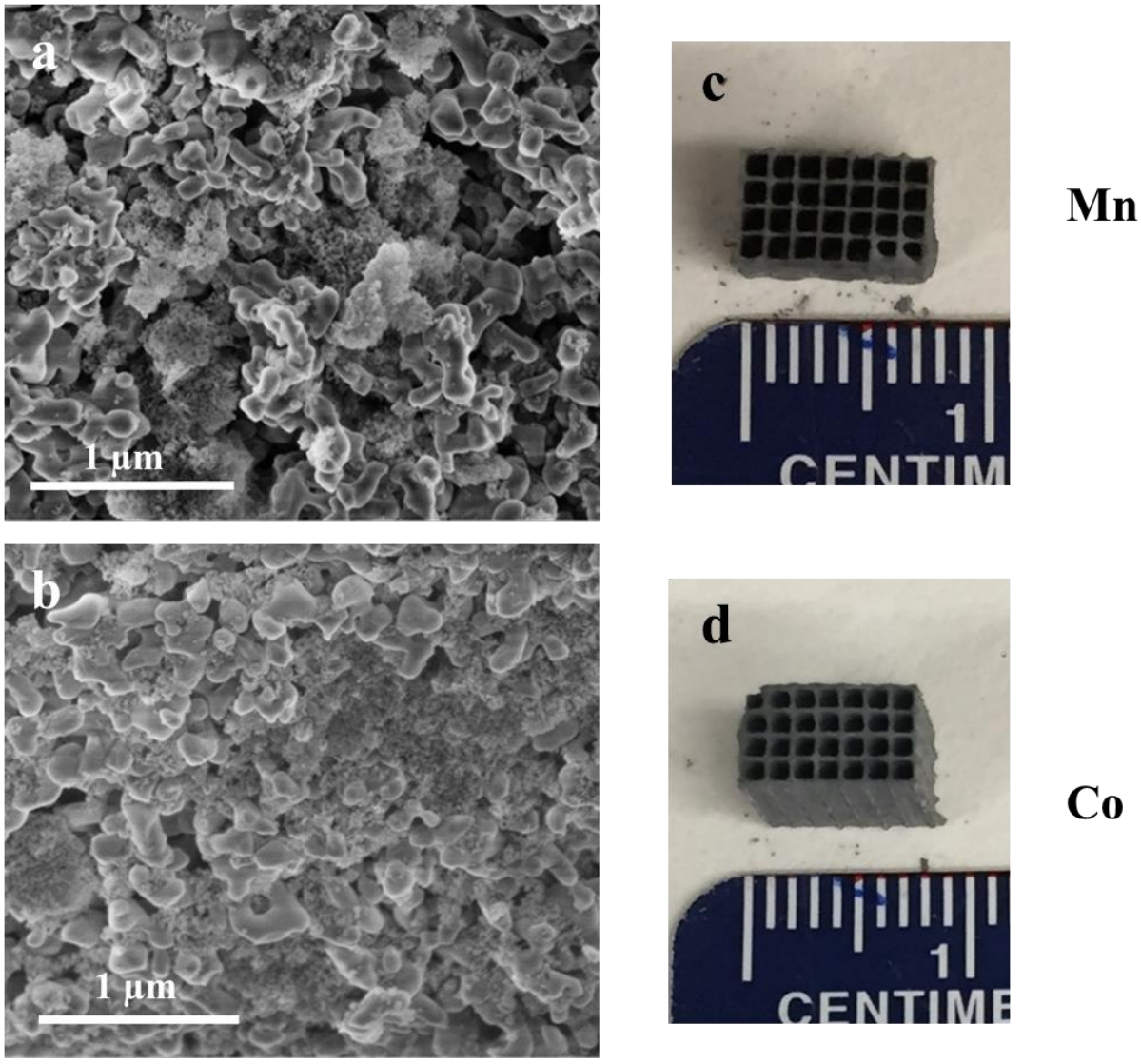

Figure 3.7 (a) SEM image and (b) Picture of Meso-Mn-DC. (c) SEM image and (d) Photo of Meso-Co-DC.

3.3.3 CO Oxidation Reaction Activity

Carbon monoxide oxidation was chosen as the model reaction to evaluate the catalytic activities of the prepared materials. Figure 3.8a gives CO light off plots of in-situ prepared Meso-Mn-HC, 20%Mn-Co-HC, Cs-Mn-HC, Meso-Ce-HC, and dip coated Meso-Mn-DC and Meso-Co-DC. Overall, cobalt oxide based materials exhibited the lowest light off temperature, cerium oxide based material showed the lowest activity, with manganese oxide materials in between. This result is in line with previous reports.[8, 51, 98] Among cobalt oxide materials, Meso-Co-DC showed the best activity with T_{50} at 83°C, slightly lower than 87°C for 20%Mn-Co-HC. This could be explained from two aspects. First, Meso-Co-DC has a relative large amount of active material in catalytic testing (~21 mg). Secondly, with 20%Mn doped into the sample, the activity may decrease compared to pure cobalt oxide catalyst. For manganese oxide based monolith catalysts, Meso-Mn-HC exhibited the best activity, which can completely oxidize CO to CO_2 at 175°C. Meso-Mn-DC and Cs-Mn-HC has lower activities with total oxidation achieved at 200°C. Lastly, Meso-Ce-HC showed the lowest activity, which completely converted CO to CO_2 at 250°C.

The synthesis approach of Meso-Mn-HC was further modified, and the prepared materials were tested for CO oxidation reaction as well. Figure 3.8b compares the activities for Meso-Mn-HC with different loading cycles. Meso-Mn-HC with only one layer of material on cordierite gives the lowest activity as expected. After a second coating was deposited on the substrate, the light off temperature was reduced from 126°C to 100°C. However, the activity stayed the same when a third layer of manganese oxide was grown on the substrate. This indicates Meso-Mn-HC reaches the maximum CO oxidation activity.

Figure 3.8c displays the CO light off curves of Meso-Mn-HC and Meso-Mn-AR. By coating mesoporous manganese oxide on nanoarray instead of bare substrate, the light off

temperature was decreased from 126°C to 110°C. Bare nanoarray without Meso-Mn coating does not have any activity until 300°C, so the activity of Meso-Mn-AR shown in Figure 3.8c is solely due to the Meso-Mn coating on the array. As summarized in Table 3.1, the exact catalyst amount used in catalytic test for Meso-Mn-AR is around 18 mg, higher than 9 mg for Meso-Mn-HC. Therefore, we cannot conclude whether the activity enhancement is due to the nanoarray configuration or loading amount increase, which needs to be further investigated.

Figure 3.8d presents the CO oxidation activities for Cu-incorporated mesoporous manganese oxides. 10%Cu-Mn-HC and 20%Cu-Mn-HC showed almost the same CO oxidation activity, with T_{50} at 108°C, both higher than T_{50} for Meso-Mn-HC (126°C). However, when Cu to Mn ratio is increased to 1:2, the activity decreased with light off temperature at 124°C, almost the same as Meso-Mn-HC. Similar to the case for Meso-Mn-AR, all these materials have different loading amounts on cordierite. In order to study the intrinsic reason for the activity improvement, CO oxidation activities need to be normalized to actual catalyst weight. This will be discussed later.

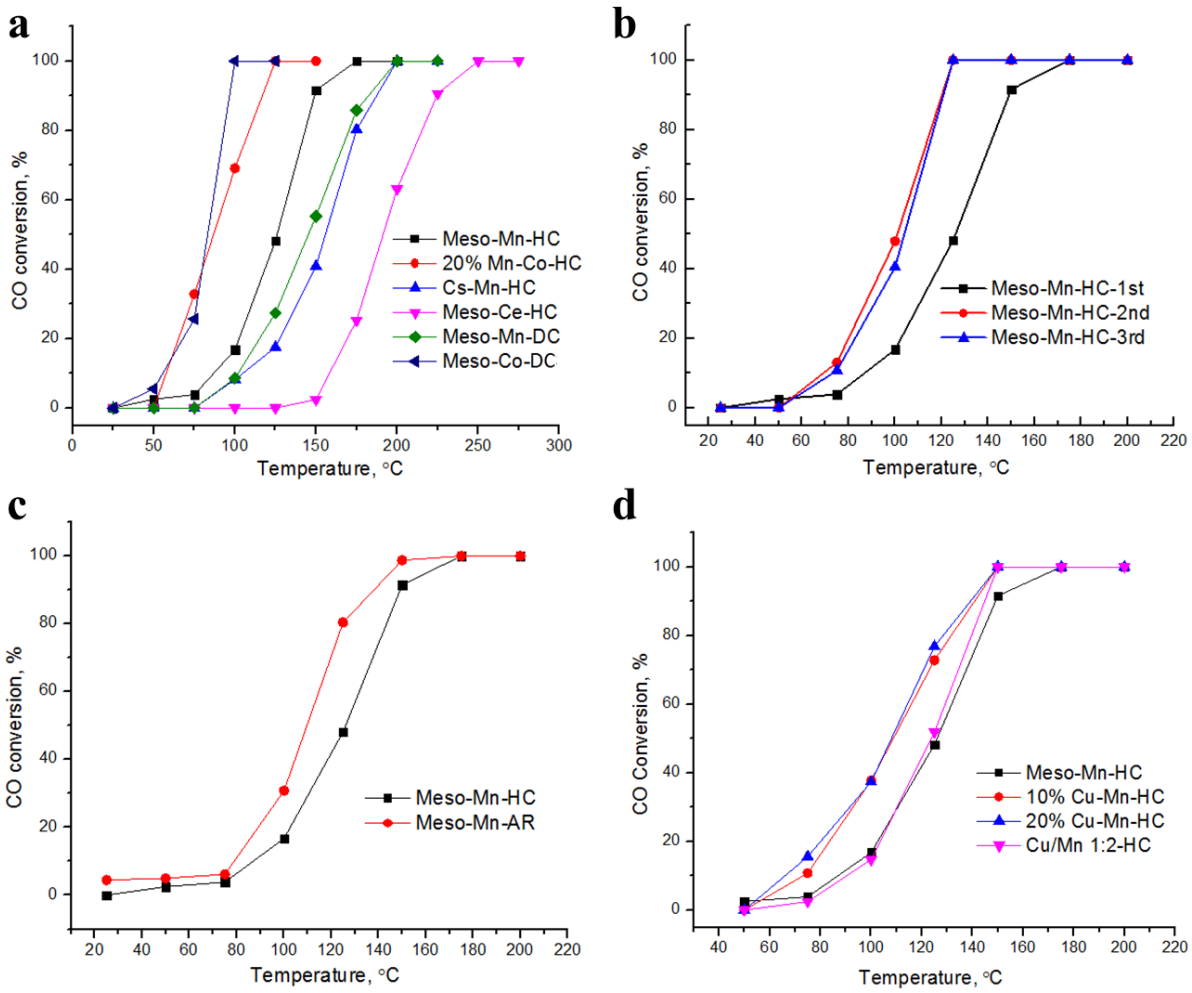

Figure 3.8 CO oxidation activities for: (a) Meso-Mn-HC, 20%Mn-Co-HC, Cs-Mn-HC, Meso-Ce-HC, Meso-Mn-DC and Meso-Co-DC; (b) Meso-Mn-HC with different coating cycles; (c) Meso-Mn-AR and Meso-Mn-HC; and (d) Cu-incorporated Meso-Mn-HC.

3.3.4 H_2-TPR

Figure 3.9 gives the temperature programmed reduction profiles for Meso-Mn-HC and Cu/Mn 1:2-HC. Cu/Mn 1:2-HC was named as Meso-CuO/MnO_x-HC due to the phase segregation. Meso-Mn-HC displayed a two-step reduction profile. The reduction steps can be ascribed to $Mn_2O_3 \rightarrow Mn_3O_4 \rightarrow MnO$, as shown in Equations 3.1 and 3.2 below:

$$Mn_2O_3 + H_2 \rightarrow Mn_3O_4 + H_2O \qquad \text{Eqn. 3.1}$$

$$Mn_3O_4 + H_2 \rightarrow MnO + H_2O \qquad \text{Eqn. 3.2}$$

The assignment of the reduction peaks is consistent with a previously published paper from our group.[94, 95] After copper was introduced into the catalyst, the two reduction steps overlapped and only one reduction peak was observed in its TPR profile. This typical reduction profile for other copper manganese oxide is reported in the literature.[99, 100] This suggests in Cu-Mn-HC catalyst, Mn^{3+} was reduced to Mn^{2+} in one single step. Additionally, there is a shoulder peak at around 210°C, which is likely due to the reduction of Cu^{2+} to Cu^0. The reduction steps of copper and manganese cations were overlapped. Besides the difference in the number of reduction steps, Cu-incorporated Meso-Mn started to be reduced at a lower temperature, with the reduction peak temperature at 277°C. On the other hand, Meso-Co had a higher reduction temperature, with peak temperature of the first reduction step at 312°C. Therefore, addition of Cu into mesoporous manganese oxide increased its reducibility and helps the release of lattice oxygen. Increased lattice oxygen mobility usually leads to improved oxidation reaction activity. However, from Figure 3.8d and Table 3.1, there is no obvious difference between the activities of Cu/Mn 1:2-HC and Meso-Mn-HC. This will be discussed in detail in the next section.

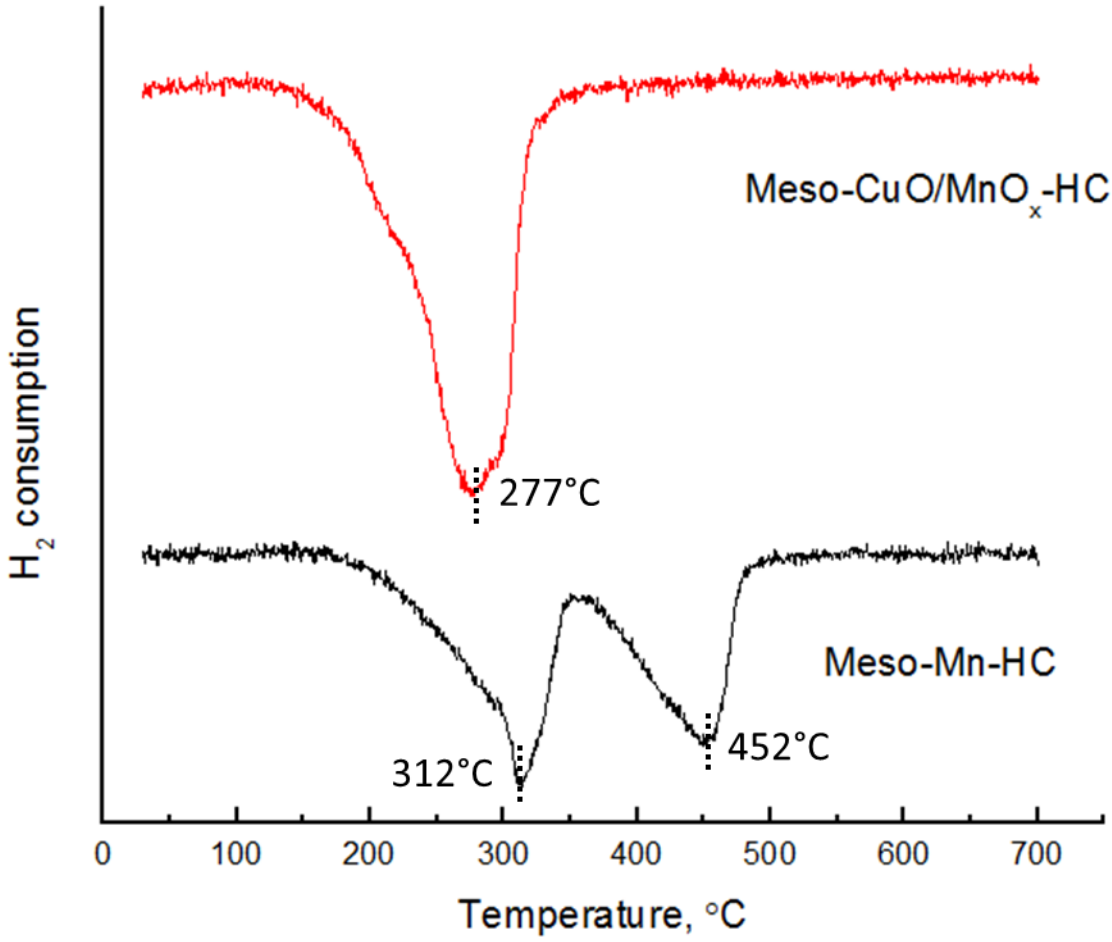

Figure 3.9 H_2-TPR reduction profiles for Meso-Mn-HC and Cu/Mn 1:2-HC.

3.3.5 Robustness Test

All the materials prepared were subjected to robustness tests to check the stability of the coating layer. Results were shown in Figure 3.10. The monolithic catalysts were sonicated in ethanol solution, and data were taken every 10 minutes. As shown in Figure 3.10b, c, the solution in the second vial, which contains Meso-Mn-DC sample, turned brown after 20 min sonication. While the ethanol solution in the other three vials remained transparent. This indicates that the in-situ coated sample mostly remain on the cordierite during the sonication process, showing much better stability than the dip coated sample. Figure 3.10a gives the quantified results. From the plot we can see that Meso-Ce-HC and 20%Mn-Co-HC experienced no weight loss during 20 min sonication, and Meso-Mn-HC had around a 90% weight maintained. On the other hand, Meso-Mn-DC suffered from more than 65% weight loss after the sonication process. This reveals the great advantage of the in-situ coating process in terms of coating layer stability.

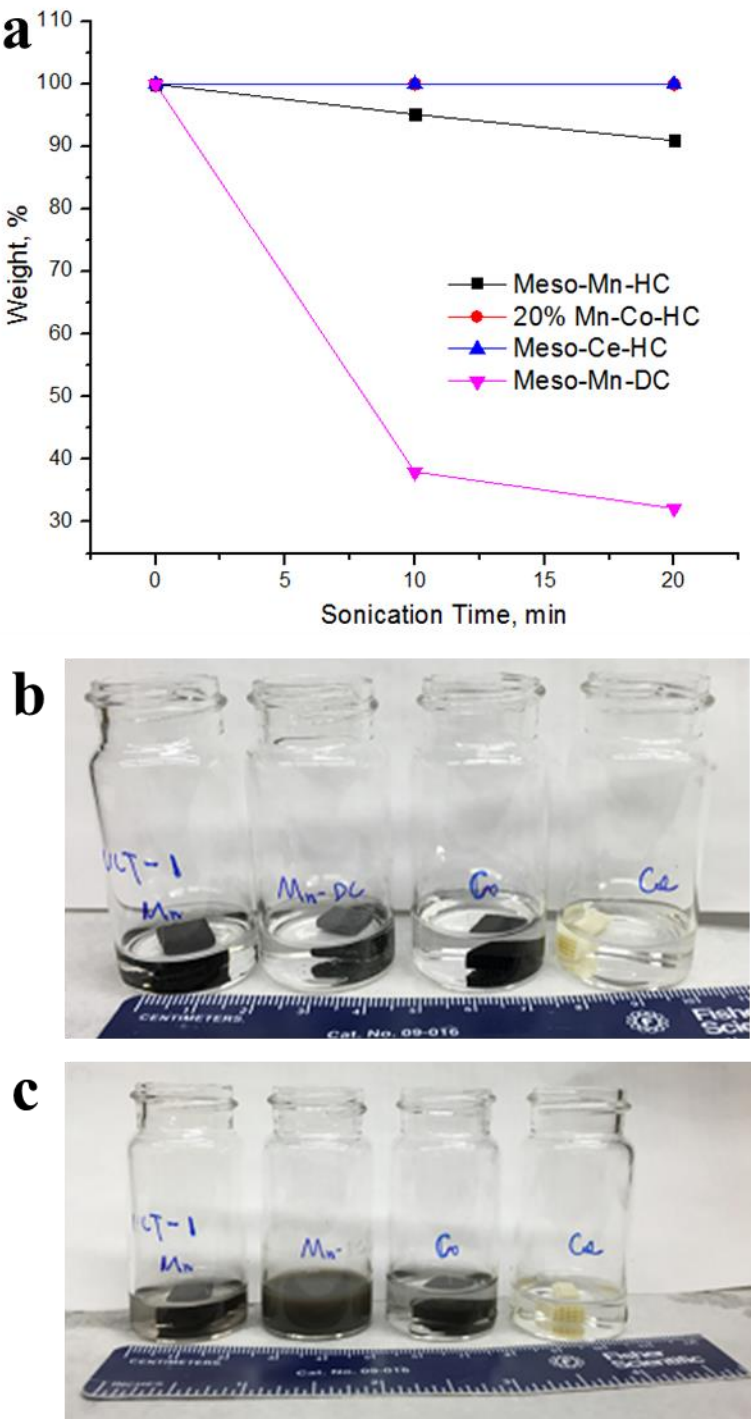

Figure 3.10 (a) Weight measurement of the monolithic catalysts after sonication in ethanol. Pictures of the samples (b) before and (c) after the sonication process. Samples in the vials from left to right: Meso-Mn-HC, Meso-Mn-DC, 20%Mn-Co-HC, and Meso-Ce-HC, respectively.

3.4 Discussion

In this chapter, a novel mesoporous soft template synthetic approach (UCT synthesis) was used to in-situ coat mesoporous metal oxides on cordierite honeycomb substrate. In a typical UCT procedure, metal precursors were dissolved in a solution containing 1-butanol, nitric acid and P123. With the Pluronic block copolymer P123 added, the viscosity of the solution was increased. Therefore, it is theoretically possible to let the metal oxide stick onto the substrate without the use of an extra binder. Section 3.3.1 has discussed and confirmed the in-situ coating of mesoporous manganese oxide, cobalt oxide, and cerium oxide, three top candidates for diesel oxidation applications among all the metal oxides. More importantly, the mesoporosity was maintained and confirmed by low angle PXRD patterns (Figure 3.1b, 3.2b, 3.4b and 3.5b). Due to the ordered mesostructure and fully exposed active sites, the prepared UCT monolithic catalysts showed very promising activities for CO oxidation reaction, as indicated in Figure 3.8. Furthermore, the robustness test shown in Figure 3.10 demonstrated that in-situ coated materials have much better stability than the dip coated sample. The UCT synthesis approach is generic for coating mesoporous metal oxides on cordierite without the use of additional binder.

Among all the discussed materials, mesoporous manganese oxide based samples have the largest loading amount on the cordierite. After carefully investigate the physicochemical properties of these different metal oxides, the UCT manganese oxide was found to have the smallest particle size.[48] Also, pure mesoporous cobalt oxide was difficult to adhere for the procedure on the substrate. The UCT cobalt oxide has a flower like structure with particle sizes on micrometer scale, much larger than the nano-sized particles of UCT manganese oxide. In general, smaller particles tend to stick on a substrate more easily and have a stronger adhesion force. While large particles have more chance to fall off the substrate. Therefore, to increase the loading amount of cobalt

oxide, decreasing the particle sizes becomes a powerful technique. From previous studies, manganese incorporation could help prevent the particle aggregation of cobalt oxide. The presence of a second component might hinder the crystal growth of cobalt oxide. In addition, the amorphous nature of UCT manganese oxide could help break down the flower like structure of cobalt oxide. As a result, 20%Mn-loaded mesoporous cobalt oxide ended up with random small nanoparticle morphology. Consequently, 20%Mn-Co-HC has a better coating on the substrate as indicated by the black color of the prepared material in Figure 3.5c. Pure mesoporous cobalt oxide coated sample still shows white color due to the exposure of bare substrate.

As indicated by Figure 3.8, almost all in-situ coated catalysts exhibited better activities than dip coated samples. One exception is Meso-Co-DC has slightly lower light off temperature than 20%Mn-Co-HC, which is likely due to the different loading amount. The in-situ prepared sample has more exposed active sites, larger surface area, and stronger adhesion to the substrate, contributing to higher activity. On the other hand, dip coated sample may sacrifice some catalytic activity due to the use of polymer binder. Therefore, UCT synthesis method is a promising technique for preparing monolithic catalysts for exhaust after treatment applications.

To further promote the activity of Meso-Mn-HC, three methods were used: multiple loading cycle, nanoarray coating and Cu incorporation. However as mentioned above, those materials all have different loading ratios. To make a fair comparison, CO oxidation activities need to be normalized to exact weight used in catalytic tests. Figure 3.11a displayed the CO activities for Meso-Mn-HC with multiple loading cycles normalized to weight. Meso-Mn-HC-1st showed the highest activity. However according to Figure 3.8b, Meso-Mn-HC-2nd and Meso-Mn-HC-3rd have lower light off temperature than Meso-Mn-HC-1st. Therefore, we can conclude the activity enhancement was due to increased loading amount. With the second and third layers coated on the

substrate, internal diffusion resistance was increased, which might be the reason for their lower activities shown in Figure 3.11a. Figure 3.11b demonstrate normalized activities for Meso-Mn-AR and Meso-Mn-HC. Meso-Mn-HC exhibited higher activities compared to Meso-Mn-AR, while Meso-Mn-AR had better performance than Meso-Mn-HC before normalization (Figure 3.8c). Again, the activity improvement shown in Figure 3.8c can be solely ascribed to weight increase. The nanoarray has larger surface area compared to bare substrate, which can provide more space for active layer coating. This can explain why Meso-Mn-AR has a higher loading ratio. Last but not least, Figure 3.11c compares normalized activities of Cu-incorporated Meso-Mn-HC. All the Cu-doped samples have higher activities than Meso-Mn-HC. Therefore, copper enhances the oxidation ability of Meso-Mn. Especially for Cu/Mn 1:2-HC, the sample exhibits the highest activity in Figure 3.11c and shows almost the same performance as Meso-Mn-HC. This indicates when ~33% Cu cation was added to the sample, its intrinsic activity can be largely promoted. Figure 3.9 displayed H_2-TPR results for Cu/Mn 1:2-HC and Meso-Mn-HC. According to this figure, Cu-loaded material has better reducibility, which can explain its higher activity. Copper has been reported to help the reduction process of manganese cations, leading to higher oxygen mobility in copper manganese oxide. Also, copper can have a spillover effect, which further facilitates the release of lattice oxygen from manganese oxide.[51, 96] All these properties give higher CO oxidation activity. Overall, Cu/Mn 1:2-HC demonstrated the best catalytic activity.

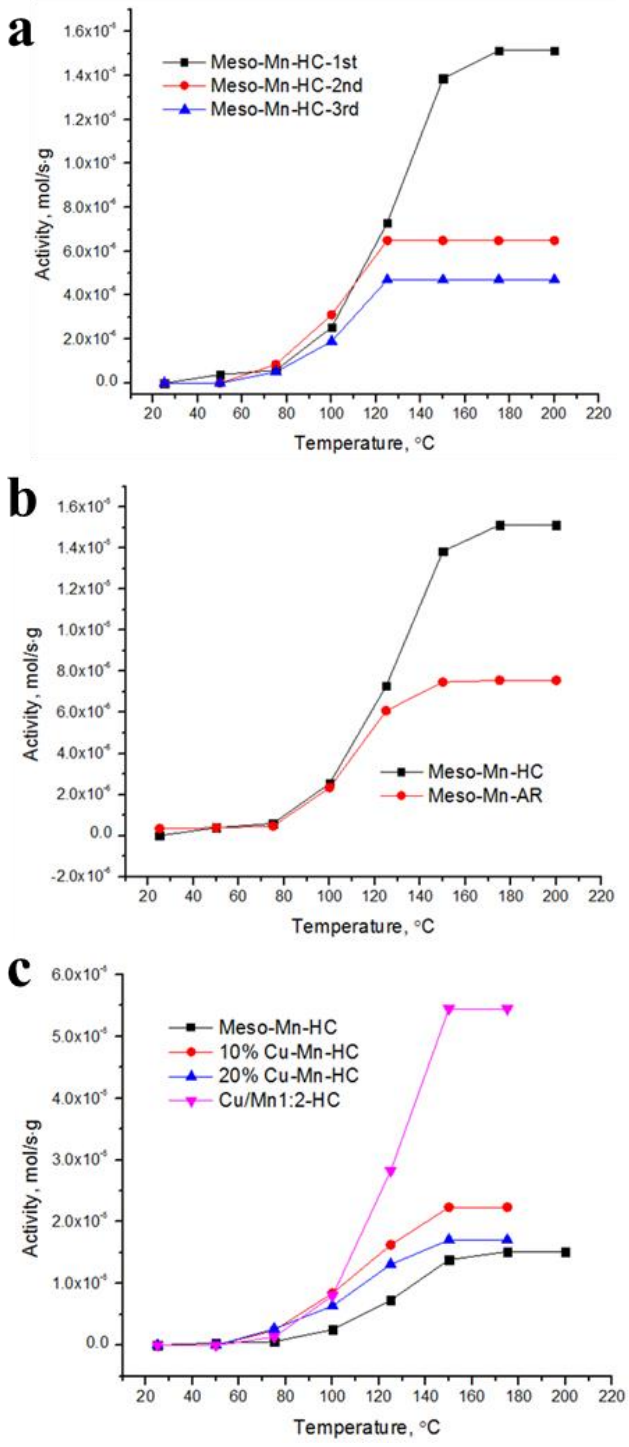

Figure 3.11 CO oxidation activities normalized to exact weight for (a) Meso-Mn-HC with different coating cycles; (b) Meso-Mn-AR and Meso-Mn-HC; and (c) Cu-incorporated Meso-Mn-HC.

3.5 Conclusions

Mesoporous manganese oxide, cobalt oxide, and cerium oxide have been successfully in-situ coated on cordierite honeycomb substrate without the addition of extra binder. The UCT method has been found to be generic for coating mesoporous metal oxides on cordierite. Manganese oxide based materials have the highest loading ratio on the substrate. The existence of the active layer on cordierite was confirmed by SEM characterization. Low angle PXRD results indicates that all the in-situ coated materials have an ordered mesostructure. Additionally, all the in-situ coated catalysts can have at least 90% weight retained after 20 min sonication in ethanol. However, the dip coated sample suffered from more than 65% weight loss after 20 min sonication process. For the same catalyst, the in-situ coated sample has higher CO oxidation activity than the dip coated sample, revealing the great advantage of eliminating the use of binder. The catalyst activity can be further promoted by multiple loading cycle, nanoarray coating and copper incorporation. The activity enhancement can be ascribed to increased loading amount and better reducibility.

CHAPTER 4. Ni AND Mn-SUBSTITUTED MESOPOROUS Co_3O_4 AS BIFUNCTIONAL CATALYSTS FOR OXYGEN REDUCTION REACTION AND OXYGEN EVOLUTION REACTION

4.1 Introduction

As previously stated, cobalt oxide has been discovered to be a green and active noble metal-free electrochemical catalyst for oxygen reduction and oxygen evolution reaction. In addition to the impressive electrochemical performance, considerable research has been focused on probing the active sites in Co_3O_4 structure for ORR and OER. Choi et al designed a $ZnCo_2O_4$ electrode with Co^{2+} replaced by Zn^{2+} and found this material was a better OER catalyst than Co_3O_4, suggesting Co^{2+} is not critical for catalyzing OER.[101] Dai et al. found that Co^{3+} is the active site for OER through XANES observations.[102] Recently, Sun et al. investigated plane-dependent activity of Co_3O_4. They demonstrated that catalyst with predominantly exposed {110} planes, which mainly consist of Co^{3+}, was the most active for OER.[103] Liu et al. however, claimed Co^{2+} is responsible for the formation of the OER active species CoOOH.[104] For ORR, Co^{2+} was usually considered as the active site. Guo et al. reported a controllable synthesis of Co_3O_4 with different exposed crystalline facets {111}, {100}, {110}, and discovered {111} plane was the most active for ORR due to its highest density of Co^{2+} cations.[105] Although the effect of surface valence states of Co on ORR and OER activities have been discussed extensively, conclusive evidence is still lacking and detailed scientific understandings are necessary to address the reaction mechanisms.

In terms of electrocatalytic activities, although a couple of cobalt oxide catalysts anchored on carbon support and cobalt oxides directly grown on conductive substrates like Ti or Ni foil have been reported as outstanding bifunctional catalysts of similar performance of precious metals,[27,

[106-108] comparable activities of mesoporous cobalt oxide freestanding nanoparticles have yet to be reported. In this study, we utilize the UCT synthesis approach to prepare Co_3O_4 based mesoporous materials as efficient catalysts for OER and ORR. Moreover, we will adjust the surface composition of Co_3O_4 by selective cation substitution to study the intrinsic active sites. Specifically, mesoporous Co_3O_4 as well as Ni/Mn incorporated Co_3O_4 was successfully synthesized. The best electrocatalytic activity was accomplished by 5% Ni doped Co_3O_4, with an overpotential of 399 mV for ORR (at 3 mA/cm^2) and 381 mV (at 10 mA/cm^2) for OER, on a par with the high quality Pt/C (389 mV for ORR) and Ir/C (346 mV for OER) catalysts and surpassing the performance of most cobalt based electrocatalysts published so far.[102, 109-111] Besides the distinguished activity, 5% Ni-loaded Co_3O_4 demonstrated little activity decay throughout 24 h continuous operation for both ORR and OER. Furthermore, for the first time we present a comprehensive investigation of the intrinsic active sites for ORR and OER by correlating different physicochemical properties such as surface area, surface oxidation states, structural defects to the electrochemical activities. This study could potentially serve as a helpful guidance towards the rational design of high performance electrocatalysts based on fundamental structure-activity relations.

4.2 Experimental Section

4.2.1 Chemicals.

Cobalt (II) nitrate hexahydrate ($Co(NO_3)_2{\cdot}6H_2O$, ≥98.0%), nickel (II) nitrate hexahydrate ($Ni(NO_3)_2{\cdot}6H_2O$, ≥98.5%), manganese (II) nitrate tetrahydrate ($Mn(NO_3)_2{\cdot}4H_2O$, ≥97.0%) 1-butanol (anhydrous, 99.8%), Poly(ethylene glycol)-block-Poly(propylene glycol)-block-Poly(ethylene glycol) PEO_{20}–PPO_{70}–PEO_{20} (Pluronic P123), nitric acid (68.0%-70.0% HNO_3), 20 wt % Pt/C, and 20 wt % Ir/C were all purchased from Sigma-Aldrich. 2-propanol (≥99.5%) was

purchased from J. T. Baker. Carbon black (Vulcan XC 72R) and 5 wt% Nafion dispersion D520 were purchased from Fuel Cell Store. Commercial Co_3O_4 (99.5%) was purchased from Strem Chemical Inc. and was denoted as C-Co_3O_4. All chemicals were reagent-grade and used as received without further purification.

4.2.2 Synthesis.

In a typical synthesis of pure mesoporous cobalt oxide, 5 g (0.017 mol) of $Co(NO_3)_2 \cdot 6H_2O$ was dissolved in a solution containing 17 g (0.33 mol) of 1-butanol, 2.4 g (0.038 mol) of HNO_3 and 2.5 g (4.31×10^{-4} mol) of P123. A clear gel was formed after stirring the above mixture at room temperature. The resulting transparent gel was then placed in an oven at 120ºC for 3.5 h. The obtained powder was washed several times with ethanol, centrifuged, and dried in a vacuum oven overnight. The dried powder was subjected to a heating cycle of 150ºC 12 h + 250ºC 2 h + 350ºC 1 h to obtain the final product. All the heating treatments were done under ambient condition. The sample was naturally cooled down to room temperature after each heating step. To synthesize metal substituted cobalt oxide, a certain amount of $Ni(NO_3)_2 \cdot 6H_2O$ or $Mn(NO_3)_2 \cdot 4H_2O$ was added to the solution at the beginning step according to the metal loading ratio. Other synthesis procedures were the same as that of pure cobalt oxide preparation. The total number of moles of the metal nitrate ($Co(NO_3)_2 \cdot 6H_2O$ + $Ni(NO_3)_2 \cdot 6H_2O$ or $Mn(NO_3)_2 \cdot 4H_2O$) remained unchanged (0.017 mol). The metal dopant amounts were 5, 10, 15 and 20 mol% with respect to the total metal precursors. The samples were labelled as X%M-Co, where X is 5, 10, 15, or 20, standing for the metal dopant loading percentages and M stands for metal dopant Ni and Mn.

4.2.3 Characterization.

Powder X-ray diffraction (PXRD) data were collected using a Rigaku Ultima IV diffractometer with Cu Kα radiation (λ = 1.5406 Å) at an operating voltage of 40 kV and a beam current of 44 mA. N_2 sorption analyses were performed on a Quantachrome Autosorb-1-1C automated sorption system. Morphological characterization was investigated with a Zeiss DSM 982 Gemini field emission scanning electron microscope (FE-SEM) with a Schottky emitter at an accelerating voltage of 2.0 kV. High-resolution transmission electron microscopy (HR-TEM) images and selected area electron diffraction (SAED) of the synthesized samples were collected by a JEOL 2010 FasTEM microscope operating at 200 kV with an energy dispersive X-ray spectroscopy (EDS) detector. X-ray Photoelectron Spectroscopy (XPS) measurements were studied on a PHI model 590 spectrometer with multiprobes (ΦPhysical Electronics Industries Inc.). The binding energies reported in this study were corrected for specimen charging by referencing them to the C 1s peak (set at 284.6 eV). Raman measurements were taken on a Renishaw 2000 Raman microscope attached to a charge-coupled device (CCD) camera with an Ar^+ laser at 514.4 nm as the excitation source. The spectrometer was calibrated by a silicon wafer before tests.

4.2.4 Electrochemical Measurements.

4.2.4.1 Cyclic Voltammetry (CV).

Electrochemical tests in this study were conducted in a three-electrode electrochemical cell on a CHI 660A electrochemical workstation at room temperature (22 ± 2°C). The cell consisted of an Ag/AgCl electrode in saturated KCl aqueous solution (0.197 V versus standard hydrogen electrode) as the reference electrode, a platinum wire as the counter electrode, and a sample modified pyrolytic graphite (PG) carbon electrode as the working electrode. A 0.1 M KOH solution (PH = 13) was used as the electrolyte. To prepare the working electrode, the pyrolytic graphite electrode was first polished with 600 grit SiC paper under wet conditions and sonicated

in ethanol for 2 min to achieve a clean and smooth electrode surface. Eight mg of active material and 2 mg of Vulcan XC 72R carbon were dispersed in 1.9 mL of 4:1 v/v water/ isopropanol mixed solvent, followed by adding 0.1 mL of 5 wt% Nafion solution (115 wt% of Nafion to catalyst ratio). Pt/C (20 wt% Pt on Vulcan XC 72) and Ir/C ink (20 wt% Ir on Vulcan XC 72) were prepared by dispersing 8 mg of the sample in 1.9 mL of 4:1 v/v water/ isopropanol mixed solvent with 0.1 mL of 5 wt% Nafion solution. The mixture was sonicated for at least 30 min to form a homogeneous ink. Twenty μL of the prepared suspension was then loaded onto a PG carbon electrode (5 mm in diameter) and dried overnight at ambient condition. The catalyst loading was ~0.408 mg/cm^2. Before each experiment, the cell was purged with O_2 (zero grade, Airgas) for 30 min, and the flow of O_2 was maintained over the electrolyte during the test to ensure continued saturation of O_2. The working electrode was cycled between -0.60 V and 0.10 V versus Ag/AgCl at a scan rate of 25 mV/s. The CV data were recorded until a reproducible scan was obtained. The background currents were analyzed by saturating the cell with Ar and measuring the CVs under the same condition as that was used in O_2 saturated environment. The CVs were iR-compensated prior to each run. All the potentials in this study were reported with respect to the reversible hydrogen electrode (RHE).

4.2.4.2 Linear Sweep Voltammetry-Rotating Disk Electrodes (LSV-RDEs).

The cell configuration and the preparation of the working electrode were the same as that stated above for CV tests. Linear sweep voltammograms (LSVs) were conducted on rotating disk electrodes (RDEs) with the aid of RDEV (Pine Instruments). The LSV was measured at a scan rate of 5 mV/s and a rotating rate of 1600 rpm in the potential range from 0.0 to -0.70 V for ORR and from 0.0 to 0.70 V for OER (vs. Ag/AgCl). In order to calculate the electron transfer number n for ORR on the basis of the Koutecky-Levich equation, LSVs were collected at various rotating speeds

(400, 900, 1200, 1600, and 2500 rpm). For both ORR and OER, all the experiments were performed in O_2 saturated electrolyte similar to the CV tests.

4.2.4.3 Electrochemical Impedance Spectroscopy (EIS).

The EIS test was carried out in the same three-electrode cell with continuous O_2 flow over the electrolyte at a rotating speed of 1600 rpm. Impedance data were recorded at -0.15 V vs Ag/AgCl (0.815 V vs RHE) for ORR and 0.65 V vs Ag/AgCl (1.615 V vs RHE) for OER. The spectra were collected in the frequency range of 0.1-10^5 Hz with a 5 mV amplitude.

4.2.4.4 Stability Test.

A pyrolytic graphite carbon electrode was used as the counter electrode instead of a Pt counter electrode to prevent any possible side reactions in long term durability tests. All the tests were done in O_2 saturated 0.1 M KOH solution with a working electrode rotated at 1600 rpm. The ORR stabilities were investigated by chronoamperometric responses of the catalysts with the potential kept at -0.4 V vs Ag/AgCl (0.565 V vs RHE). The OER durability tests were revealed using chronopotentiometry technology with the current density kept at 10 mA/cm^2 and potential window set between 0.5 and 1.0 V vs Ag/AgCl (1.465-1.965 V vs RHE). All the CVs and LSVs were iR compensated, however no iR compensation was applied for stability tests.

4.3 Results

4.3.1 Physicochemical Properties of Mesoporous Co_3O_4 and Initial Catalytic Results.

Mesoporous Co_3O_4 (Meso-Co) was prepared according to our newly discovered approach as stated above. As indicated by wide angle PXRD patterns in Figure 4.1a, Meso-Co as well as the commercial cobalt oxide sample (C-Co_3O_4) exhibited a typical Co_3O_4 spinel PXRD pattern

(JCPDS 43-1003). The nanocrystalline nature of Meso-Co was revealed by its relatively broad diffraction line, with an average particle size of 13.0 nm. The calculated Scherrer grain size of C-Co_3O_4 was around 89 nm. Similar to our previous work, the diffraction line in the low angle region (Figure 4.1b) and the Type IV adsorption isotherm (Figure 4.1c) of Meso-Co confirmed the existence of the mesostructure.[35, 112] However, C-Co_3O_4 failed to show a diffraction line in low angle PXRD, suggesting a nonporous structure. The electrocatalytic properties were evaluated for both oxygen reduction reaction (ORR) and oxygen evolution reaction (OER), and further compared with C-Co_3O_4 (Figure 4.1d). Meso-Co exhibited superior activity than C-Co_3O_4 by showing much smaller overpotential for ORR (569 mV at -3 mA/cm^2) and OER (396 mV at 10 mA/cm^2) which can be ascribed to the great advantage provided by the mesostructure and nanocrystalline nature of catalysts. Moreover, our Meso-Co surpassed the activity of similar types of materials reported in the literature. For example, Joo et al. carried out OER/ORR tests on mesoporous Co_3O_4 prepared by KIT-6 template and only showed an overpotential of 411 mV at 10 mA/cm^2 and 623 mV at -3 mA/cm^2.[110] However, compared to the state of the art precious metal based catalysts and Co_3O_4 on graphene/carbon nanotube covalent hybrid catalysts, Meso-Co showed limited activity, especially for ORR.[27, 113] Therefore, the activity of Meso-Co need to be further enhanced in order to become a competitive bifunctional catalyst. Ni doping has been reported to increase the conductivity and active site population of Co_3O_4,[114] meanwhile incorporation of a more active species Mn has been proven to promote the ORR activity.[115] Theoretically, these metal cations can be introduced into the Co_3O_4 framework because of their similar ionic radius and electronegativity. More interestingly, partially replacing the surface Co^{2+} and Co^{3+} by foreign cations enabled us to discover the inherent active species for catalyzing ORR and OER.

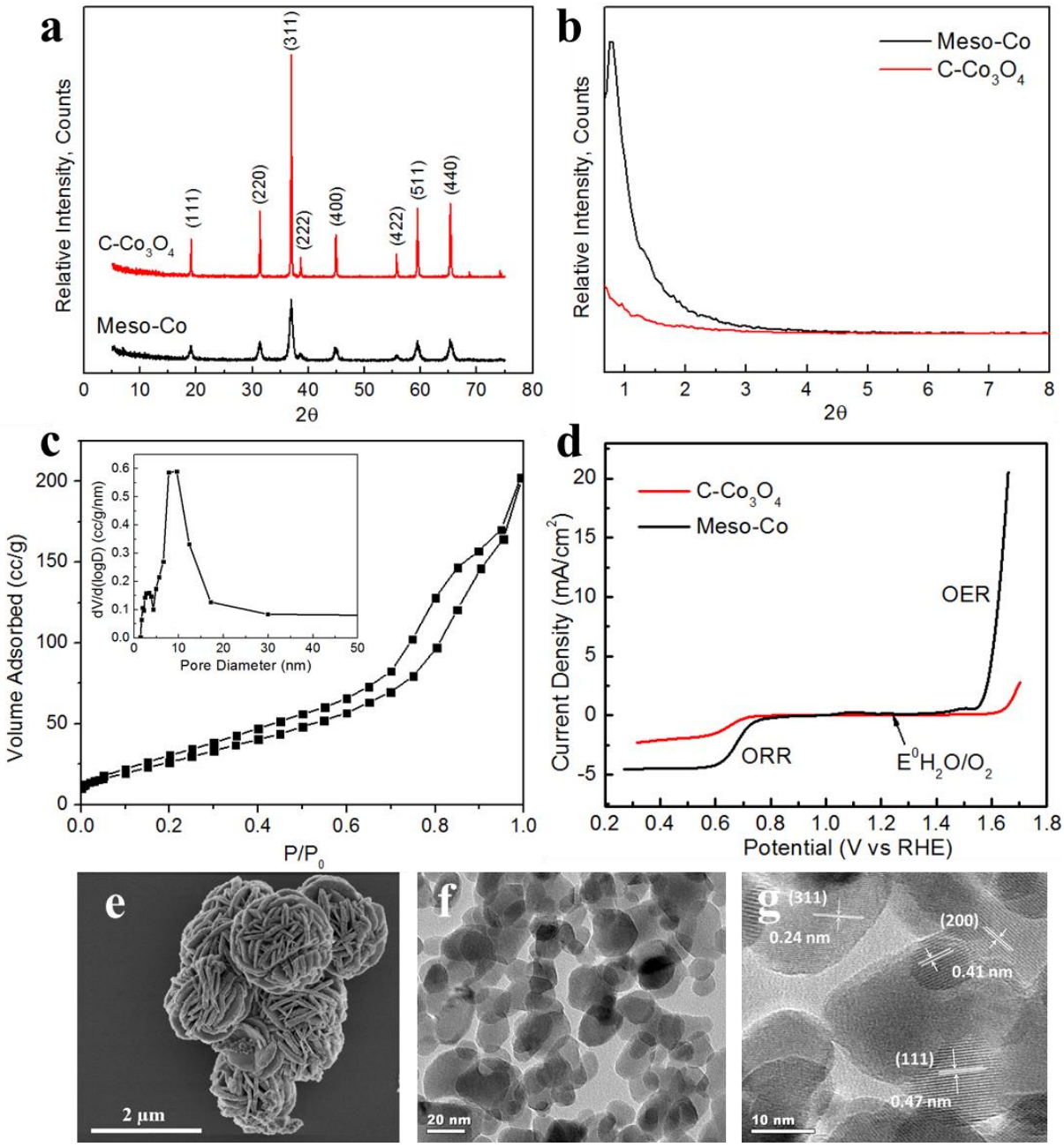

Figure 4.1 (a) Wide angle and (b) Low angle PXRD patterns of Meso-Co and C-Co_3O_4. (c) N_2 sorption isotherm with an inset of BJH pore size distributions of Meso-Co. (d) ORR and OER performance of Meso-Co and C-Co_3O_4. (e-g) FE-SEM, TEM, and HR-TEM images of Meso-Co.

4.3.2 Physicochemical Properties of Ni-Substituted Mesoporous Co_3O_4.

Two series of catalysts were prepared with various nickel and manganese loadings, respectively. The as-synthesized samples were denoted as X%M-Co hereafter (M = Ni, Mn, while X = 5, 10, 15, and 20, representing the metal doping/substitution percentages.). First, the physicochemical characteristics of Ni-substituted series X%Ni-Co were systematically reviewed. All the wide angle PXRD diffractograms of X%Ni-Co illustrated in Figure 4.2a showed the same pattern as the reference Meso-Co catalyst (JCPDS 43-1003), without any diffraction lines of Ni related compounds observed. This implied that no Ni precipitated out during the syntheses. With Ni doped into the Co_3O_4 lattice, 2θ positions of the diffraction lines shifted to lower degrees compared to Meso-Co, corresponding to expansion of the lattice constant. The shift of the 2θ position of the (440) planes, the planes showing the most obvious shift, were marked by a drop line as shown in Figure 4.2a. The estimated lattice parameter continuously increased from 8.0763 Å for Meso-Co to 8.1312 Å for 20%Ni-Co. The change in the size of the Co_3O_4 crystal lattice is likely caused by lattice distortion that confirms the incorporation of Ni into the Co_3O_4 structure and the formation of the Co-Ni-O solid solution. The doping percentages of Ni in the final products were determined by EDX analysis under TEM. As can be seen from Table 4.1, the Ni amount is 12.1%, 19.9%, 28.6%, and 35.5%, almost doubled the nominal ratios of the precursors. The PXRD patterns were also used to calculate the average particle sizes using the Scherrer equation. The crystallite sizes of all the samples range from 6.2 to 13.0 nm. The particle size is smaller for the Ni-substituted Co_3O_4 than that of the pure Co_3O_4, and generally shows a decreasing trend with the increase of the Ni amount. The presence of the second metal component Ni hindered the crystallization of Co_3O_4, and the increased crystallographic disorder in the Co-Ni-O mixed oxides might also result in decreased crystallite sizes.

Despite the structure distortion revealed from high angle PXRD patterns, all the materials maintained their mesoporosities. Meso-Co and all the Ni substituted samples diffracted in the low angle region (Figure 4.2b). In addition, a type IV adsorption isotherm along with a type I hysteresis loop shown in N_2 sorption analyses (Figure 4.2c) confirmed a regular cylindrical mesostructure. The porous network formed in between the particles can be clearly seen in TEM images (Figure 4.2e, g). Figure 4.2d presented Barrett-Joyner-Halenda (BJH) pore size distribution, suggesting monomodal pore size distributions of all materials. The surface areas of X%Ni-Co were found to be similar (~150 - 160 m^2/g) in spite of different Ni amounts, which are all higher than that of the Meso-Co (109 m^2/g). The larger surface area is likely due to the morphology change after Ni incorporation. Unlike the aggregated microspheres for Meso-Co, X%Ni-Co exhibited nanosheet morphologies in SEM (Figure 4.2f and 4.3) with more open structures and less extent of aggregation, leading to higher surface areas. Figure 4.2e presents high-resolution TEM images of 5%Ni-Co, showing average particle size of ca. 10 nm, matching well with Scherrer crystallite size calculated from PXRD patterns (9.0 nm). The d spacing values were measured to be 0.24, 0.28, and 0.47 nm, attributed to (311), (220), and (111) planes of Co_3O_4, respectively. The SAED ring patterns shown in the inset of Figure 4.2e clearly displayed the Debye-Scherrer rings which can also be indexed to the above planes of the Co_3O_4 spinel structure.

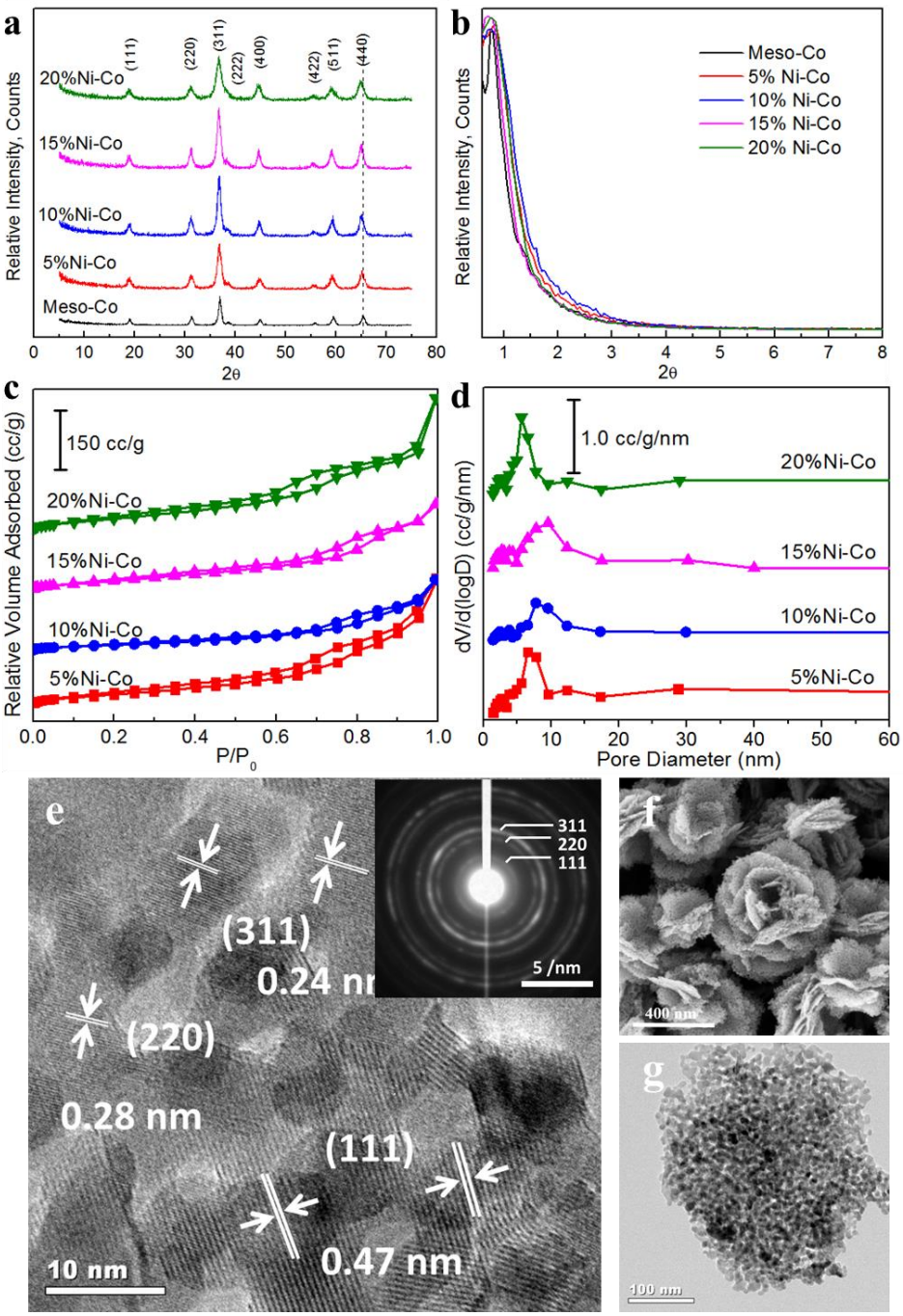

Figure 4.2 Structural characterizations of Ni-substituted mesoporous Co_3O_4: (a) Wide angle and (b) Low angle PXRD patterns, (c) N_2 sorption isotherms and (d) BJH desorption pore size distributions of X%Ni-Co (X = 5, 10, 15, and 20) and Meso-Co samples. (e) HR-TEM with an inset of SAED pattern, (f) SEM, and (g) TEM of 5%Ni-Co.

Table 4.1 Structural Parameters of Different Mesoporous Cobalt Oxide Samples Characterized in This Study.

Material	BET Surface Area (m^2/g)	BJH Des. Pore Volume (cm^3/g)	BJH Des. Pore Diameter (nm)	Lattice Constant (Å)	Scherrer Crystallite Size (nm)	X/(X+Co) atomic ratio (X=Ni/Mn) by EDS
Meso-Co	109	0.341	7.7	8.076	13.0	0
5%Ni-Co	160	0.551	6.5	8.096	9.0	0.121
10%Ni-Co	153	0.398	7.7	8.108	9.5	0.199
15%Ni-Co	149	0.326	9.5	8.117	8.28	0.286
20%Ni-Co	164	0.582	5.6	8.131	6.2	0.355
5%Mn-Co	127	0.234	7.7	8.077	12.8	0.010
10%Mn-Co	135	0.359	9.5	8.091	7.1	0.117
15%Mn-Co	174	0.435	12.3	8.102	6.5	0.152
20%Mn-Co	199	0.432	9.5	8.118	4.6	0.268

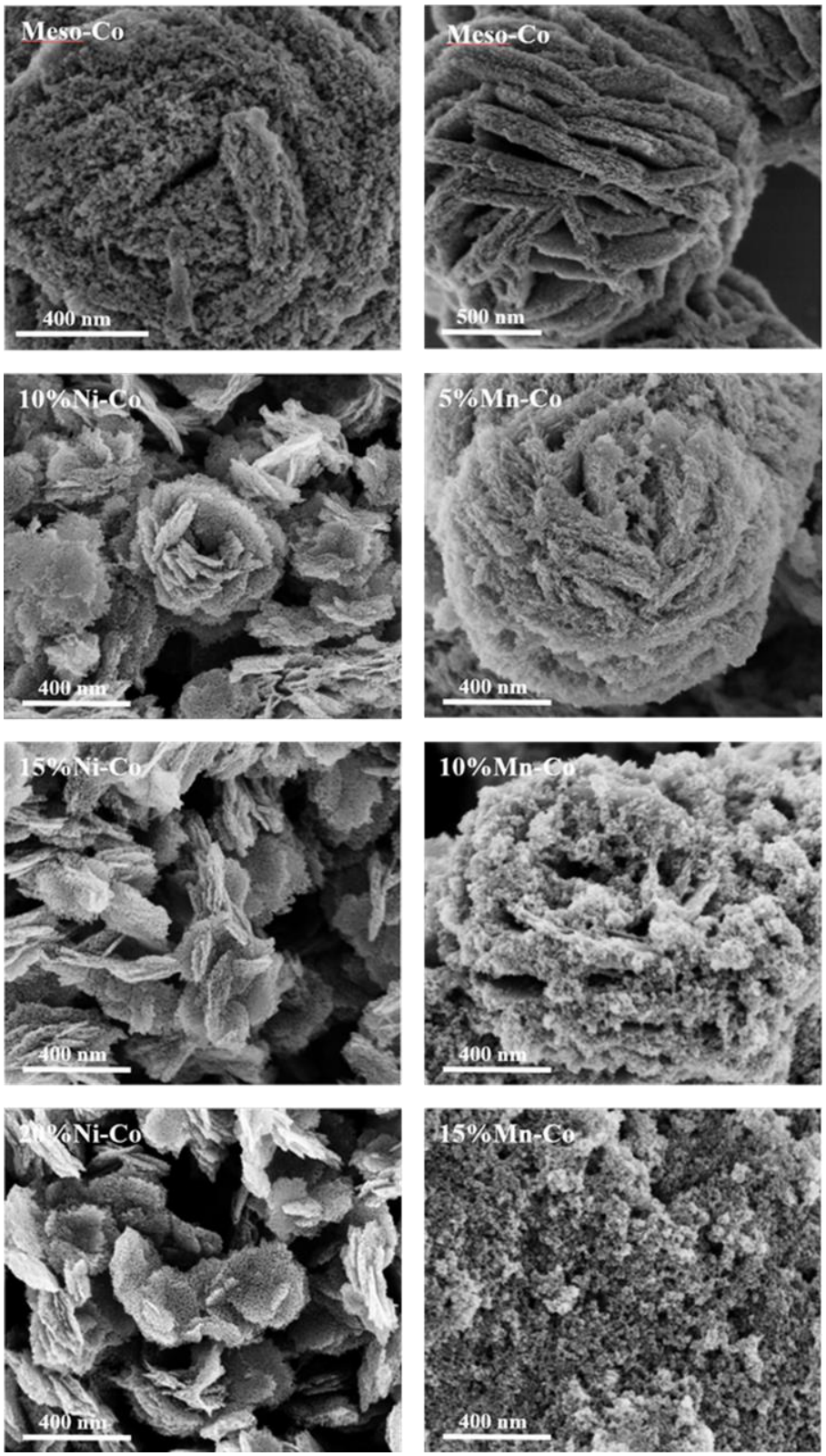

Figure 4.3 SEM images of Meso-Co, X%Ni-Co (X = 10, 15, 20) and X%Mn-Co (X = 5, 10, 15).

4.3.3 Physicochemical Properties of Mn-Substituted Mesoporous Co_3O_4.

Similar to the Ni-substituted catalyst series, the basic physicochemical properties of Mn-substituted Co_3O_4 system were also evaluated by PXRD, N_2 sorption, SEM, EDX and TEM techniques. All the diffraction lines in the wide angle PXRD patterns shown in Figure 4.4a were attributed to the Co_3O_4 crystal structure. After Mn was introduced to the catalyst system, the expansion of the unit cell and decrease of the particle grain size caused by lattice distortion and Co_3O_4 crystallization inhibition were observed by wide angle PXRD patterns as expected (Figure 4.4a and Table 4.1). However, the change of the lattice constant of X%Mn-Co with various Mn amounts was relatively small when compared with Ni (Table 4.1), which indicates it is more difficult for Mn to go into the Co_3O_4 crystal structure. The excessive Mn ions may be eliminated by a washing process. The 5%Mn-Co sample had almost the same lattice parameter as Meso-Co (8.0769 vs 8.0763 Å), and the lattice constant slowly increased to 8.1175 Å until the nominal Mn/(Co+Mn) ratio reached 20% (Table 4.1). EDX analyses were also conducted and the Mn/(Mn+Co) atomic ratios for X%Mn-Co were found to be 0.010, 0.117, 0.152, and 0.268 where X equaled to 5, 10, 15, and 20, respectively. The addition of Mn induced significant changes in particle grain sizes (Table 4.1). The 20%Mn-Co system had a Scherrer crystallite size of 4.6 nm, less than a half of the size for Meso-Co (13.0 nm), and smaller than that of 20%Ni-Co (6.2 nm). The small grain size of 20%Mn-Co was further evidenced by high-resolution TEM image shown in Figure 4.4e. The mesoporous structure of X%Mn-Co was maintained as confirmed by low angle PXRD patterns (Figure 4.4b), N_2 sorption measurements (Figure 4.4c), and TEM (Figure 4.4e, g). Figure 4.4d demonstrated the narrow BJH pore size distributions of the materials, with pore diameters in the range of 7.7 – 12.3 nm. The incorporation of Mn greatly enhanced the surface area of the catalyst, with the highest surface area of 199 m^2/g achieved by the 20%Mn-Co sample.

The enlargement of the surface area can also be related to the morphologies of the catalysts. The morphologies shown in SEM images of Mn-incorporated Co_3O_4 consist of nanosized small round particles without aggregation to nanosheets or microspheres, giving rise to larger surface areas versus the Meso-Co or X%Ni-Co materials (Figure 4.3 and 4.4f). Smaller grain sizes of Co-Mn-O mixed oxides could also be responsible for their higher surface areas. The clear lattice fringes in HR-TEM images and the SAED ring patterns illustrated in Figure 4.4e confirm the good crystallinity of our synthesized mesoporous materials and match well with the wide angle PXRD patterns (Figure 4.4a).

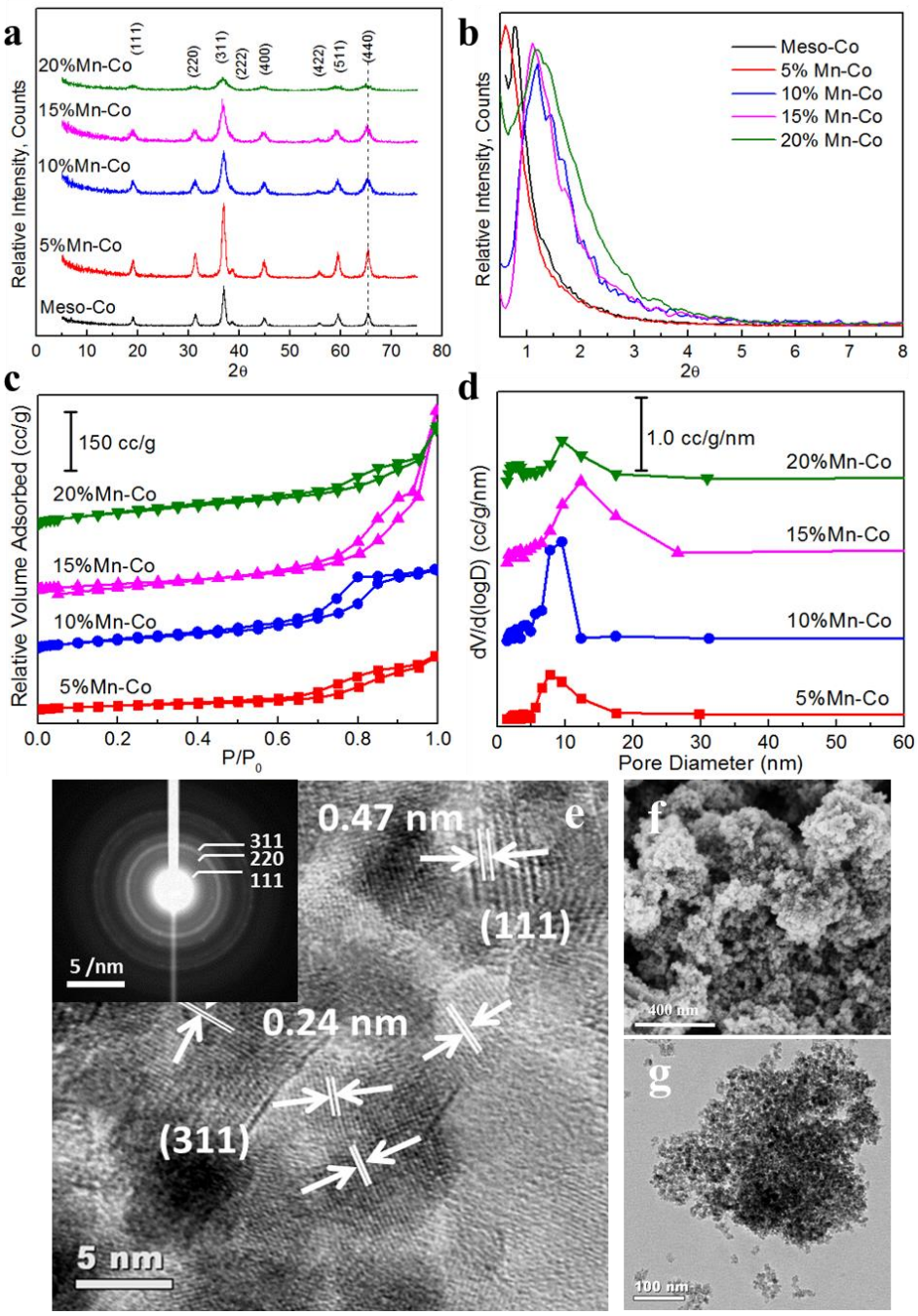

Figure 4.4 Structural characterizations of Mn-substituted mesoporous Co_3O_4: (a) Wide angle and (b) Low angle PXRD patterns, (c) N_2 sorption isotherms and (d) BJH desorption pore size distributions of X%Mn-Co (X = 5, 10, 15, and 20) and Meso-Co samples. (e) HR-TEM with an inset of SAED pattern, (f) SEM, and (g) TEM of 20%Mn-Co.

4.3.4 ORR Activities of Ni-Substituted Mesoporous Co_3O_4.

The ORR catalytic activities of Ni promoted mesoporous cobalt oxide were first characterized by cyclic voltammetry (CV) in both O_2 and Ar-saturated 0.1 M KOH solution and compared with that of pure mesoporous cobalt oxide. The results are displayed in Figure 4.5a. No discernible redox peaks were observed in the CV data collected under Ar, indicating no reaction happens under Ar-saturated conditions in this potential window. Therefore the reduction peaks in the voltammogram in O_2-saturated solution can be considered as reduction reactions of oxygen only. Upon incorporation of Ni into Co_3O_4, the catalyst showed a larger loop in the CVs under Ar atmosphere compared with pure Co_3O_4, suggesting an increased electrochemically active surface area of Ni-substituted cobalt oxide. All the Ni doped Co_3O_4 exhibited similar voltammograms under Ar independent of the Ni loading amount. In O_2-saturated solution, 5%Ni-Co showed a peak potential of 0.81 V, which is much more positive than that of Meso-Co (0.67 V). The higher activity of 5%Ni-Co can also be demonstrated by its much higher peak current density than Meso-Co. However, further increasing the dopant amount does not contribute to improved ORR activity. In general, the position of the peak potential or onset potential in ORR voltammograms reveals the intrinsic properties of active sites, while the peak current density can be correlated with the number of effective or accessible active sites for ORR. This preliminary evaluation of ORR activity by CV demonstrates the remarkable promotion effect of Ni in Co_3O_4. Although $Ni_xCo_{3-x}O_4$ for the application in ORR has been extensively studied[111, 116] it has never been perceived that small Ni doping amounts lead to huge activity improvement while increased Ni incorporation does not contribute to further improvement.

To eliminate the mass transport effect and further investigate the ORR kinetics, rotating disk electrode (RDE) measurements of Ni-substituted cobalt oxide were carried out. Figure 4.5b

displays the linear sweep voltammetry (LSV) curves collected at a rotation rate of 1600 rpm in 0.1 M KOH solution. The activity trend of the catalysts is similar to that observed by CV measurements. The 5%Ni-Co sample demonstrates the best activity by showing a potential of 0.83 V to reach a current density of 3 mA/cm^2, which is a generally used figure of merit to quantify ORR activity. The required potential slightly decreased to 0.80 V when the Ni loading amount was increased to 20%. However the potential is still much more positive than the potential needed for Meso-Co (0.66 V). All the X%Ni-Co (X = 5, 10, 15 and 20) exhibited very similar onset potentials at around 0.87 V. The onset potential is defined as the potential at which 10% of the peak current density was reached.[117]. The performance of 5%Ni-Co is superior to most similar catalysts published in the literature so far. The potential required to reach 3 mA/cm^2 for a recently developed mesoporous $NiCo_2O_4$ nanowire array was roughly at 0.685 V with a rotating rate of 2500 rpm.[111] The peak potential of an urchin-like $NiCo_2O_4$ sphere in CV was located at 0.61 V.[116] Since the testing conditions are varied in these previously reported catalysts, it is more convincing to compare our catalysts to the state of the art 20 wt% Pt/C at the same mass loading in the same measurement system. Figure 4.5b also shows the potential of Pt/C is 0.84 V at a current density of 3 mA/cm^2 is only 10 mV more positive than that of 5%Ni-Co. Moreover, 5%Ni-Co outperformed the benchmarking Pt/C catalyst in terms of the diffusion limiting current density. The number of electrons transferred per O_2 molecule (n) was calculated from the slopes of Koutecky-Levich (K-L) plots at potentials between 0.60 and 0.30 V. Figure 4.6 showed LSV curves collected at 400, 900, 1200, 1600 and 2500 rpm for all the catalysts and the corresponding K-L plots. The calculated average n together with other performance parameters are summarized in Table 4.2. The good linearity of the obtained K-L plots indicates first-order kinetics with respect to the concentration

of O_2.[118] The electron transfer number of 5%Ni-Co is ~4.0, suggesting a direct four electron reduction pathway without peroxide formation, the same as the commercial Pt/C catalyst (n ~4.0).

Additionally, we employed electrochemical impedance spectroscopy (EIS) techniques to gain insight into the catalytic behavior of Ni doped Co_3O_4 during ORR. The EIS was conducted at 0.815 V, which is within the ORR active potential region of X%Ni-Co as well as Pt/C, between 0.1 and 10^5 Hz (Figure 4.5c and d). The resistance in the high frequency region (the intercept on the real axis near the origin of the plot) is due to the solution resistance (R_s). The charge transfer resistances (R_{ct}) of the materials were obtained from a fitted equivalent circuit model called the simplified Randles Cell. As shown in the Nyquist plot in Figure 4.5c, 5%Ni-Co showed a much smaller semicircle than Meso-Co, with an R_{ct} value of 68 Ω, which is much smaller than that of Meso-Co (1852 Ω). Figure 4.5d compares R_{ct} values between catalysts doped with different amounts of Ni and further compared with commercial Pt/C catalyst. The 5%Ni-Co and 10%Ni-Co samples showed similar R_{ct} values (68 and 67 Ω) that are commensurate with Pt/C (68 Ω). The 15%Ni-Co and 20%Ni-Co samples showed slightly larger R_{ct} values (79 and 81 Ω, respectively). Lower charge transfer resistance corresponds to faster electron transfer rate and higher ionic conductivity, which are key factors for efficient ORR catalysts. Overall, the R_{ct} measured by EIS is consistent with the ORR activities via RDE and CV. This result confirms that the incorporation of Ni can improve the conductivity of Co_3O_4 catalysts.

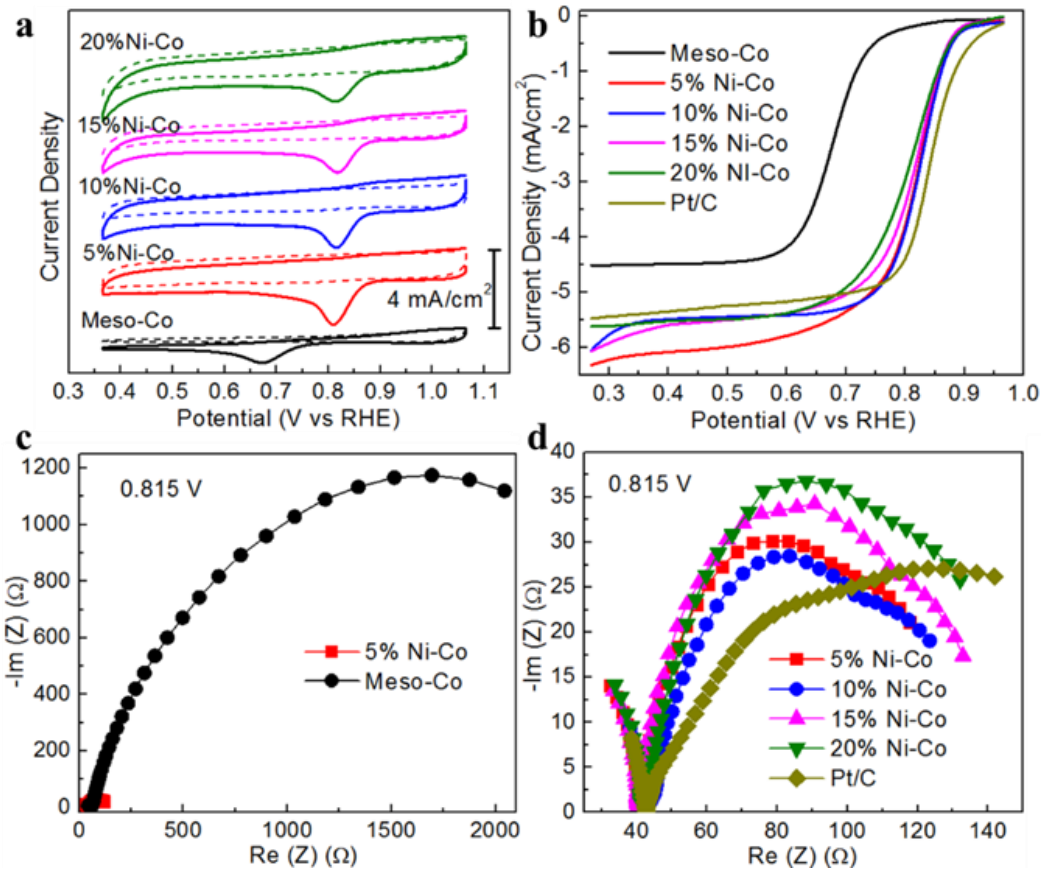

Figure 4.5 ORR catalytic activities of Ni-substituted mesoporous Co_3O_4: (a) CV voltammograms of Meso-Co and X%Ni-Co (X = 5, 10, 15, and 20) in O_2-saturated (solid line) and Ar-saturated (dash line) 0.1 M KOH at a scan rate of 25 mV/s. CV responses were continuously recorded until reproducible cycles could be obtained. (b) LSV curves of X%Ni-Co (X = 5, 10, 15, and 20), Meso-Co and Pt/C samples carried out in O_2-saturated 0.1 M KOH solution at a rotation rate of 1600 rpm and a sweep rate of 5 mV/s. Nyquist plots derived from EIS measurements in O_2-saturated 0.1 M KOH at 0.815 V of (c) 5%Ni-Co and Meso-Co, and (d) X%Ni-Co with different Ni loading amount (X = 5, 10, 15, and 20) and Pt/C catalysts.

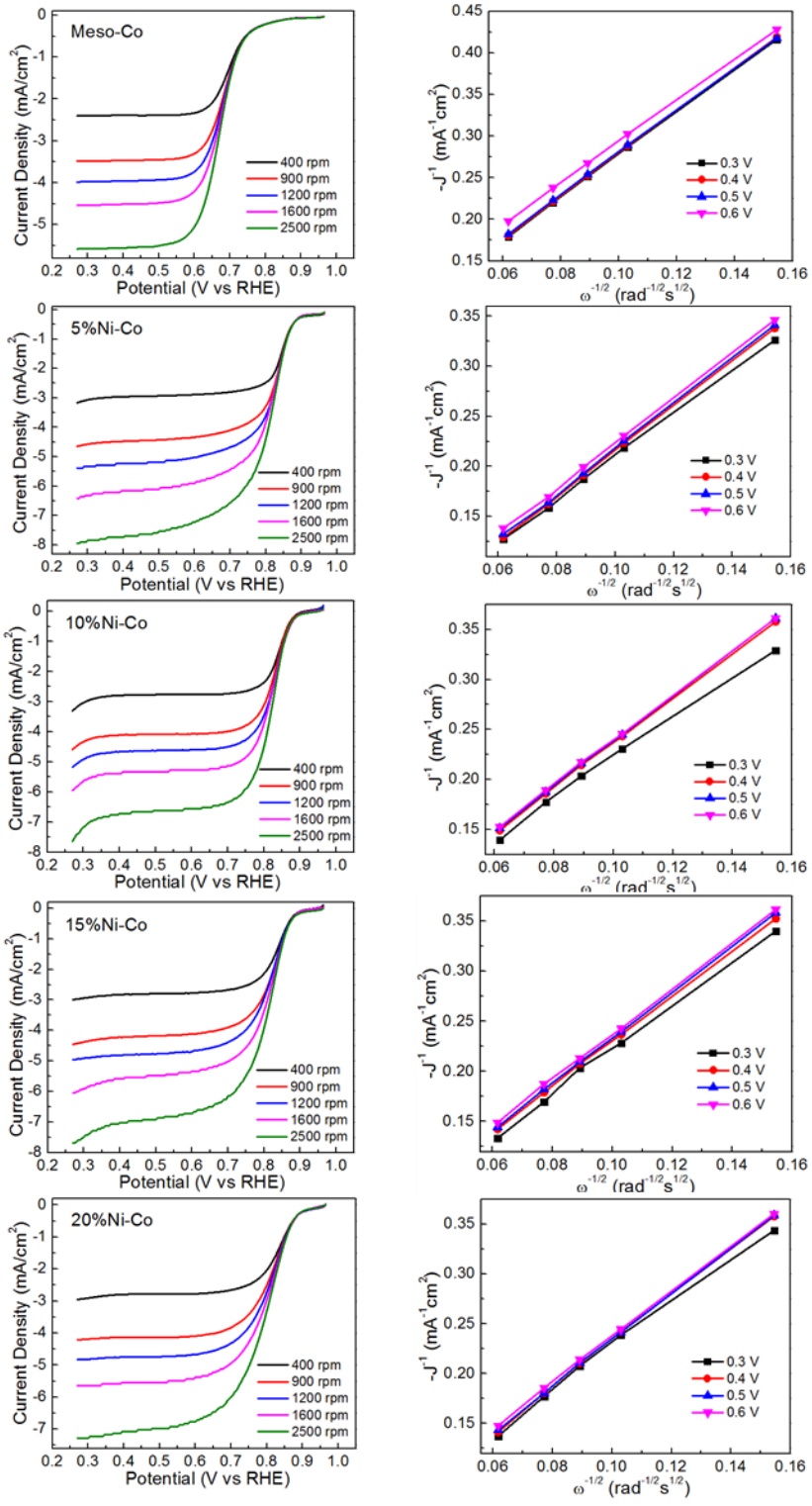

Figure 4.6 LSV curves of Meso-Co and X%Ni-Co (X = 5, 10, 15 and 20) collected at different rotation speeds indicated with their corresponding K-L plots shown on the right.

Table 4.2 Summary of the ORR and OER Catalytic Activities for the Studied Catalysts.

Catalyst	ORR				OER		
	Onset potential E_0 (V)	E at J = -3 mA cm^{-2} (V)	Electron transfer number n	Resistance R_{ct} (Ω)	E at J = 10 mA cm^{-2} (V)	Tafel slope (mV dec^{-1})	Resistance R_{ct} (Ω)
Meso-Co	0.75	0.66	~3.6	1852	1.62	74	81
5%Ni-Co	0.87	0.83	~4.0	68	1.61	73	50
10%Ni-Co	0.87	0.82	~4.0	67	1.60	83	52
15%Ni-Co	0.87	0.81	~4.0	79	1.62	79	49
20%Ni-Co	0.87	0.80	~4.0	81	1.61	82	47
5%Mn-Co	0.75	0.66	~3.7	1624	1.63	82	58
10%Mn-Co	0.83	0.69	~4.0	245	1.63	99	64
15%Mn-Co	0.87	0.73	~4.0	145	1.63	100	60
20%Mn-Co	0.9	0.81	~4.0	78	1.65	114	65
20 wt % Pt/C	0.91	0.84	~4.0	68	n/a	n/a	n/a
20 wt % Ir/C	0.81	0.65	n/a	n/a	1.58	72	42

"n/a" stands for data not applicable.

4.3.5 ORR Activities of Mn-Substituted Mesoporous Co_3O_4.

The same CV procedures as those for Ni-substituted series, were used to evaluate the ORR activities for Mn-substituted Co_3O_4 catalysts (Figure 4.7a). No obvious features were observed in Ar-saturated solution, confirming that the reduction peaks observed under O_2-saturated condition were due to the oxygen reduction reaction. Unlike the Ni doped Co_3O_4 system, the different doping amounts of Mn gave rise to a clear difference in the activity, as shown by the monotonous increase of ORR activities with increased Mn incorporation. This is indicated by the continuous increase of the CV loops under Ar atmosphere, with 20%Mn-Co exhibiting almost a 4-fold higher current density than Meso-Co. The reduction peak potential was increased from 0.67 V of Meso-Co to roughly 0.80 V for 20%Mn-Co. RDE was also employed to investigate the precise kinetics of the electrocatalytic activities of X%Mn-Co (X = 5, 10, 15 and 20) with Meso-Co and Pt/C catalysts included for comparison (Figure 4.7b). Higher Mn substitution amounts were found to favor the ORR activity. With 20%Mn doped in Meso-Co, the onset potential reached 0.90 V, which is very comparable to 0.91 V achieved by Pt/C, the well-known best catalyst for ORR. In order to reach a current density of 3 mA/cm^2, 20%Mn-Co required a potential of 0.805 V, 35 mV more negative than the Pt/C reference material. In spite of this, 20%Mn-Co surpassed the activity of Pt/C at 0.7 V and ended with a larger diffusion limiting current density, indicating higher intrinsic activity, a higher number of catalytic sites, or both. Compared with literature reports so far, our catalyst is one of the best catalysts for ORR among Co and Mn mixed spinel free nanoparticles. The $Co_xMn_{3-x}O_4$ nanocrystalline spinel prepared by rapid room-temperature synthesis had an onset potential at around 0.895 V in 0.1 M KOH.[119] Likewise, the onset potential of another Mn doped Co oxide $Mn_y{\cdot}Co_yO_x/C$ was at roughly 0.85 V.[120] Besides, a well dispersed Co_3O_4/Co_2MnO_4 nanocomposite needed about 0.68 V to reach 3 mA/cm^2 current density.[121] The average electron transfer number

n of 20%Mn-Co was calculated to be ~4.0 from the K-L plots, larger than ~3.6 for Meso-Co, implying a quasi-4-electron process. The parallel fitted lines in K-L plots indicate similar calculated n values at potentials between 0.3-0.6 V (Figure 4.8).

The EIS results for Mn loaded Co_3O_4 are presented in Figure 4.7c. With increasing Mn content, the diameter of the semicircle in the Nyquist plot keeps decreasing. The measured R_{ct} values follow the order Meso-Co > 5%Mn-Co > 10%Mn-Co > 15%Mn-Co > 20%Mn-Co > Pt/C, showing an inverse relationship with the activity trend demonstrated by CV and RDE measurements (See Table 4.2 for details). Incorporation of Mn helps the efficient charge transport during the ORR process, thus facilitating the ORR activity. The smallest Rct value was achieved by 20%Mn-Co (78 Ω), which exhibited the best activity among different Mn-substituted Co_3O_4. In summary, doping either Ni or Mn into Co_3O_4 is able to enhance ORR activity with more positive onset and peak potentials, larger average electron transfer numbers and smaller charge transfer resistance. Increased Mn content in Co_3O_4 leads to better activity, the activities of Ni-substituted Co_3O_4 are almost independent of the Ni doping concentration.

Besides the excellent activity, a promising ORR catalyst must demonstrate outstanding stability. Long-term durability tests were thus performed by chronoamperometry techniques at a constant voltage of 0.565 V on 5%Ni-Co and 20%Mn-Co, which are the best catalysts in the X%Ni-Co and X%Mn-Co series. Pt/C was also studied for comparison. As shown in Figure 4.7d, 5%Ni-Co was able to maintain ~95% of its initial current density throughout the 24 hours of continuous operation, exhibiting remarkable stability. The 20%Mn-Co material also showed very good stability with ~89% of current density sustained after 24 hours. However, the state of the art Pt/C catalyst suffered ~25% current decay during the test with inferior stability to our mesoporous 5%Ni-Co and 20%Mn-Co catalysts. This result reveals the distinguished stability of our

mesoporous catalysts and their potential to replace traditional precious metal based catalysts in applications for fuel cells or metal air batteries. To the best of our knowledge, the stabilities of our catalysts over such a long period of lifetime are the best reported so far. Similar durability tests have been conducted on various types of catalysts only within a relative short period of time (< 10 h).[109, 113, 122]

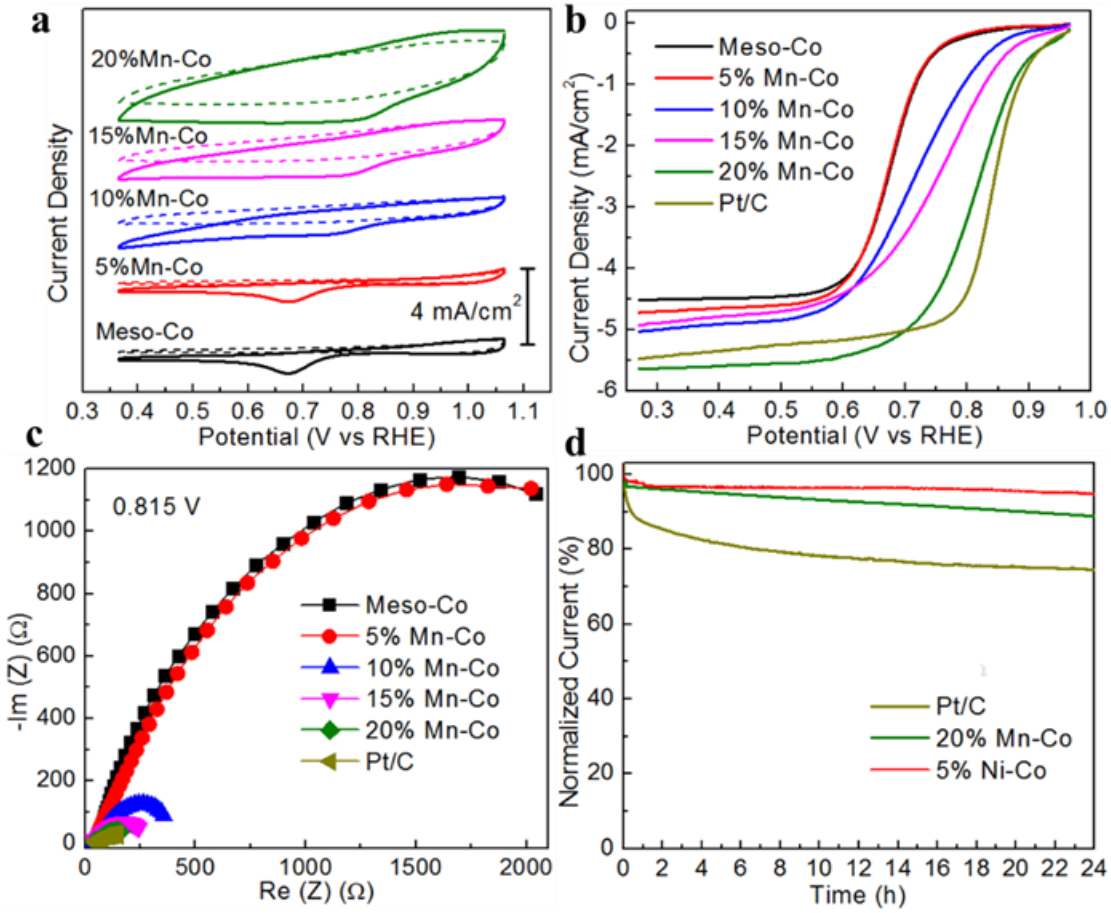

Figure 4.7 ORR performance of Mn-substituted mesoporous Co_3O_4: (a) CV voltammograms of Meso-Co and X%Mn-Co (X = 5, 10, 15, and 20) in O_2-saturated (solid line) and Ar-saturated (dash line) 0.1 M KOH at a scan rate of 25 mV/s. Multiple CV responses were monitored until a reproducible scan was attained. (b) LSV curves at a rotation rate of 1600 rpm and a sweep rate of 5 mV/s, and (c) Impedance data at 0.815 V in O_2-saturated 0.1 M KOH of X%Mn-Co (X = 5, 10, 15, and 20), Meso-Co and Pt/C catalysts. (d) Chronoamperometric responses (i-t curves) conducted in O_2-saturated 0.1 M KOH on 5%Ni-Co, 20%Mn-Co and Pt/C modified PG carbon electrodes under a constant potential of 0.565 V and a rotation rate of 1600 rpm.

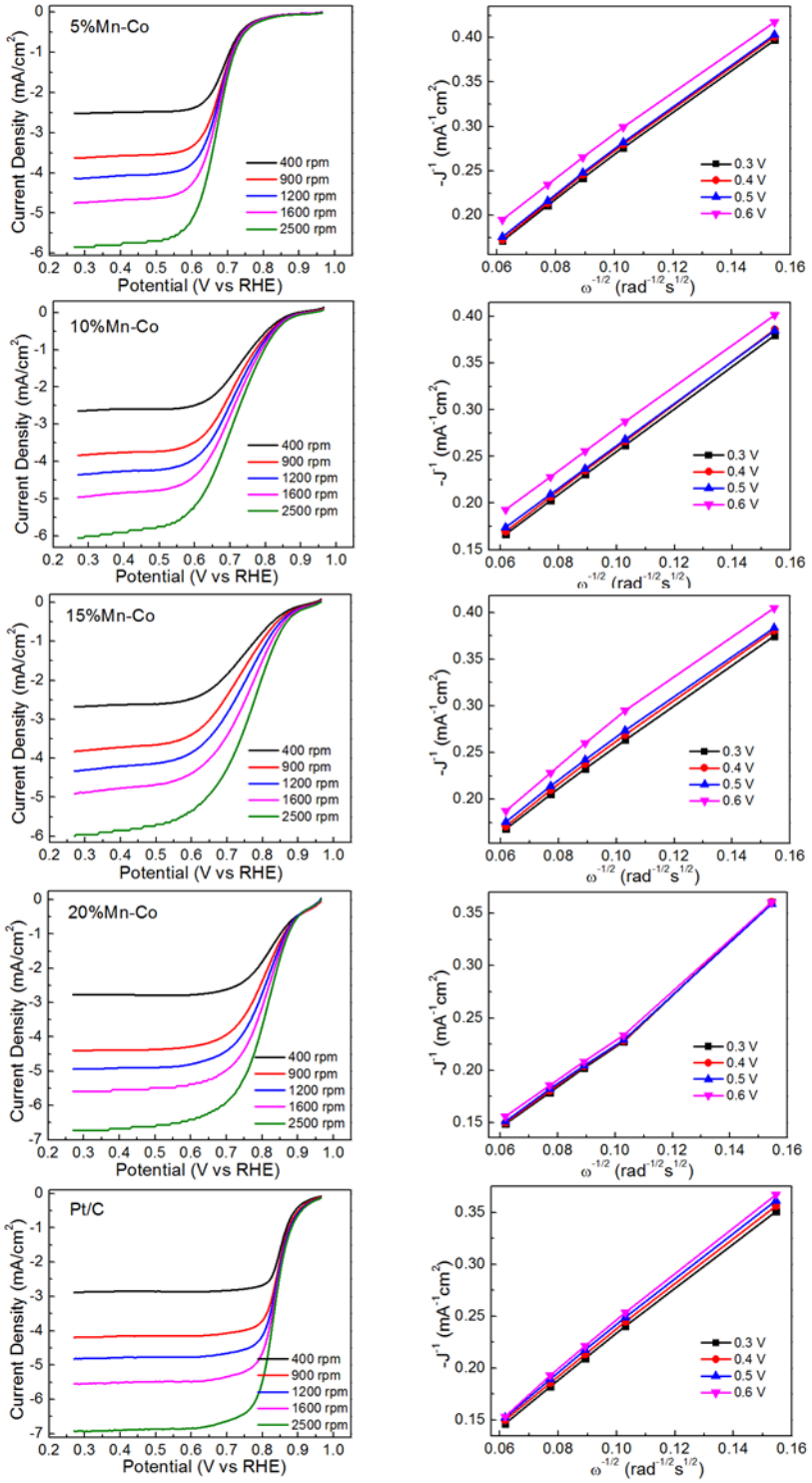

Figure 4.8 LSV curves of X%Mn-Co (X = 5, 10, 15 and 20) and 20 wt% Pt/C collected at different rotation speeds indicated with their corresponding K-L plots shown on the right.

4.3.6 OER Activities.

In addition, OER reaction activity was also measured to explore the potential of the mesoporous Ni/Mn-substituted Co_3O_4 to be used as reversible bifunctional electrocatalysts. Figure 4.9a shows the linear sweep voltammograms in anodic directions of 5%Ni-Co, 20%Mn-Co, Meso-Co and the benchmark OER catalyst, Ir/C. As illustrated by Figure 4.9a, 5%Ni-Co, 20%Mn-Co as well as Meso-Co exhibit similar onset potentials for electrochemical water oxidation at approximately 1.55 V. The 5%Ni-Co sample gives the best catalytic behavior with the highest current density and a more steep increase of the current between 1.55 and 1.65 V, showing its faster reaction rate. In terms of the activity for OER, the performance of different catalysts are usually evaluated by comparing the overpotential required for reaching a current density of 10 mA/cm^2, which is a metric for practical solar fuel synthesis.[21] The 5%Ni-Co material displays the lowest overpotential of 0.381 V to reach a current density of 10 mA/cm^2. This performance was comparable to the best reported Co-based OER catalysts under similar conditions.[27, 123] Moreover, the 5%Ni-Co system possesses better activity than the state of the art OER catalyst Ir/C at potentials beyond 1.64 V. In contrast, a slight activity decay was detected when 20% Mn was doped into the sample.

Furthermore, the Tafel plots were derived from the LSV curves in Figure 4.9a to study the kinetics of OER (Figure 4.10). The Tafel slope values were listed in Table 4.2. The overall slopes increased in the order Ir/C (72.1 mV/dec) < 5%Ni-Co (72.5) < Meso-Co (74.3) < 20%Mn-Co (114.4), showing an inverse order with the activity. The smaller Tafel slopes indicate that catalysts are more kinetically favorable towards OER reaction, leading to better activity. Several newly reported nanocast Co_3O_4 catalysts showed Tafel slopes between ~59 and 70 mV/dec when pH = 14.[124, 125] The slope values reported here were under pH 13 and the Tafel slope was found to

decrease from 96 to 59 mV/dec with pH changing from 13 to 14.[125] Thus the Tafel behavior of our catalysts is on a par with the best reported Co_3O_4 catalyst[27] and the lower Tafel slope compared with that of the nanocast Co_3O_4 demonstrates the great advantage of soft-template mesoporous materials in electrochemical applications.

To directly compare the bifunctionality of our catalysts to precious metals, LSV curves of both OER and ORR reactions of various samples are summarized in Figure 4.9b. The benchmark OER catalyst Ir/C only shows moderate activity towards ORR, with 3 mA/cm^2 current density achieved at 0.65 V, which is 180 mV more negative than 5%Ni-Co. On the other hand, the distinguished ORR catalyst Pt/C exhibits very poor OER performance compared with our mesoporous cobalt oxides without reaching 10 mA/cm^2 up to 1.665 V. Consequently, our Ni/Mn-substituted Co_3O_4 materials, especially 5%Ni-Co, stands out as a highly active bifunctional catalyst for both electrochemical oxygen reduction and water oxidation. In the past few years, similar bifunctional activities were accomplished by Co_3O_4 on carbon matrix hybrid materials.[27, 102, 106] However, the multi-step synthesis approach of composite catalysts creates difficulty for large scale industrial applications. In this work, a single-step inverse micelle synthesis without any post-treatment has been employed and has enabled us to produce batches of mesoporous materials on gram scales. As stated above, the sluggish ORR reaction kinetics of Meso-Co can be overcome by simply doping Ni or Mn into its structure at the beginning of the wet chemical synthesis. Meanwhile competitive OER performance was maintained and further enhanced.

The charge transport efficiency of OER was appraised by EIS spectroscopy under OER reaction conditions (Figure 4.9c). Lower values of R_{ct}, typically reflected from smaller features in the Nyquist plots, usually correlate with better catalytic behavior. In general, the trend of obtained R_{ct} values match the OER activity trend presented in Figure 4.9a. One exception is 20%Mn-Co

which demonstrates lower activity than Meso-Co even though Mn doping appears to have facilitated improved electron transfer. Stabilities of these catalysts were evaluated under controlled current electrolysis at 10 mA/cm^2 by the chronopotentiometry technique. The potential window was set between 1.465 and 1.965 V. As shown in Figure 4.9d, 5%Ni-Co demonstrates a negligible positive shift of the potential during 24 hours of continuous electrolysis, implying its long time stability. Interestingly, 20%Mn-Co displayed a potential increase in the first 6 hours. The potential was then slowly decreased to approach its initial value. This could be due to the surface passivation of the catalyst under oxidizing conditions.[126] Both catalysts display superior durability to Ir/C, which exhibits severe polarization in prolonged use. After the chronopotentiometry tests, the catalysts were carefully removed from the electrode and characterized by HR-TEM (Figure 4.9e and f). The mesopores formed by the intraparticle voids and clear lattice fringes indexed to Co_3O_4 crystalline structure can be observed, suggesting good structural and crystal phase stability of the materials.

Lastly, OER tests were performed on the complete group of Ni/Mn-substituted Co_3O_4 with different Ni and Mn doping concentrations and results are summarized in Table 4.2. Briefly, Ni-doped Co_3O_4 showed very close OER behavior, which is similar to the activity trend observed in their ORR performances. Unlike their ORR activity behavior, however, Mn doping did not lead to an obvious change in the OER activity of Meso-Co when the targeted doping is smaller than 15%. However, 20%Mn-Co showed lower activity than Meso-Co as discussed above, suggesting that too much Mn in the sample inhibited the OER reaction. This finding is in line with another literature report.[102]

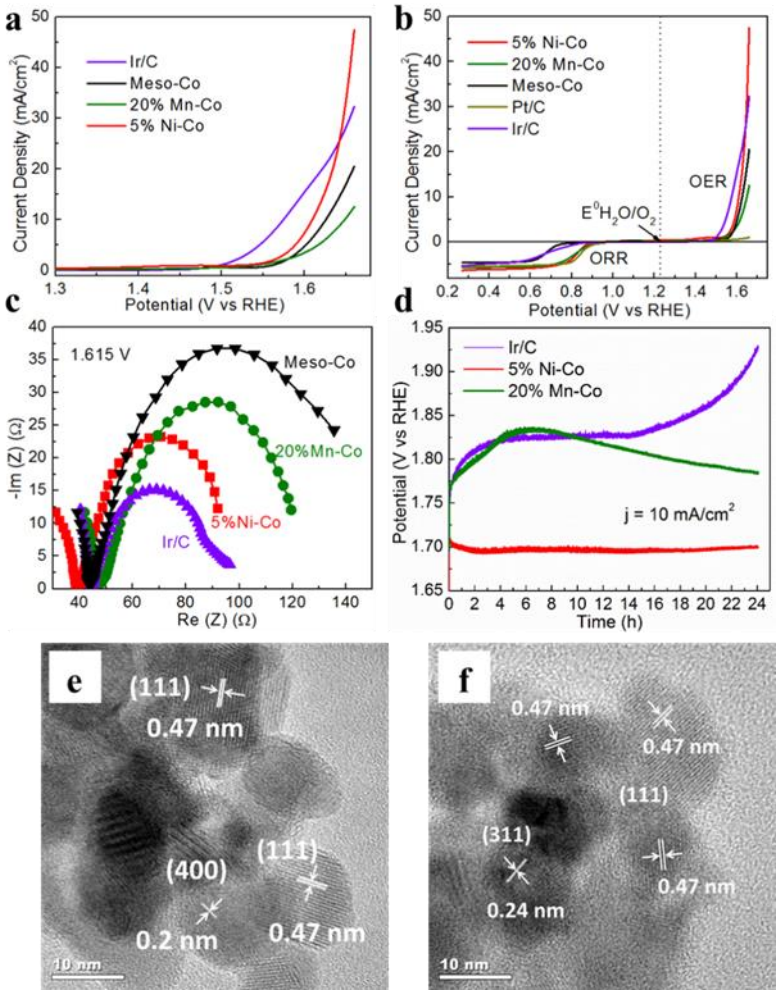

Figure 4.9 OER activities: (a) LSV curves of 5%Ni-Co, 20%Mn-Co, Meso-Co and Ir/C in O_2-saturated 0.1 M KOH solution at a rotation rate of 1600 rpm and a sweep rate of 5 mV/s. (b) Oxygen electrode bifunctional activities studied by LSV technique for both ORR and OER of 5%Ni-Co, 20%Mn-Co, Meso-Co, Pt/C and Ir/C catalysts. (c) Nyquist plots obtained from impedance measurements in O_2-saturated 0.1 M KOH at 1.615 V of 5%Ni-Co, 20%Mn-Co, Meso-Co and Ir/C catalysts. (d) Chronopotentiometric responses of 5%Ni-Co, 20%Mn-Co and Ir/C catalysts in O_2-saturated 0.1 M KOH under a constant current density of 10 mA/cm^2 and a rotation rate of 1600 rpm. HR-TEM images of (e) 5%Ni-Co, and (f) 20%Mn-Co after OER stability tests, respectively.

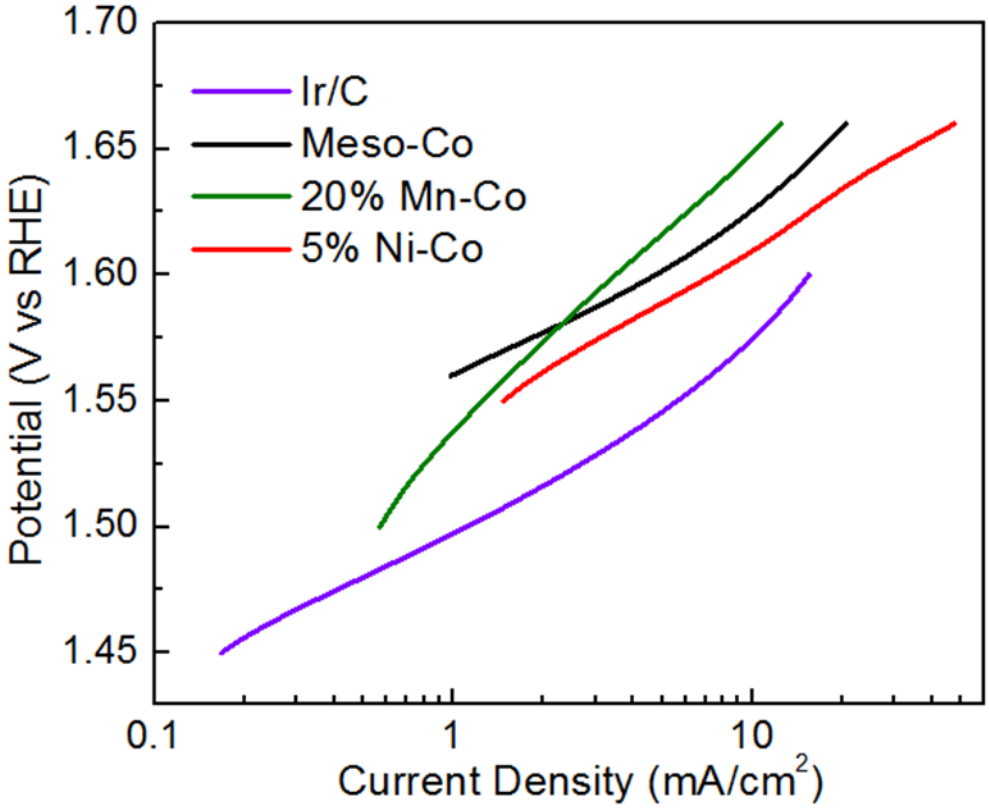

Figure 4.10 Tafel plots derived from LSV curves in **Figure 4.9a**.

4.4 Discussion

As stated previously, Co^{3+} is usually considered as the active site for OER, while Co^{2+} is believed to play a significant role in catalyzing ORR. CV tests under inert atmosphere are useful techniques to study the surface redox activities of Co^{2+} and Co^{3+} cations in Co_3O_4. Figure 4.11 displays the CV voltammograms in Ar-saturated 0.1 M KOH solution between 0.51 and 1.61 V. Multiple anodic (oxidation process) and cathodic (reduction process) peaks were observed. As shown in Figure 4.11, the redox couple I_a/I_c in the range of ~1.07-1.1 V can be assigned to the transformation between Co(II) and Co(III), while another pair of redox peaks II_a/II_c at ~1.24-1.54 V can be ascribed to the Co(III)/Co(IV) redox couple. The involved reactions in basic media are shown below:[113, 120, 127]

I_a/I_c, $\quad Co_3O_4 + OH^- + H_2O \leftrightarrow 3CoOOH + e^-$

II_a/II_c, $\quad CoOOH + OH^- \leftrightarrow CoO_2 + H_2O + e^-$

Besides these two redox couples, a small shoulder peak at ca. 1.28-1.42 V corresponding to the oxidation of Ni(II) to Ni(III) was also detected (Figure 4.11a), suggesting the doped Ni mainly exists as Ni^{2+}.[120] This peak becomes more evident and overlaps with the II_a peak when the doping concentration of Ni is larger than 15%, thus forming a more broad and intense anodic II_a peak. On the other hand, Figure 4.11b displays small shoulder peaks for the redox reactions of Mn related phases. The anodic peaks in the range of ca. 0.8-1.1 V and ca. 1.2-1.4 V can be attributed to the oxidation of Mn(II) to Mn(III) and Mn(III) to Mn(IV), respectively,[120] which indicate the coexistence of Mn^{2+} and Mn^{3+}. The rapid increase of the current density at potentials right after peak II_a is due to electrochemical oxygen evolution. Therefore, the oxidation of surface Co^{3+} to Co^{4+} is crucial for OER activity. After Ni was doped into Meso-Co, the anodic peak position of

Co(III)/Co(IV) was shifted to an lower potential as demonstrated in Figure 4.11a, while this kind of negative shift was not seen for the Mn-substituted Co_3O_4 series. This indicates Ni doping facilitates the oxidation of Co^{3+} to Co^{4+}, however Mn does not contribute to this oxidation process. These observations can explain the OER activity trend seen in Figure 4.9a: 5%Ni-Co > Meso-Co > 20%Mn-Co. Moreover, the II_a peak intensity of 20%Mn-Co is much lower than those of other Mn-substituted Co_3O_4 catalysts (Figure 4.11b). This explains the weakest OER activity of the 20%Mn-Co material among Mn-substituted series. Conversely, for ORR, the reverse reaction of OER, Co^{2+} is considered as the active site.[105] However, according to our CV voltammograms in Figure 4.11, I_a and I_c peaks associated with Co^{2+} in the Co_3O_4 spinel structure were weakened upon Ni and Mn incorporation. The ORR performance of Meso-Co was largely promoted by Ni or Mn doping. Therefore, the ORR activities cannot be simply correlated with surface Co^{2+} sites. Other structural parameters like surface area and oxygen deficiency need to be taken into consideration for better understanding of the ORR activity which will be discussed later.

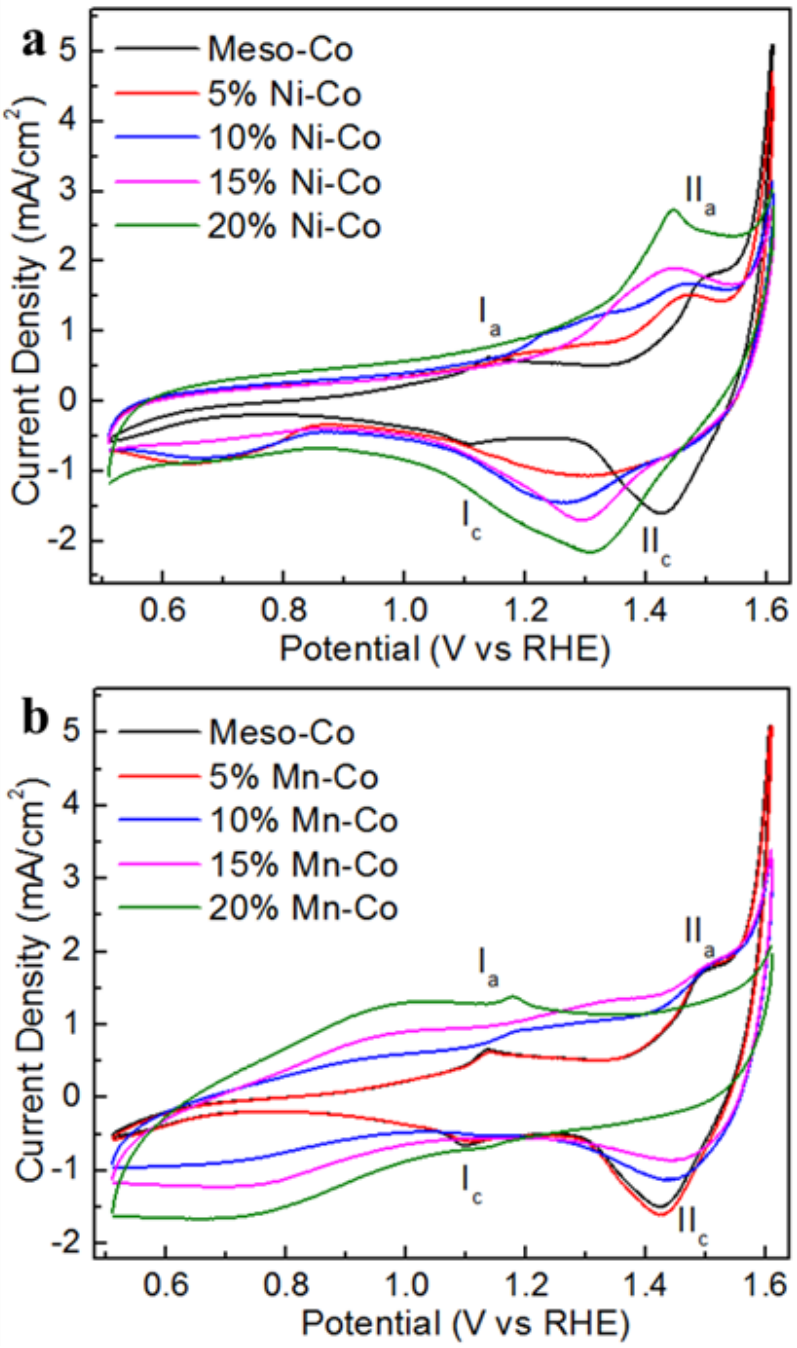

Figure 4.11 Surface redox properties: CV analyses of (a) X%Ni-Co (X = 5, 10, 15, and 20), Meso-Co, and (b) X%Mn-Co (X = 5, 10, 15, and 20), Meso-Co catalysts. All tests were performed in Ar-saturated 0.1 M KOH solution at a sweep rate of 25 mV/s. Multiple cycles were recorded until a reproducible scan was obtained.

To understand how the Co(III)/Co(IV) redox couple affects OER reactions, we need to first take a closer look at the reaction mechanism of OER. According to the mechanism proposed by several research groups,[123, 128, 129] the reaction starts with the adsorption of OH^- anions and the formation of the first intermediate A-OH_{ads} (A stands for the active sites on the anode surface). Subsequently the formed A-OH_{ads} further reacts with OH^- anions in the electrolyte and undergoes a series of transformation steps including the generation of A-O_{ads}, A-OOH_{ads} and the deprotonation of A-OOH_{ads} to produce O_2. The rate-determining step (rds) of OER is generally believed to be related to the Tafel slope.[108, 127] The Tafel slopes of our catalysts (see Table 4.2 and Figure 4.10) are within the range that the rearrangement of the first intermediate A-OH_{ads} is regarded as the rds.[129] When surface Co^{3+} is oxidized to Co^{4+}, the electrophilicity of the intermediate is enhanced, thus enabling reaction with the nucleophilic species OH^- and facilitating the formation of A-OOH_{ads}. In addition, Co^{4+} can also boost the deprotonation of A-OOH_{ads} via an electron-withdrawing inductive effect to form the final product O_2.[108, 123, 128] From the perspective of Lewis acid-base interactions, Co^{4+} as a high valence state cation makes the anode surface more acidic, which helps the activation of H_2O molecules (Lewis base).[123] As previously discussed, Ni doping is a better choice for improving the OER performance of Meso-Co than Mn. This can be further explained from two aspects. First, Bell et al. claimed that the electronegativity of transition metals could have an influence on the oxidation of Co^{3+} in Co_3O_4 to Co^{4+}.[128] The greater electronegativity of Ni (1.91) than Mn (1.55) makes it a powerful electron sink to promote the oxidation step from Co^{3+} to Co^{4+}, contributing to higher OER activity. Secondly, the partial replacement of cobalt cations by Ni^{2+} can enlarge the Co^{3+}-O bond length, thereby assisting the OH^- anions to adsorb onto Co^{3+} and oxidize to Co^{4+}. Similar improvement of OER performance due to the Co^{3+}-O bond distance expansion was reported for $Zn_xCo_{3-x}O_4$ nanoarrays.[108] The larger

extent of Co^{3+}-O bond distortion caused by Ni incorporation compared to Mn was further confirmed by Raman analyses. Since it is relatively difficult for Mn to go into the Co_3O_4 lattice and in order to make a fair comparison, Figure 4.12 displays the Raman spectra of 5%Ni-Co and 10%Mn-Co. The actual Ni/Mn atomic percentages have been determined by EDS under TEM to be similar, 12.1% and 11.7% as shown in Table 4.1. Five characteristic bands of Co_3O_4 lattice at 192, 477, 521, 616, and 680 cm^{-1} were detected, corresponding to F_{2g}, E_g, F_{2g}, F_{2g}, and A_{1g} vibrational modes.[130, 131] The high frequency band at 680 cm^{-1} can be assigned to a vibration involving the motion of oxygen atoms inside the octahedral units, where Co^{3+} mainly exists.[132-134] Upon incorporation of Ni, the A_{1g} mode broadened and the wavenumber shifted towards the lower energy side, suggesting a tensile stress has been introduced in the Co_3O_4 matrix by external Ni dopant. This kind of change in Raman band width and wavenumber has been reported in different doping systems.[133, 135, 136] On the other hand, very few changes in the Raman bands were detected in 10%Mn-Co compared to Meso-Co (Figure 4.12), indicating that Ni has a stronger ability to induce Co_3O_4 lattice disorder than Mn. As a result, the Co(III)-O bond strength in Ni-substituted Co_3O_4 is weakened and Co^{3+} can be more readily oxidized to Co^{4+}, leading to better OER performance.

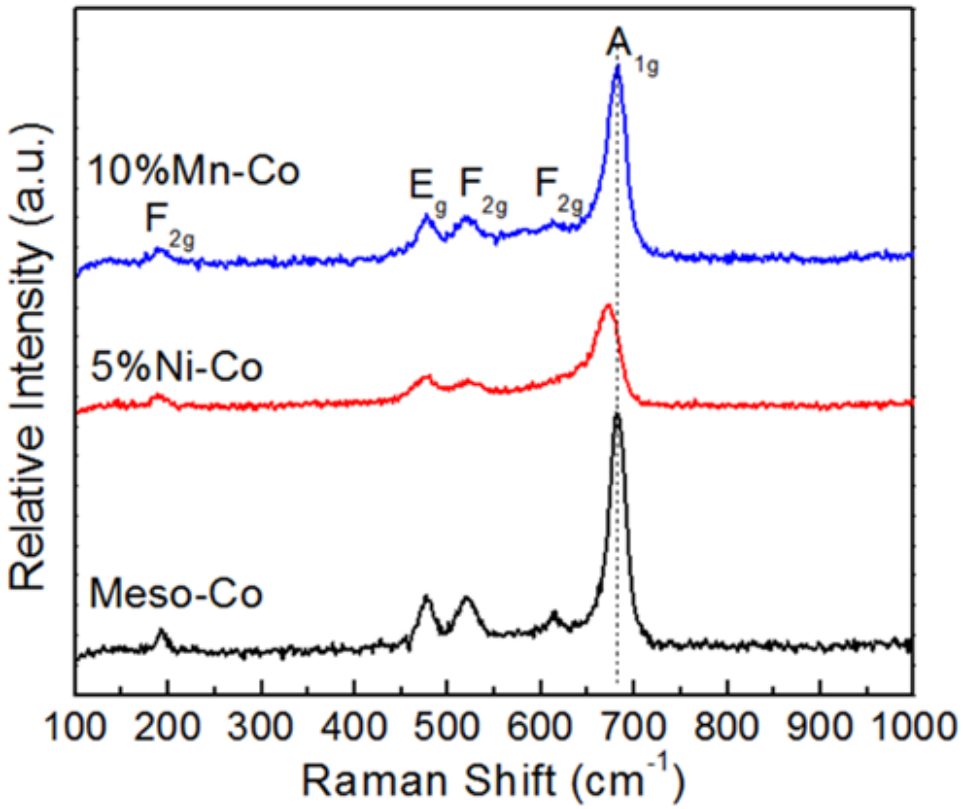

Figure 4.12 Raman scattering spectra of 5%Ni-Co, 10%Mn-Co and Meso-Co.

From the preceding discussion, improved ORR activity through Ni and Mn substitution cannot be directly correlated with the surface Co^{2+} population. A brief understanding of the ORR reaction pathway is required to investigate the intrinsic active sites. ORR could proceed via a direct four-electron pathway or an indirect two-electron pathway. As summarized in Table 4.2, the electron transfer number n for Meso-Co is 3.6, suggesting the existence of a 2e pathway. In this case, the adsorbed O_2 is first reduced to peroxide ion, then the generated peroxide is further reduced to hydroxide ion or undergoes a chemical disproportionation reaction. After doping with Ni or Mn, the n value approaches the direct 4e pathway without peroxide generation. In both cases, the reaction starts with adsorption and partial dissociation of O_2, which is considered as the rate-determining step of ORR.[119, 137, 138] From this point of view, a good ORR catalyst should have good O_2 adsorption affinity and sufficient oxygen vacancies. The strong binding between adsorbed O_2 and surface vacancy site can trigger the elongation of the O-O bond, thus lowering the activation energy and facilitating the reduction of O_2. To characterize the O_2 adsorption ability and surface defects of the catalysts, O_2-TPD tests were performed on 5%Ni-Co and 20%Mn-Co, the two best ORR catalysts, as well as Meso-Co for comparison in Figure 4.13a. Usually, the oxygen desorption peaks below 500 °C can be attributed to chemisorbed oxygen on surface defects, while the peaks appearing after 500 °C are due to desorption of lattice oxygen.[112, 119] No discernible features below 500 °C can be observed in Meso-Co, while both 5%Ni-Co and 20%Mn-Co displayed a well-defined desorption peak (marked by arrows in Figure 4.13a). This indicates the enriched surface oxygen vacancies in Ni and Mn-substituted Co_3O_4. Moreover, 5%Ni-Co desorbs chemisorbed oxygen at a higher temperature (~400 °C) than 20%Mn-Co (~300 °C), suggesting this material has stronger oxygen binding ability than 20%Mn-Co. The O_2-TPD results match perfectly with the XPS analyses. Figure 4.13b shows the deconvoluted O 1s spectra with the

quantified results listed in Table 4.3. The high oxygen vacancy concentrations on 5%Ni-Co and 20%Mn-Co were evidenced by their smaller amount of lattice oxygen (O_L) and more intense peaks of hydroxyl (O_{OH}) and chemisorbed water (O_{mw}) than Meso-Co. Furthermore, the presence of oxygen vacancies can also be expected from lattice expansion as indicated by the peak shift in PXRD and Raman results (Figure 4.2a, 4.4a and 4.12).[136, 137] Consequently, Ni/Mn-substituted Co_3O_4 possesses much higher ORR activities than Meso-Co by showing more positive onset potentials and larger current densities (Figure 4.5, 4.7 and Table 4.2). This finding is also in agreement with recent published literature that more surface exposed Co^{2+} ions lead to better ORR activity.[105] Given the charge neutrality, more Co^{2+} in the Co_3O_4 spinel structure corresponds to less lattice oxygen. However, this hypothesis only applies to pure Co_3O_4 without foreign cations. In our case, due to the presence of Ni or Mn cations in the structure, there is no direct relationship between Co^{2+} population and oxygen vacancies. So more precisely speaking, the enhancement of ORR activity should be attributed to a high fraction of surface defect sites.

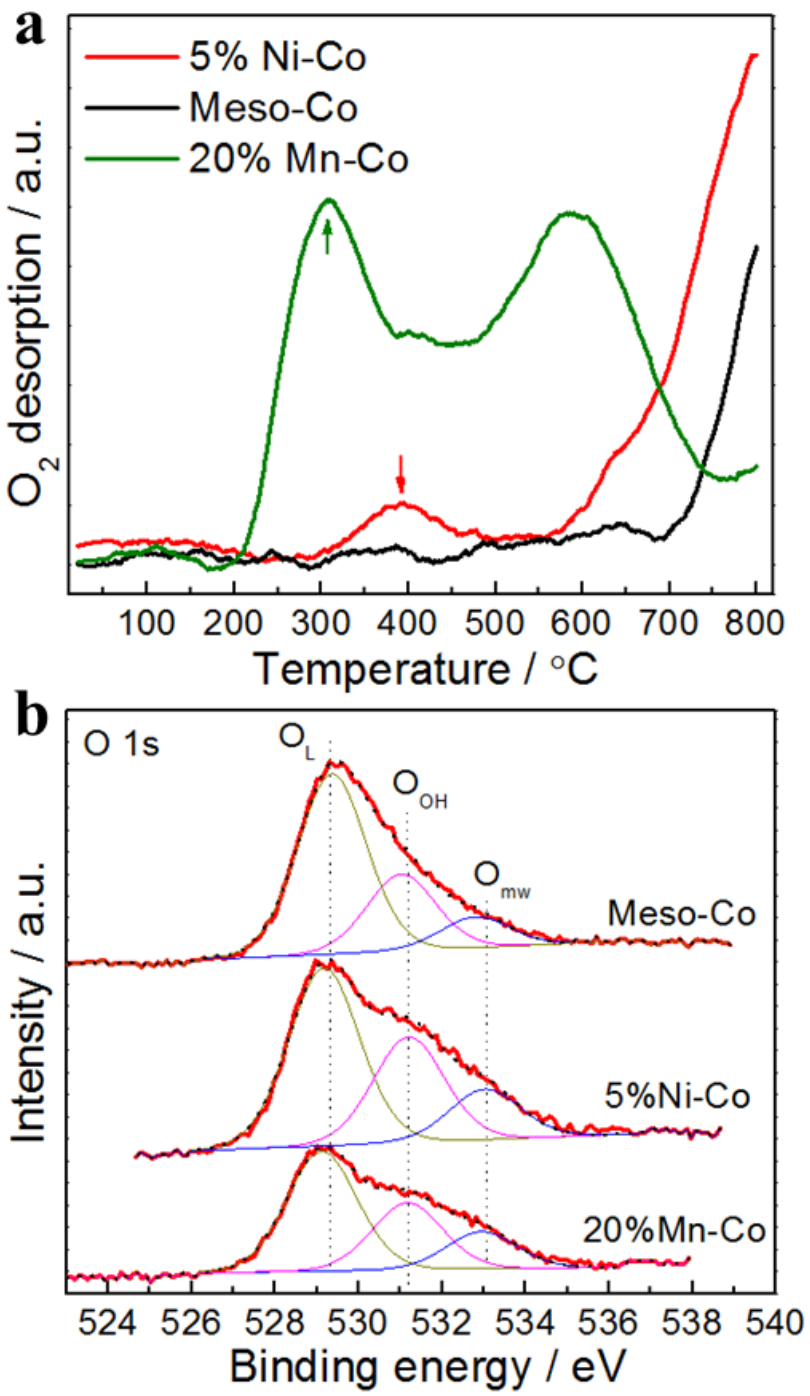

Figure 4.13 (a) O_2-TPD profiles, and (b) Deconvoluted O 1s spectra from XPS analyses of Meso-Co, 5%Ni-Co and 20%Mn-Co. O 1s peaks were deconvoluted into three major contributions: lattice oxygen (O_L), surface hydroxyl group (O_{OH}), and adsorbed molecular water (O_{mw}).

Table 4.3 Summary of Binding Energy (BE) and Area Percentages of Different Oxygen Components.

Material	O_L		O_{OH}		O_{mw}	
	BE (eV)	Area (%)	BE (eV)	Area (%)	BE (eV)	Area (%)
Meso-Co	529.4	62.7	531.0	26.6	532.8	10.7
5%Ni-Co	529.2	53.3	531.2	31.6	533.0	15.1
20%Mn-Co	529.1	53.4	531.2	30.0	532.9	16.6

Besides the promotion effect of abundant oxygen vacancies and high activity of surface Co^{3+} to Co^{4+} transformation, surface area should also have a great impact on the ORR and OER activities since both reactions are surface sensitive. According to previously published work, high surface area meso-structured Pt thin films exhibited higher activity and stability for ORR than the commercial Pt/C catalyst.[139] Similarly, mesoporous Co_3O_4 was reported to have superior activity to the conventional Co_3O_4 nanoparticles.[110] In this study, ORR activities have been largely improved after Ni or Mn is incorporated into the Co_3O_4 mesoporous structure (Figure 4.5, 4.7 and Table 4.2). The doped Co_3O_4 mesoporous structures exhibit larger surface areas. As summarized in Table 4.1, the surface areas of Ni-incorporated Co_3O_4 are almost on the same level (~150-160 m^2/g) regardless of the doping concentrations (5, 10, 15, and 20 mol%) but they are much larger than that of Meso-Co (109 m^2/g). This also explains the ORR activity trend that all Ni-substituted Co_3O_4 catalysts show comparable ORR performance with the onset potentials at ca. 0.87 V, which are much more positive than 0.75 V for Meso-Co (Figure 4.5 and Table 4.2). For the Mn-substituted Co_3O_4 series, the continuously increased surface areas from 127 to 199 m^2/g with more Mn incorporation into the Co_3O_4 also accounts for the higher activities (Figure 4.7, Table 4.1 and 4.2). Accordingly, the desired potential for a current density of -3 mA/cm^2 follows the order of Meso-Co (0.66 V) = 5%Mn-Co (0.66) < 10%Mn-Co (0.69) < 15%Mn-Co (0.73) < 20%Mn-Co (0.81). Therefore, the critical role of surface area in catalyzing ORR is confirmed. The high surface areas of our cobalt based mesoporous materials enable efficient electron-mass transport and supply more accessible active sites. Their well-developed porous channels are able to benefit the diffusion of reactants, the penetration of electrolytes and the release of products formed, thus maximizing the utilization of catalytic active sites. Moreover, the highly interconnected porous network of mesoporous catalysts were reported to display better stability by retaining its original structure

under harsh electrocatalytic conditions.[110] On the other hand, no promoted activity with increasing surface area was detected for OER, which suggests the oxidation process of Co^{3+} to Co^{4+} may be predominant over the surface areas in determining the OER activity. Therefore, excellent surface redox activity, abundant oxygen defects and large surface area all contributed to exceptional ORR and OER activities of our catalysts, making them promising candidates for potential applications of solar water splitting, rechargeable metal air batteries and fuel cells.

4.5 Conclusions

In summary, mesoporous cobalt oxide as well as Ni and Mn substituted cobaltite has been successfully synthesized by a one-step wet-chemical method. The obtained materials are formed by monodispersed nanoparticle aggregation with mesopores developed in between the nanoparticle voids. Their electrocatalytic performances for both ORR and OER were systematically investigated by CV, RDEV, and EIS methods. The 5%Ni-Co sample exhibited the best activity with an overpotential of 399 mV for ORR (at 3 mA/cm^2) and 381 mV (at 10 mA/cm^2) for OER, which are on a par with the state of the art Pt/C (389 mV for ORR) and Ir/C (346 mV for OER) catalysts. Negligible catalytic activity decay was observed for both reactions over a 24 hour time period. Their surface compositions and redox properties were characterized by CV, Raman, XPS and O_2-TPD analyses, and correlated with the activity performance. The enhancement of the ORR activity with Ni and Mn doping was believed to relate to the increase of surface oxygen defects and surface areas, while the improvement of the OER performance was found to result from the facilitation of the oxidation of surface Co^{3+} cations to Co^{4+}. This is the first systematic study to probe surface active sites for both OER and ORR through partial cation substitution and may provide insight to guide future catalyst synthesis and applications for many related fields.

FUTURE WORK

In this thesis, mesoporous cobalt oxides with controlled porosity have been synthesized and used for low temperature carbon monoxide oxidation reaction. This material has enriched surface oxygen vacancies and very good lattice oxygen mobility. Therefore, this system should have a great potential in catalyzing other oxidation reactions such as hydrocarbon oxidation and volatile organic compound oxidation. Moreover, this material could be used to activate C-H bonds and produce value added products. One example could be ethane oxidative dehydrogenation to ethylene. To selectively oxidize ethane, the catalyst needs to be modified to reduce its oxidation ability in order to prevent over-oxidation. Mild oxidants like CO_2 instead of O_2 can also be used. Another direction would be increasing the hydrophobicity of the material. This could be realized by coupling the mesoporous material with hydrophobic polymers to improve its moisture resistance ability.

In the second part, in-situ coating of mesoporous metal oxides on cordierite substrates has been discussed. N_2 sorption and TEM characterization should be completed. To further test the potential of these materials in exhaust after-treatment application, propane combustion reactions should be carried out. Besides, attempts could be made to scale up the synthesis and get rid of the remaining powder in the reactor, moving it one step closer to commercialization. Furthermore, extending this coating method to other substrates and using these materials in gas/liquid separations are worth trying.

In the electrochemical study, substituted mesoporous cobalt oxide was used as a bifunctional catalyst for oxygen reduction and oxygen evolution reactions. The next stage of the research could focus on using this material in other electrochemical reactions including methane

activation, methanol oxidation, and hydrogen evolution reactions. Ni-doped cobalt oxide material is well known for its good conductivity. By combining electrochemical results with gas phase characterization and reactions, other activity related properties (besides conductivity) could be fully investigated. Additionally, the materials can be coupled with conductive substrates to further promote the conductivity.

REFERENCES

1. T. Jiang, A. S. Poyraz, A. Iyer, Y. Zhang, Z. Luo, W. Zhong, R. Miao, A. M. El-Sawy, C. J. Guild and Y. Sun, *J. Phys. Chem. C*, 2015.
2. J. Rosen, G. S. Hutchings and F. Jiao, *J. Catal.*, 2014, **310**, 2-9.
3. G. J. de AA Soler-Illia, E. L. Crepaldi, D. Grosso and C. Sanchez, *Curr. Opin. Colloid Interface Sci.*, 2003, **8**, 109-126.
4. S. Taylor and C. Rhodes, *Catal. Lett.*, 2005, **101**, 31-33.
5. P. Thormählen, M. Skoglundh, E. Fridell and B. Andersson, *J. Catal.*, 1999, **188**, 300-310.
6. M. Cargnello, C. Gentilini, T. Montini, E. Fonda, S. Mehraeen, M. Chi, M. Herrera-Collado, N. D. Browning, S. Polizzi and L. Pasquato, *Chem. Mater.*, 2010, **22**, 4335-4345.
7. M. Haruta, T. Kobayashi, H. Sano and N. Yamada, *Chem. Lett.*, 1987, 405-408.
8. X. Xie, Y. Li, Z.-Q. Liu, M. Haruta and W. Shen, *Nature*, 2009, **458**, 746-749.
9. J. W. Saalfrank and W. F. Maier, *Angew. Chem. Int. Ed.*, 2004, **43**, 2028-2031.
10. Y. Guo, Z. Ren, W. Xiao, C. Liu, H. Sharma, H. Gao, A. Mhadeshwar and P.-X. Gao, *Nano Energy*, 2013, **2**, 873-881.
11. S.-Y. Chen, W. Song, H.-J. Lin, S. Wang, S. Biswas, M. Mollahosseini, C.-H. Kuo, P.-X. Gao and S. L. Suib, *ACS Appl. Mater. Interfaces*, 2016, **8**, 7834-7842.
12. A. Bueno-López, D. Lozano-Castelló, I. Such-Basáñez, J. García-Cortés, M. Illán-Gómez and C. S.-M. De Lecea, *Appl. Catal., B*, 2005, **58**, 1-7.
13. J. L. Williams, *Catal. Today*, 2001, **69**, 3-9.
14. A. S. Aricò, P. Bruce, B. Scrosati, J.-M. Tarascon and W. Van Schalkwijk, *Nat. Mater.*, 2005, **4**, 366-377.
15. Y. G. Guo, J. S. Hu and L. J. Wan, *Adv. Mater.*, 2008, **20**, 2878-2887.
16. Q. Zhang, E. Uchaker, S. L. Candelaria and G. Cao, *Chem. Soc. Rev.*, 2013, **42**, 3127-3171.
17. M. Winter and R. J. Brodd, *Chem. Rev.*, 2004, **104**, 4245-4270.

18. M. W. Kanan and D. G. Nocera, *Science*, 2008, **321**, 1072-1075.

19. M. G. Walter, E. L. Warren, J. R. McKone, S. W. Boettcher, Q. Mi, E. A. Santori and N. S. Lewis, *Chem. Rev.*, 2010, **110**, 6446-6473.

20. H. Wang, Y. Yang, Y. Liang, G. Zheng, Y. Li, Y. Cui and H. Dai, *Energy Environ. Sci.*, 2012, **5**, 7931-7935.

21. Y. Gorlin and T. F. Jaramillo, *J. Am. Chem. Soc.*, 2010, **132**, 13612-13614.

22. P. Strasser, S. Koh, T. Anniyev, J. Greeley, K. More, C. Yu, Z. Liu, S. Kaya, D. Nordlund and H. Ogasawara, *Nat. Chem.*, 2010, **2**, 454-460.

23. Y. Lee, J. Suntivich, K. J. May, E. E. Perry and Y. Shao-Horn, *J. Phys. Chem. Lett.*, 2012, **3**, 399-404.

24. Y.-C. Lu, Z. Xu, H. A. Gasteiger, S. Chen, K. Hamad-Schifferli and Y. Shao-Horn, *J. Am. Chem. Soc.*, 2010, **132**, 12170-12171.

25. Z. Chen, A. Yu, D. Higgins, H. Li, H. Wang and Z. Chen, *Nano Lett.*, 2012, **12**, 1946-1952.

26. S. Park, Y. Shao, J. Liu and Y. Wang, *Energy Environ. Sci.*, 2012, **5**, 9331-9344.

27. Y. Liang, Y. Li, H. Wang, J. Zhou, J. Wang, T. Regier and H. Dai, *Nat. Mater.*, 2011, **10**, 780-786.

28. Y. Meng, W. Song, H. Huang, Z. Ren, S.-Y. Chen and S. L. Suib, *J. Am. Chem. Soc.*, 2014, **136**, 11452-11464.

29. H. Zhu, S. Zhang, Y.-X. Huang, L. Wu and S. Sun, *Nano Lett.*, 2013, **13**, 2947-2951.

30. J. Suntivich, K. J. May, H. A. Gasteiger, J. B. Goodenough and Y. Shao-Horn, *Science*, 2011, **334**, 1383-1385.

31. K. J. May, C. E. Carlton, K. A. Stoerzinger, M. Risch, J. Suntivich, Y.-L. Lee, A. Grimaud and Y. Shao-Horn, *J. Phys. Chem. Lett.*, 2012, **3**, 3264-3270.

32. A. Zhao, J. Masa, W. Xia, A. Maljusch, M.-G. Willinger, G. Clavel, K. Xie, R. Schlögl, W. Schuhmann and M. Muhler, *J. Am. Chem. Soc.*, 2014, **136**, 7551-7554.

33. Z. Ren, Y. Guo, Z. Zhang, C. Liu and P.-X. Gao, *J. Mater. Chem. A*, 2013, **1**, 9897-9906.

34. C.-H. Kuo, W. Li, W. Song, Z. Luo, A. S. Poyraz, Y. Guo, A. W. Ma, S. L. Suib and J. He, *ACS Appl. Mater. Interfaces*, 2014, **6**, 11311-11317.

35. L. R. Pahalagedara, A. S. Poyraz, W. Song, C.-H. Kuo, M. N. Pahalagedara, Y.-T. Meng and S. L. Suib, *Chem. Mater.*, 2014, **26**, 6613-6621.

36. Z. Ren, V. Botu, S. Wang, Y. Meng, W. Song, Y. Guo, R. Ramprasad, S. L. Suib and P. X. Gao, *Angew. Chem. Int. Ed.*, 2014, **53**, 7223-7227.

37. Z. Ren, Z. Wu, W. Song, W. Xiao, Y. Guo, J. Ding, S. L. Suib and P.-X. Gao, *Appl. Catal., B*, 2016, **180**, 150-160.

38. C. Wang, H. Yin, S. Dai and S. Sun, *Chem. Mater.*, 2010, **22**, 3277-3282.

39. C.-H. Chen, E. C. Njagi, S.-P. Sun, H. Genuino, B. Hu and S. L. Suib, *Chem. Mater.*, 2010, **22**, 3313-3315.

40. X.-D. Hou, Y.-Z. Wang and Y.-X. Zhao, *Catal. Lett.*, 2008, **123**, 321-326.

41. C. Kresge, M. Leonowicz, W. Roth, J. Vartuli and J. Beck, *Nature*, 1992, **359**, 710-712.

42. A. S. Poyraz, S. Biswas, H. C. Genuino, S. Dharmarathna, C. H. Kuo and S. L. Suib, *ChemCatChem*, 2013, **5**, 920-930.

43. D. E. De Vos, M. Dams, B. F. Sels and P. A. Jacobs, *Chem. Rev.*, 2002, **102**, 3615-3640.

44. Z. Wu and D. Zhao, *Chem. Commun.*, 2011, **47**, 3332-3338.

45. A. K. Sinha and K. Suzuki, *Angew. Chem. Int. Ed.*, 2005, **44**, 271-273.

46. M. Vettraino, M. Trudeau and D. Antonelli, *Adv. Mater.*, 2000, **12**, 337-341.

47. S. W. Boettcher, J. Fan, C.-K. Tsung, Q. Shi and G. D. Stucky, *Acc. Chem. Res.*, 2007, **40**, 784-792.

48. A. S. Poyraz, C.-H. Kuo, S. Biswas, C. K. King'ondu and S. L. Suib, *Nature Commun.*, 2013, **4**.

49. D. Grosso, F. Cagnol, G. d. A. Soler-Illia, E. L. Crepaldi, H. Amenitsch, A. Brunet-Bruneau, A. Bourgeois and C. Sanchez, *Adv. Funct. Mater.*, 2004, **14**, 309-322.

50. A. S. Poyraz, C.-H. Kuo, E. Kim, Y. Meng, M. S. I. Seraji and S. L. Suib, *Chem. Mater.*, 2014.

51. E. C. Njagi, C.-H. Chen, H. Genuino, H. Galindo, H. Huang and S. L. Suib, *Appl. Catal., B*, 2010, **99**, 103-110.

52. C.-H. Kuo, W. Li, W. Song, Z. Luo, A. Poyraz, Y. Guo, A. W. Ma, S. L. Suib and J. He, *ACS Appl. Mater. Interfaces*, 2014.

53. J.-Y. Luo, M. Meng, X. Li, X.-G. Li, Y.-Q. Zha, T.-D. Hu, Y.-N. Xie and J. Zhang, *J. Catal.*, 2008, **254**, 310-324.

54. C.-W. Tang, C.-C. Kuo, M.-C. Kuo, C.-B. Wang and S.-H. Chien, *Appl. Catal., A*, 2006, **309**, 37-43.

55. NIST XPS Database, X-ray Photoelectron Spectroscopy Database 20, version 3.0.

56. M. M. Natile and A. Glisenti, *Chem. Mater.*, 2002, **14**, 3090-3099.

57. Y. Ding, L. Zhu, A. Huang, X. Zhao, X. Zhang and H. Tang, *Catal. Sci. Technol.*, 2012, **2**, 1977-1984.

58. B. Ernst, A. Bensaddik, L. Hilaire, P. Chaumette and A. Kiennemann, *Catal. Today*, 1998, **39**, 329-341.

59. W. Shan, W. Shen and C. Li, *Chem. Mater.*, 2003, **15**, 4761-4767.

60. A. Gupta, M. Hegde, K. Priolkar, U. Waghmare, P. Sarode and S. Emura, *Chem. Mater.*, 2009, **21**, 5836-5847.

61. P. Arnoldy and J. A. Moulijn, *J. Catal.*, 1985, **93**, 38-54.

62. C.-B. Wang, C.-W. Tang, S.-J. Gau and S.-H. Chien, *Catal. Lett.*, 2005, **101**, 59-63.

63. M. Kang, M. W. Song and C. H. Lee, *Appl. Catal., A*, 2003, **251**, 143-156.

64. L. Liotta, G. Di Carlo, G. Pantaleo, A. Venezia and G. Deganello, *Appl. Catal., B*, 2006, **66**, 217-227.

65. L. Xue, C. Zhang, H. He and Y. Teraoka, *Appl. Catal., B*, 2007, **75**, 167-174.

66. L. Spadaro, F. Arena, M. Granados, M. Ojeda, J. Fierro and F. Frusteri, *J. Catal.*, 2005, **234**, 451-462.

67. Z. Fei, S. He, L. Li, W. Ji and C.-T. Au, *Chem. Commun.*, 2012, **48**, 853-855.

68. Y.-Z. Wang, Y.-X. Zhao, C.-G. Gao and D.-S. Liu, *Catal. Lett.*, 2008, **125**, 134-138.

69. Q. Liu, L.-C. Wang, M. Chen, Y. Cao, H.-Y. He and K.-N. Fan, *J. Catal.*, 2009, **263**, 104-113.

70. Y. Liu, C. Wen, Y. Guo, G. Lu and Y. Wang, *J. Mol. Catal. A: Chem.*, 2010, **316**, 59-64.

71. Y.-Z. Wang, Y.-X. Zhao, C.-G. Gao and D.-S. Liu, *Catal. Lett.*, 2007, **116**, 136-142.

72. M. J. Pollard, B. A. Weinstock, T. E. Bitterwolf, P. R. Griffiths, A. Piers Newbery and J. B. Paine III, *J. Catal.*, 2008, **254**, 218-225.

73. F. Grillo, M. M. Natile and A. Glisenti, *Appl. Catal., B*, 2004, **48**, 267-274.

74. J. Jansson, *J. Catal.*, 2000, **194**, 55-60.

75. J. Jansson, M. Skoglundh, E. Fridell and P. Thormählen, *Top. Catal.*, 2001, **16**, 385-389.

76. J. Jansson, A. E. Palmqvist, E. Fridell, M. Skoglundh, L. Österlund, P. Thormählen and V. Langer, *J. Catal.*, 2002, **211**, 387-397.

77. S. Tang, J. Lin and K. Tan, *Catal. Lett.*, 1998, **51**, 169-175.

78. J. Lee, M. C. Orilall, S. C. Warren, M. Kamperman, F. J. DiSalvo and U. Wiesner, *Nature Mater.*, 2008, **7**, 222-228.

79. M. Özacar, A. S. Poyraz, H. C. Genuino, C.-H. Kuo, Y. Meng and S. L. Suib, *Appl. Catal., A*, 2013, **462**, 64-74.

80. H.-K. Lin, H.-C. Chiu, H.-C. Tsai, S.-H. Chien and C.-B. Wang, *Catal. Lett.*, 2003, **88**, 169-174.

81. H. Tüysüz, M. Comotti and F. Schüth, *Chem. Commun.*, 2008, 4022-4024.

82. L. Hu, K. Sun, Q. Peng, B. Xu and Y. Li, *Nano Research*, 2010, **3**, 363-368.

83. P. Li, C. He, J. Cheng, C. Y. Ma, B. J. Dou and Z. P. Hao, *Appl. Catal., B*, 2011, **101**, 570-579.

84. J. Luo, Q. Zhang, J. Garcia-Martinez and S. L. Suib, *J. Am. Chem. Soc.*, 2008, **130**, 3198-3207.

85. V. D. Makwana, Y.-C. Son, A. R. Howell and S. L. Suib, *J. Catal.*, 2002, **210**, 46-52.

86. C. Homer, D. Saminda, C. Eric, C. Michael and L. Steven, *J. Phys. Chem. C*, 2012, **116**, 12066-12078.

87. V. Shapovalov and H. Metiu, *J. Catal.*, 2007, **245**, 205-214.

88. H. Y. Kim, H. M. Lee and G. Henkelman, *J. Am. Chem. Soc.*, 2012, **134**, 1560-1570.

89. N. A. Merino, B. P. Barbero, P. Grange and L. E. Cadús, *J. Catal.*, 2005, **231**, 232-244.

90. J. Li, G. Lu, G. Wu, D. Mao, Y. Wang and Y. Guo, *Catal. Sci. Technol.*, 2012, **2**, 1865-1871.

91. G. Xia, Y. Yin, W. Willis, J. Wang and S. Suib, *J. Catal.*, 1999, **185**, 91-105.

92. T. Zhou, L. Li, J. Cheng and Z. Hao, *Ceram. Int.*, 2010, **36**, 529-534.

93. J. N. Armor, *Chem. Mater.*, 1994, **6**, 730-738.

94. A. S. Poyraz, W. Song, D. Kriz, C.-H. Kuo, M. S. Seraji and S. L. Suib, *ACS Appl. Mater. Interfaces*, 2014, **6**, 10986-10991.

95. S. Biswas, A. S. Poyraz, Y. Meng, C.-H. Kuo, C. Guild, H. Tripp and S. L. Suib, *Appl. Catal., B*, 2015, **165**, 731-741.

96. H. C. Genuino, S. Dharmarathna, E. C. Njagi, M. C. Mei and S. L. Suib, *J. Phys. Chem. C*, 2012, **116**, 12066-12078.

97. M. Hajjari, M. Ardjmand and M. Tabatabaei, *RSC Adv.*, 2014, **4**, 14352-14356.

98. C.-J. Jia, M. Schwickardi, C. Weidenthaler, W. Schmidt, S. Korhonen, B. M. Weckhuysen and F. Schüth, *J. Am. Chem. Soc.*, 2011, **133**, 11279-11288.

99. Y. Tanaka, T. Utaka, R. Kikuchi, K. Sasaki and K. Eguchi, *Appl. Catal., A*, 2003, **242**, 287-295.

100. S. Hosseini, A. Niaei, D. Salari, M. Alvarez-Galvan and J. Fierro, *Ceram. Int.*, 2014, **40**, 6157-6163.

101. T. W. Kim, M. A. Woo, M. Regis and K.-S. Choi, *J. Phys. Chem. Lett.*, 2014, **5**, 2370-2374.

102. Y. Liang, H. Wang, J. Zhou, Y. Li, J. Wang, T. Regier and H. Dai, *J. Am. Chem. Soc.*, 2012, **134**, 3517-3523.

103. Y. Zhang, F. Ding, C. Deng, S. Zhen, X. Li, Y. Xue, Y.-M. Yan and K. Sun, *Catal. Commun.*, 2015, **67**, 78-82.

104. H.-Y. Wang, S.-F. Hung, H.-Y. Chen, T.-S. Chan, H. M. Chen and B. Liu, *J. Am. Chem. Soc.*, 2015.

105. J. Xiao, Q. Kuang, S. Yang, F. Xiao, S. Wang and L. Guo, *Sci. Rep.*, 2013, **3**.

106. X. Ge, Y. Liu, F. T. Goh, T. A. Hor, Y. Zong, P. Xiao, Z. Zhang, S. H. Lim, B. Li and X. Wang, *ACS Appl. Mater. Interfaces*, 2014, **6**, 12684-12691.

107. T. N. Lambert, J. A. Vigil, S. E. White, D. J. Davis, S. J. Limmer, P. D. Burton, E. N. Coker, T. E. Beechem and M. T. Brumbach, *Chem. Commun.*, 2015, **51**, 9511-9514.

108. X. Liu, Z. Chang, L. Luo, T. Xu, X. Lei, J. Liu and X. Sun, *Chem. Mater.*, 2014, **26**, 1889-1895.

109. P. W. Menezes, A. Indra, D. González-Flores, N. R. Sahraie, I. Zaharieva, M. Schwarze, P. Strasser, H. Dau and M. Driess, *ACS Catal.*, 2015, **5**, 2017-2027.

110. Y. J. Sa, K. Kwon, J. Y. Cheon, F. Kleitz and S. H. Joo, *J. Mater. Chem. A*, 2013, **1**, 9992-10001.

111. C. Jin, F. Lu, X. Cao, Z. Yang and R. Yang, *J. Mater. Chem. A*, 2013, **1**, 12170-12177.

112. W. Song, A. S. Poyraz, Y. Meng, Z. Ren, S.-Y. Chen and S. L. Suib, *Chem. Mater.*, 2014, **26**, 4629-4639.

113. Y. Liang, H. Wang, P. Diao, W. Chang, G. Hong, Y. Li, M. Gong, L. Xie, J. Zhou and J. Wang, *J. Am. Chem. Soc.*, 2012, **134**, 15849-15857.

114. Y. Li, P. Hasin and Y. Wu, *Adv. Mater.*, 2010, **22**, 1926-1929.

115. E. Rios, J.-L. Gautier, G. Poillerat and P. Chartier, *Electrochim. Acta*, 1998, **44**, 1491-1497.

116. Z.-Q. Liu, Q.-Z. Xu, J.-Y. Wang, N. Li, S.-H. Guo, Y.-Z. Su, H.-J. Wang, J.-H. Zhang and S. Chen, *Int. J. Hydrogen Energy*, 2013, **38**, 6657-6662.

117. F. Maillard, A. Bonnefont, M. Chatenet, L. Guétaz, B. Doisneau-Cottignies, H. Roussel and U. Stimming, *Electrochim. Acta*, 2007, **53**, 811-822.

118. M. De Koninck and B. Marsan, *Electrochim. Acta*, 2008, **53**, 7012-7021.

119. F. Cheng, J. Shen, B. Peng, Y. Pan, Z. Tao and J. Chen, *Nature Chem.*, 2011, **3**, 79-84.

120. A. Queiroz and F. Lima, *J. Electroanal. Chem.*, 2013, **707**, 142-150.

121. D. Wang, X. Chen, D. G. Evans and W. Yang, *Nanoscale*, 2013, **5**, 5312-5315.

122. C.-H. Kuo, I. M. Mosa, S. Thanneeru, V. Sharma, L. Zhang, S. Biswas, M. Aindow, S. P. Alpay, J. F. Rusling and S. L. Suib, *Chem. Commun.*, 2015, **51**, 5951-5954.

123. M.-R. Gao, Y.-F. Xu, J. Jiang, Y.-R. Zheng and S.-H. Yu, *J. Am. Chem. Soc.*, 2012, **134**, 2930-2933.

124. C. Xiao, X. Lu and C. Zhao, *Chem. Commun.*, 2014, **50**, 10122-10125.

125. X. Deng, W. N. Schmidt and H. Tüysüz, *Chem. Mater.*, 2014, **26**, 6127-6134.

126. C. C. McCrory, S. Jung, J. C. Peters and T. F. Jaramillo, *J. Am. Chem. Soc.*, 2013, **135**, 16977-16987.

127. J. A. Koza, Z. He, A. S. Miller and J. A. Switzer, *Chem. Mater.*, 2012, **24**, 3567-3573.

128. B. S. Yeo and A. T. Bell, *J. Am. Chem. Soc.*, 2011, **133**, 5587-5593.

129. Y. Lai, Y. Li, L. Jiang, W. Xu, X. Lv, J. Li and Y. Liu, *J. Electroanal. Chem.*, 2012, **671**, 16-23.

130. V. Hadjiev, M. Iliev and I. Vergilov, *J. Phys. C: Solid State Phys.*, 1988, **21**, L199.

131. L. Huang, D. Chen, Y. Ding, S. Feng, Z. L. Wang and M. Liu, *Nano Lett.*, 2013, **13**, 3135-3139.

132. M. Bouchard and A. Gambardella, *J. Raman Spectrosc.*, 2010, **41**, 1477-1485.

133. Z. M. Stanojević, N. Romčević and B. Stojanović, *J. Eur. Ceram. Soc.*, 2007, **27**, 903-907.

134. C. F. Windisch, G. J. Exarhos and R. R. Owings, *Vibrational spectroscopic study of the site occupancy distribution of cations in nickel cobalt oxides*, Pacific Northwest National Laboratory (PNNL), Richland, WA (US), 2004.

135. Y. Lou, X.-M. Cao, J. Lan, L. Wang, Q. Dai, Y. Guo, J. Ma, Z. Zhao, Y. Guo and P. Hu, *Chem. Commun.*, 2014, **50**, 6835-6838.

136. R. Bhargava, P. K. Sharma, S. Kumar, A. C. Pandey and N. Kumar, *J. Raman Spectrosc.*, 2011, **42**, 1802-1807.

137. F. Cheng, T. Zhang, Y. Zhang, J. Du, X. Han and J. Chen, *Angew. Chem. Int. Ed.*, 2013, **52**, 2474-2477.

138. T. Y. Ma, Y. Zheng, S. Dai, M. Jaroniec and S. Z. Qiao, *J. Mater. Chem. A*, 2014, **2**, 8676-8682.

139. J. Kibsgaard, Y. Gorlin, Z. Chen and T. F. Jaramillo, *J. Am. Chem. Soc.*, 2012, **134**, 7758-7765.

APPENDIX

List of Publications, Patent Applications, Presentations, and Posters

Journal Articles

- **Song, W.**; Ren, Z.; Chen, S.-Y.; Meng, Y.; Biswas, S.; Nandi, P.; Elsen, H. A.; Gao, P.-X.; Suib, S. L., Ni and Mn-Substituted Mesoporous Co_3O_4: an Ultra Stable Bifunctional Catalyst with Surface Structure Dependent Activity for Oxygen Reduction Reaction and Oxygen Evolution Reaction. Submitted to *ACS Applied Materials & Interfaces* **2016**, 8, 20802-20813.

- Jafari, T.; Moharreri, E.; Amin, A. S.; Miao, R.; **Song, W.**; Suib, S. L., Photocatalytic Water Splitting—The Untamed Dream: A Review of Recent Advances. *Molecules* **2016**, 21, 900.

- Liu, B.; Yao, H.; **Song, W.**; Jin, L.; Mosa, I. M.; Rusling, J. F.; Suib, S. L.; He, J., Ligand-Free Noble Metal Nanocluster Catalysts on Carbon Supports via "Soft" Nitriding. *Journal of the American Chemical Society* **2016**,138, 4718-4721.

- Chen, S.-Y.; **Song, W.**; Lin, H.-J.; Wang, S.; Biswas, S.; Mollahosseini, M.; Kuo, C.-H.; Gao, P.-X.; Suib, S. L., Manganese Oxide Nanoarray-Based Monolithic Catalysts: Tunable Morphology and High Efficiency for CO Oxidation. *ACS Applied Materials & Interfaces* **2016**, 8, 7834-7842.

- Ren, Z.; Wu, Z.; **Song, W.**; Xiao, W.; Guo, Y.; Ding, J.; Suib, S. L.; Gao, P.-X., Low Temperature Propane Oxidation over Co_3O_4 Based Nano-array Catalysts: Ni Dopant Effect, Reaction Mechanism and Structural Stability. *Applied Catalysis B: Environmental* **2016**, 180, 150-160.

- Liu, B.; Mosa, I. M.; **Song, W.**; Zheng, H.; Kuo, C.-H.; Rusling, J. F.; Suib, S. L.; He, J., Unconventional Structural and Morphological Transitions of Nanosheets, Nanoflakes and Nanorods of AuNP@MnO_2. *Journal of Materials Chemistry A* **2016**, 4, 6447-6455.

- Liu, B.; Yao, H.; Daniels, R. A.; **Song, W.**; Zheng, H.; Jin, L.; Suib, S. L.; He, J., A Facile Synthesis of Fe_3C@ Mesoporous Carbon Nitride Nanospheres with Superior Electrocatalytic Activity. *Nanoscale* **2016**, 8, 5441-5445.

- Mosa, I. M.; Biswas, S.; El-Sawy, A. M.; Botu, V.; Guild, C.; **Song, W.**; Ramprasad, R.; Rusling, J. F.; Suib, S. L., Tunable Mesoporous Manganese Oxide for High Performance Oxygen Reduction and Evolution Reactions. *Journal of Materials Chemistry A* **2016**, 4, 620-631.

- Wang, S.; Ren, Z.; **Song, W.**; Guo, Y.; Zhang, M.; Suib, S. L.; Gao, P.-X., ZnO/Perovskite Core–shell Nanorod Array Based Monolithic Catalysts with Enhanced Propane Oxidation and Material Utilization Efficiency at Low Temperature. *Catalysis Today* **2015**, 258, 549-555.

- Liu, B.; Luo, Z.; Federico, A.; **Song, W.**; Suib, S. L.; He, J., Colloidal Amphiphile-Templated Growth of Highly Crystalline Mesoporous Nonsiliceous Oxides. *Chemistry of Materials* **2015**, 27, 6173-6176.

- Jiang, T.; Du, S.; Jafari, T.; Zhong, W.; Sun, Y.; **Song, W.**; Luo, Z.; Hines, W. A.; Suib, S. L., Synthesis of Mesoporous γ-Fe_2O_3 Supported Palladium Nanoparticles and Investigation of Their Roles as Magnetically Recyclable Catalysts for Nitrobenzene Hydrogenation. *Applied Catalysis A: General* **2015**, 502, 105-113.

- Liu, B.; Kuo, C.-H.; Chen, J.; Luo, Z.; Thanneeru, S.; Li, W.; **Song, W.**; Biswas, S.; Suib, S. L.; He, J., Ligand-Assisted Co-Assembly Approach toward Mesoporous Hybrid Catalysts of

Transition-Metal Oxides and Noble Metals: Photochemical Water Splitting. *Angewandte Chemie International Edition*, **2015**, 127, 9189-9193.

- Kuo, C.-H.; Mosa, I. M.; Poyraz, A. S.; Biswas, S.; El-sawy, A. M.; **Song, W.**; Luo, Z.; Chen, S.-Y.; Rusling, J. F.; He, J.; Suib, S. L., Robust Mesoporous Manganese Oxide Catalysts for Water Oxidation. *ACS Catalysis* **2015**, 5, 1693-1699.

- Pahalagedara, L. R.; Poyraz, A.; **Song, W.**; Kuo, C.-H.; Pahalagedara, M. N.; Meng, Y.; Suib, S. L., Low Temperature Desulfurization of H_2S: High Sorption Capacities by Mesoporous Cobalt Oxide via Increased H_2S Diffusion. *Chemistry of Materials* **2014**, 26, 6613-6621.

- Meng, Y.; **Song, W.**; Huang, H.; Ren, Z.; Chen, S.-Y.; Suib, S. L., Structure–Property Relationship of Bifunctional MnO_2 Nanostructures: Highly Efficient, Ultra-Stable Electrochemical Water Oxidation and Oxygen Reduction Reaction Catalysts Identified in Alkaline Media. *Journal of the American Chemical Society* **2014**, 136, 11452-11464. (Highly cited paper, top 1% paper by Thomson Reuters)

- **Song, W.**; Poyraz, A. S.; Meng, Y.; Ren, Z.; Chen, S.; Suib, S. L., Mesoporous Co_3O_4 with Controlled Porosity: Inverse Micelle Synthesis and High-Performance Catalytic CO Oxidation at −60°C. *Chemistry of Materials* **2014**, 26, 4629−4639.

- Ren, Z.; Botu, V.; Wang, S.; Meng, Y.; **Song, W.**; Guo, Y.; Ramprasad, R.; Suib, S. L.; Gao, P.-X., Monolithically Integrated Spinel $M_xCo_{3-x}O_4$ (M=Co, Ni, Zn) Nanoarray Catalysts: Scalable Synthesis and Cation Manipulation for Tunable Low-Temperature CH4 and CO Oxidation. *Angewandte Chemie International Edition* **2014**, 53, 7223−7227.

- Kuo, C.-H.; Li, W.; **Song, W.**; Luo, Z.; Poyraz, A. S.; Guo, Y.; Ma, A. W.; Suib, S. L.; He, J., Facile Synthesis of Co_3O_4@CNT with High Catalytic Activity for CO Oxidation under Moisture-Rich Conditions. *ACS Applied Materials & Interfaces* **2014**, 6, 11311−11317.

- Poyraz, A. S.; **Song, W.**; Kriz, D.; Kuo, C.; Seraji, M. S.; Suib, S. L., Crystalline Mesoporous $K_{2-X}Mn_8O_{16}$ and ε-MnO_2 by Mild Transformations of Amorphous Mesoporous Manganese Oxides and Their Enhanced Redox Properties. *ACS Applied Materials & Interfaces* **2014**, 6, 10986−10991.

- Meng, Y.; Chen, D.; **Song, W.**; Xin, G., Chemical Synthesis and Application of Graphitic Carbon Nitrides. *Guangzhou Chemical Industry* **2010**, 8, 33.

Patent

- He, J.; **Song, W.**; Meng, Y.; Suib, S. L. Manganese Oxides/Graphene Nanocomposites, Films, And Membranes and Methods of Making. U.S. Provisional Application No.:62/031,846.

Conference Presentations

- **Song, W.**; Poyraz, A. S.; Meng, Y.; Ren, Z.; Chen, S.; Suib, S. L., Mesoporous Co_3O_4 Catalyst for CO Oxidation at -60ºC: Controlled Porosity, Reaction Mechanism and Deactivation Reason. *249th ACS National Meeting & Exposition* **2015**, Denver, CO.

- **Song, W.**; Ren, Z.; Chen, S.-Y.; Suib, S. L., Controlled Synthesis of Ni and Mn-Substituted Mesoporous Co_3O_4 and Its Surface Structure Dependent Activity for Oxygen Reduction Reaction and Oxygen Evolution Reaction. *2015 MRS Fall Meeting & Exhibit* **2015**, Boston, MA.